

Study of $\Lambda(1520)$ Resonances & D Mesons at the LHC Energies and Phase Transition in Magnetized Compact Stars

By

Rama Chandra Baral

PHYS07200904001

Institute of Physics, Bhubaneswar

A thesis submitted to the

Board of Studies in Physical Sciences

In partial fulfillment of requirements

For the Degree of

DOCTOR OF PHILOSOPHY

of

HOMI BHABHA NATIONAL INSTITUTE

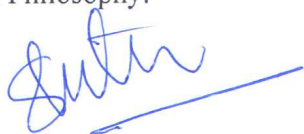


January, 2017

Homi Bhabha National Institute

Recommendations of the Viva Voce Board

As members of the Viva Voce Board, we certify that we have read the dissertation prepared by **Mr. RAMA CHANDRA BARAL** entitled “**Study of $\Lambda(1520)$ Resonances & D Mesons at the LHC Energies and Phase Transition in Magnetized Compact Stars**”, and recommend that it may be accepted as fulfilling the dissertation requirement for the Degree of Doctor of Philosophy.



Date: 16/01/2017

Chairman – Prof. S. K. Patra



Date: 16/01/2017

Guide / Convener – Prof. P. K. Sahu



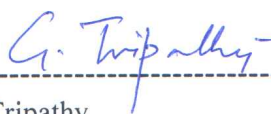
Date: 16/1/17

Member 1 – Prof. S. Ghosh, BOSE Institute, Kolkata (External)



Date: 16/1/2017

Member 2 – Prof. B. Mohanty (NISER, Bhubaneswar)



Date: 16/1/17

Member 3 – Prof. G. Tripathy

Final approval and acceptance of this dissertation is contingent upon the candidate's submission of the final copies of the dissertation to HBNI.

I hereby certify that I have read this dissertation prepared under my direction and recommend that it may be accepted as fulfilling the dissertation requirement.

Date: 16/01/2017
Place: Bhubaneswar



(Prof. P.K. Sahu)

STATEMENT BY AUTHOR

This dissertation has been submitted in partial fulfilment of requirements for an advanced degree at Homi Bhabha National Institute (HBNI) and is deposited in the Library to be made available to borrowers under rules of the HBNI. Brief quotations from this dissertation are allowable without special permission, provided that accurate acknowledgement of source is made. Requests for permission for extended quotation from or reproduction of this manuscript in whole or in part may be granted by the Competent Authority of HBNI when in his or her judgment the proposed use of the material is in the interests of scholarship. In all other instances, however, permission must be obtained from the author.

Rama Chandra Baral

Mr. Rama Chandra Baral

Date: *17 January 2017*

CERTIFICATE

This is to certify that the thesis entitled "**Study of $\Lambda(1520)$ Resonances & D Mesons at the LHC Energies and Phase Transition in Magnetized Compact Stars**", which is being submitted by **Mr. Rama Chandra Baral**, in partial fulfillment of the degree of **Doctor of Philosophy in Physics** of **Homi Bhabha National Institute** is a record of his own research work carried by him. He has carried out his investigations for the last six years on the subject matter of the thesis under my supervision at the **Institute of Physics, Bhubaneswar**. To the best of our knowledge, the matter embodied in this thesis has not been submitted for the award of any other degree.

Ramachandra Baral

Mr. Rama Chandra Baral

Institute of Physics, Bhubaneswar

Pradip Kumar Sahu

Prof. Pradip Kumar Sahu

Institute of Physics, Bhubaneswar

DECLARATION

I, Mr. Rama Chandra Baral, hereby declare that the investigations presented in the thesis have been carried out by me. The matter embodied in the thesis is original and has not been submitted earlier as a whole or in part for a degree/diploma at this or any other Institution/University.

Ramachandra Baral

Rama Chandra Baral

Institute of Physics, Bhubaneswar

Dedicated

to

my grand mother and ganga ...

List of Publications arising from the thesis

Published

1. Radial oscillation of compact stars in the presence of magnetic field
R. C. Baral, K. K. Mohanta, N. R. Panda and P. K. Sahu
Int. J. Mod. Phys. E 25, 6 (2016) 1650037
2. Production of D-mesons in p+p and p+Pb collisions at LHC energies
R. C. Baral, S. K. Tripathy, M. Younus, Z. Naik, P. K. Sahu
Int. J. Mod. Phys. E 25, 11 (2016) 1650092

List of Publication as a part of ALICE Collaboration

1. Centrality dependence of charged jet production in p-Pb collisions at $\sqrt{s_{NN}} = 5.02$ TeV, *Eur. Phys. J. C* 76 (2016) no.5, 271
2. Particle identification in ALICE: a Bayesian approach, *Eur. Phys. J. Plus* 131 (2016) no.5, 168
3. Anisotropic flow of charged particles in Pb-Pb collisions at $\sqrt{s_{NN}} = 5.02$ TeV, *Phys. Rev. Lett.* 116 (2016) 13230
4. Event shape engineering for inclusive spectra and elliptic flow in Pb-Pb collisions at $\sqrt{s_{NN}} = 2.76$ TeV, *Phys. Rev. C* 93 (2016) 034916
5. Centrality dependence of the nuclear modification factor of charged pions, kaons, and protons in Pb-Pb collisions at $\sqrt{s_{NN}} = 2.76$ TeV, *Phys. Rev. C* 93 (2016) 034913

6. Transverse momentum dependence of D-meson production in Pb-Pb collisions at $\sqrt{s_{NN}} = 2.76$ TeV, JHEP 03 (2016) 081
7. Measurement of D_s^+ production and nuclear modification factor in Pb-Pb collisions at $\sqrt{s_{NN}} = 2.76$ TeV, JHEP 03 (2016) 082
8. Multiplicity and transverse momentum evolution of charge-dependent correlations in pp, p-Pb, and Pb-Pb collisions at the LHC, Eur. Phys. J. C 76 (2016) 86
9. Centrality dependence of pion freeze-out radii in Pb-Pb collisions at $\sqrt{s_{NN}} = 2.76$ TeV, Phys. Rev. C 93 (2016) 024905
10. Direct photon production in Pb-Pb collisions at $\sqrt{s_{NN}} = 2.76$ TeV, Phys. Lett. B 754 (2016) 235-248
11. Forward-central two-particle correlations in p-Pb collisions at $\sqrt{s_{NN}} = 5.02$ TeV, Phys. Lett. B 753 (2016) 126-139
12. Centrality evolution of the charged-particle pseudorapidity density over a broad pseudorapidity range in Pb-Pb collisions at $\sqrt{s_{NN}} = 2.76$ TeV, Phys. Lett. B 754 (2016) 373-385
13. ${}^3_{\Lambda}\text{H}$ and ${}^3_{\Lambda}\bar{\text{H}}$ production in Pb-Pb collisions at $\sqrt{s_{NN}} = 2.76$ TeV, Phys. Lett. B 754 (2016) 360-372
14. Study of cosmic ray events with high muon multiplicity using the ALICE detector at the CERN Large Hadron Collider, JCAP 01 (2016) 032
15. Measurement of electrons from heavy-flavour hadron decays in p-Pb collisions at $\sqrt{s_{NN}} = 5.02$ TeV, Phys. Lett. B 754 (2016) 81-93

16. Azimuthal anisotropy of charged jet production in $\sqrt{s_{NN}} = 2.76$ TeV collisions, Phys. Lett. B 753 (2016) 511-525
17. Pseudorapidity and transverse-momentum distributions of charged particles in proton-proton collisions at $\sqrt{s} = 13$ TeV, Phys. Lett. B 753 (2016) 319-329
18. Elliptic flow of muons from heavy-flavour hadron decays at forward rapidity in Pb-Pb collisions at $\sqrt{s_{NN}} = 2.76$ TeV, Phys. Lett. B 753 (2016) 41-56
19. Search for weakly decaying $\bar{\Lambda}n$ and $\Lambda\Lambda$ exotic bound states in central Pb-Pb collisions at $\sqrt{s_{NN}} = 2.76$ TeV, Phys. Lett. B 752 (2016) 267-277
20. Production of light nuclei and anti-nuclei in pp and Pb-Pb collisions at LHC energies, Phys. Rev. C 93 (2015) 024917
21. Centrality dependence of high- p_T D meson suppression in Pb-Pb collisions at $\sqrt{s_{NN}} = 2.76$ TeV, JHEP 11 (2015) 205
22. One-dimensional pion, kaon, and proton femtoscopy in Pb-Pb collisions at $\sqrt{s_{NN}} = 2.76$ TeV, Phys. Rev. C 92 (2015) 054908
23. Centrality dependence of inclusive J/ψ production in p-Pb collisions at $\sqrt{s_{NN}} = 5.02$ TeV, JHEP 11 (2015) 127
24. Coherent $\psi(2S)$ photo-production in ultra-peripheral Pb-Pb collisions at $\sqrt{s_{NN}} = 2.76$ TeV, Phys. Lett. B 751 (2015) 358-370
25. Measurement of jet quenching with semi-inclusive hadron-jet distributions in central Pb-Pb collisions at $\sqrt{s_{NN}} = 2.76$ TeV, JHEP 09 (2015) 170

26. Measurement of charm and beauty production at central rapidity versus charged-particle multiplicity in proton-proton collisions at $\sqrt{s} = 7$ TeV, JHEP 09 (2015) 148
27. Coherent ρ^0 photo-production in ultra-peripheral Pb-Pb collisions at $\sqrt{s_{NN}} = 2.76$ TeV, JHEP 09 (2015) 095
28. Precision measurement of the mass difference between light nuclei and anti-nuclei, Nature Physics 11 (2015) 811-814
29. Measurement of charged jet production cross sections and nuclear modification in p-Pb collisions at $\sqrt{s_{NN}} = 2.76$ TeV, Phys. Lett. B 749 (2015) 68-81
30. Inclusive, prompt and non-prompt J/ψ production at mid-rapidity in Pb-Pb collisions at $\sqrt{s_{NN}} = 2.76$ TeV, JHEP 07 (2015) 051
31. Elliptic flow of identified hadrons in Pb-Pb collisions at $\sqrt{s_{NN}} = 2.76$ TeV, JHEP 06 (2015) 190
32. Charged jet cross sections and properties in proton-proton collisions at $\sqrt{s} = 7$ TeV, Phys. Rev. D 91 (2015) 112012
33. Production of inclusive $\Upsilon(1S)$ and $\Upsilon(2S)$ in p-Pb collisions at $\sqrt{s_{NN}} = 5.02$ TeV, Phys. Lett. B 740 (2015) 105-117
34. Rapidity and transverse-momentum dependence of the inclusive J/ψ nuclear modification factor in p-Pb collisions at $\sqrt{s_{NN}} = 5.02$ TeV, JHEP 06 (2015) 55
35. Centrality dependence of particle production in p-Pb collisions at $\sqrt{s_{NN}} = 5.02$ TeV, Phys. Rev. C 91 (2015) 064905

36. Measurement of pion, kaon and proton production in proton-proton collisions at $\sqrt{s} = 7$ TeV, EPJC 75 (2015) 226
37. Forward-backward multiplicity correlations in pp collisions at $\sqrt{s} = 0.9, 2.76$ and 7 TeV, JHEP 05 (2015) 097
38. Measurement of dijet k_T in p-Pb collisions at $\sqrt{s_{NN}} = 5.02$ TeV, Phys. Lett. B 746 (2015) 385
39. Measurement of jet suppression in central Pb-Pb collisions at $\sqrt{s_{NN}} = 2.76$ TeV, Phys. Lett. B 746 (2015) 1
40. Inclusive photon production at forward rapidities in proton-proton collisions at $\sqrt{s} = 0.9, 2.76$ and 7 TeV, EPJC 75 (2015) 146
41. Two-pion femtoscopy in p-Pb collisions at $\sqrt{s_{NN}} = 5.02$ TeV, Phys. Rev. C 91 (2015) 034906
42. $K^*(892)^0$ and $\phi(1020)$ production in Pb-Pb collisions at $\sqrt{s_{NN}} = 2.76$ TeV, Phys. Rev. C 91 (2015) 024609
43. Production of $\Sigma(1385)^\pm$ and $\Xi(1530)^0$ in proton-proton collisions at $\sqrt{s} = 7$ TeV, Eur. Phys. J. C 75 (2015) 1
44. Measurement of electrons from semileptonic heavy-flavor hadron decays in pp collisions at $\sqrt{s} = 2.76$ TeV, Phys. Rev. D 91 (2015) 012001
45. Multiplicity dependence of jet-like two-particle correlations in p-Pb collisions at $\sqrt{s_{NN}} = 5.02$ TeV, Phys. Lett. B 741 (2015) 38-50
46. Suppression of $\psi(2S)$ production in p-Pb collisions at $\sqrt{s_{NN}} = 5.02$ TeV, JHEP 12 (2014) 073

47. Measurement of prompt D-meson production in p-Pb collisions at $\sqrt{s_{NN}} = 5.02$ TeV, Phys. Rev. Lett. 113 (2014) 232301
48. Exclusive J/ψ photoproduction off protons in ultra-peripheral p-Pb collisions at $\sqrt{s_{NN}} = 5.02$ TeV, Phys. Rev. Lett. 113 (2014) 232504
49. Measurement of visible cross sections in proton-lead collisions at $\sqrt{s_{NN}} = 5.02$ TeV in van der Meer scans with the ALICE detector, JINST 9 (2014) 1100
50. Multi-particle azimuthal correlations in p-Pb and Pb-Pb collisions at the CERN Large Hadron Collider, Phys. Rev. C 90 (2014) 054901
51. Event-by-event mean p_T fluctuations in pp and Pb-Pb collisions at the LHC, Eur. Phys. J. C (2014) 74-3077
52. Freeze-out radii extracted from three-pion cumulants in pp, p-Pb and Pb-Pb collisions at the LHC, Phys. Lett. B 739 (2014) 139-151
53. Neutral pion production at midrapidity in pp and Pb-Pb collisions at $\sqrt{s_{NN}} = 2.76$ TeV, Eur. Phys. J. C 74 (2014) 3108
54. Suppression of $\Upsilon(1S)$ at forward rapidity in Pb-Pb collisions at $\sqrt{s_{NN}} = 2.76$ TeV, Phys. Lett. B 738 (2014) 361-372
55. Performance of the ALICE Experiment at the CERN LHC, Int. J. Mod. Phys. A 29 (2014) 1430044
56. Beauty production in pp collisions at $\sqrt{s} = 2.76$ TeV measured via semi-electronic decays, Phys. Lett. B 738 (2014) 97
57. Transverse momentum dependence of inclusive primary charged-particle production in p-Pb collisions at $\sqrt{s_{NN}} = 5.02$ TeV, Eur. Phys. J. C 74 (2014) 3054

58. Azimuthal anisotropy of D meson production in Pb-Pb collisions at $\sqrt{s_{NN}} = 2.76$ TeV, Phys. Rev. C 90 (2014) 034904
59. Measurement of quarkonium production at forward rapidity in pp collisions at $\sqrt{s} = 7$ TeV, Eur. Phys. J. C 74 (2014) 2974
60. Production of charged pions, kaons and protons at large transverse momenta in pp and Pb-Pb collisions at $\sqrt{s_{NN}} = 2.76$ TeV, PLB 736 (2014) 196-207
61. Multiplicity Dependence of Pion, Kaon, Proton and Lambda Production in p-Pb Collisions at $\sqrt{s_{NN}} = 5.02$ TeV, Phys. Lett. B 728 (2014) 25-38
62. Centrality, rapidity and transverse momentum dependence of J/ψ suppression in Pb-Pb collisions at $\sqrt{s_{NN}} = 2.76$ TeV, Phys. Lett. B 734 (2014) 314-327
63. Measurement of charged jet suppression in Pb-Pb collisions at $\sqrt{s_{NN}} = 2.76$ TeV, JHEP 03 (2014) 013
64. J/ψ production and nuclear effects in p-Pb collisions at $\sqrt{s_{NN}} = 5.02$ TeV, JHEP 02 (2014) 073
65. Two and Three-Pion Quantum Statistics Correlations in Pb-Pb Collisions at $\sqrt{s_{NN}} = 2.76$ TeV at the LHC, Phys. Rev. C 89 (2014) 024911
66. Multi-strange baryon production at mid-rapidity in Pb-Pb collisions at $\sqrt{s_{NN}} = 2.76$ TeV, Phys. Lett. B 728 (2014) 216-227
67. Upgrade of the ALICE Inner Tracking System - Technical Design Report, J. Phys. G. 41 (2014) 087002

68. Directed flow of charged particles at mid-rapidity relative to the spectator plane in Pb-Pb collisions at $\sqrt{s_{NN}} = 2.76$ TeV, Phys. Rev. Lett. 111 (2013) 232302
69. Energy Dependence of the Transverse Momentum Distributions of Charged Particles in pp Collisions Measured by ALICE, Eur. Phys. J. C 73 (2013) 2662
70. K_s^0 and Λ production in Pb-Pb collisions at $\sqrt{s_{NN}} = 2.76$ TeV, Phys. Rev. Lett. 111 (2013) 222301
71. Charmonium and e^+e^- pair photoproduction at mid-rapidity in ultra-peripheral Pb-Pb collisions at $\sqrt{s_{NN}} = 2.76$ TeV, Eur. Phys. J. C 73 (2013) 2617
72. Multiplicity dependence of the average transverse momentum in pp, p-Pb, and Pb-Pb collisions at the LHC, Phys. Lett. B 727 (2013) 371-380
73. J/ψ Elliptic Flow in Pb-Pb Collisions at $\sqrt{s_{NN}} = 2.76$ TeV, Phys. Rev. Lett. 111 (2013) 162301
74. Centrality determination of Pb-Pb collisions at $\sqrt{s_{NN}} = 2.76$ TeV with ALICE, Phys. Rev. C 88 (2013) 044909
75. Centrality dependence of π , K , p production in Pb-Pb collisions at $\sqrt{s_{NN}} = 2.76$ TeV, Phys. Rev. C 88 (2013) 044910
76. Performance of the ALICE VZERO system, JINST 8 (2013) P10016
77. Centrality dependence of the pseudorapidity density distribution for charged particles in Pb-Pb collisions at $\sqrt{s_{NN}} = 2.76$ TeV, Phys. Lett. B 726 (2013) 610-622

78. Multiplicity dependence of two-particle azimuthal correlations in pp collisions at the LHC, JHEP 09 (2013) 049
79. D meson elliptic flow in non-central Pb-Pb collisions at $\sqrt{s_{NN}} = 2.76$ TeV, Phys. Rev. Lett. 111 (2013) 102301
80. Long-range angular correlations of π , K and p in p-Pb collisions at $\sqrt{s_{NN}} = 5.02$ TeV, Phys. Lett. B 726 (2013) 164-177
81. Mid-rapidity anti-baryon to baryon ratios in pp collisions at $\sqrt{s} = 0.9, 2.76$ and 7 TeV measured by ALICE, Eur. Phys. J. C 73 (2013) 2496
82. Measurement of inelastic, single and double diffraction cross sections in proton-proton collisions at LHC with ALICE, Eur. Phys. J. C (2013) 73:2456
83. Charge correlations using the balance function in Pb-Pb collisions at $\sqrt{s_{NN}} = 2.76$ TeV Phys. Lett. B 723 (2013) 267-279
84. Measurement of the inclusive differential jet cross-section in pp collisions at $\sqrt{s} = 2.76$ TeV, Phys. Lett. B 722 (2013) 262-272
85. Net-Charge Fluctuations in Pb-Pb collisions at $\sqrt{s_{NN}} = 2.76$ TeV, Phys. Rev. Lett. 110, 152301 (2013)
86. Measurement of electrons from beauty hadron decays in pp collisions at $\sqrt{s} = 7$ TeV, Physics Letters B 721 (2013) 13-23
87. Charged kaon femtoscopic correlations in pp collisions at $\sqrt{s} = 7$ TeV, Phys. Rev. D 87, (2013) 05
88. Centrality Dependence of Charged Particle Production at Large Transverse Momentum in Pb-Pb Collisions at $\sqrt{s_{NN}} = 2.76$ TeV, Physics Letters B 720 (2013), pp. 52-62

89. Transverse Momentum Distribution and Nuclear Modification Factor of Charged Particles in p-Pb Collisions at $\sqrt{s_{NN}} = 5.02$ TeV, Phys. Rev. Lett. 110, 082302 (**2013**)
90. Coherent J/ψ photoproduction in ultra-peripheral Pb-Pb collisions at $\sqrt{s_{NN}} = 2.76$ TeV, Physics Letters B Volume 718, Issues 4-5, 29 January **2013**, Pages 1273-1283
91. Anisotropic flow of charged hadrons, pions and (anti-)protons measured at high transverse momentum in Pb-Pb collisions at $\sqrt{s_{NN}} = 2.76$ TeV, Phys. Lett. B 719 (**2013**) 18
92. Pseudorapidity density of charged particles in p-Pb collisions at $\sqrt{s_{NN}} = 5.02$ TeV, Phys. Rev. Lett. 110, 032301 (**2013**)
93. Long-range angular correlations on the near and away side in p-Pb collisions at $\sqrt{s_{NN}} = 5.02$ TeV, Physics Letters B 719 (**2013**), pp. 29-41
94. Charge separation relative to the reaction plane in Pb-Pb collisions at $\sqrt{s_{NN}} = 2.76$ TeV, Phys. Rev. Lett. 110 (**2013**) 012301
95. Measurement of electrons from semileptonic heavy-flavour hadron decays in pp collisions at $\sqrt{s} = 7$ TeV, Phys. Rev. D 86, 112007 (**2012**)
96. Measurement of the Cross Section for Electromagnetic Dissociation with Neutron Emission in Pb-Pb Collisions at $\sqrt{s_{NN}} = 2.76$ TeV, Phys. Rev. Lett. 109, 252302 (**2012**)
97. Pion, Kaon, and Proton Production in Central Pb-Pb Collisions at $\sqrt{s_{NN}} = 2.76$ TeV, Phys. Rev. Lett. 109, 252301 (**2012**)
98. Inclusive J/ψ production in pp collisions at $\sqrt{s} = 2.76$ TeV, Phys. Lett. B 718 (**2012**) 295

99. D_s meson production at central rapidity in proton–proton collisions at $\sqrt{s} = 7$ TeV, Physics Letters B 718 (2012), pp. 279-294
100. Measurement of prompt J/ψ and beauty hadron production cross sections at mid-rapidity in pp collisions at $\sqrt{s} = 7$ TeV, JHEP 11 (2012) 065
101. Rapidity and transverse momentum dependence of inclusive J/ψ production in pp collisions at $\sqrt{s} = 7$ TeV, Physics Letters B 718 (2012) 692-698
102. Production of $K^*(892)^0$ and $\phi(1020)$ in pp collisions at $\sqrt{s} = 7$ TeV, Eur. Phys. J. C 72 (2012) 2183
103. $K_s^0 - K_s^0$ correlations in 7 TeV pp collisions from the LHC ALICE experiment, Physics Letters B 717 (2012) pp. 151-161
104. Neutral pion and η meson production in proton-proton collisions at $\sqrt{s} = 0.9$ TeV and 7 TeV, Physics Letters B 717 (2012), pp. 162-172
105. Suppression of high transverse momentum prompt D mesons in central Pb-Pb collisions at $\sqrt{s_{NN}} = 2.76$ TeV, JHEP 9 (2012) 112
106. Production of muons from heavy flavour decays at forward rapidity in pp and Pb-Pb collisions at $\sqrt{s_{NN}} = 2.76$ TeV, Phys. Rev. Lett. 109, 112301 (2012)
107. Transverse sphericity of primary charged particles in minimum bias proton-proton collisions at $\sqrt{s} = 0.9, 2.76$ and 7 TeV, Eur. Phys. J. C (2012) 72:2124
108. J/ψ suppression at forward rapidity in Pb-Pb collisions at $\sqrt{s_{NN}} = 2.76$ TeV, Phys. Rev. Lett. 109, 072301 (2012)

109. Measurement of charm production at central rapidity in proton proton collisions at $\sqrt{s} = 2.76$ TeV, JHEP 1207 (2012) 191
110. Underlying Event measurements in pp collisions at $\sqrt{s} = 0.9$ and 7 TeV with the ALICE experiment at the LHC, JHEP 1207 (2012) 116
111. Multi-strange baryon production in pp collisions at $\sqrt{s} = 7$ TeV with ALICE, Phys. Lett. B 712 (2012) 309
112. J/ψ Production as a Function of Charged Particle Multiplicity in pp Collisions at $\sqrt{s} = 7$ TeV, Phys. Lett. B 712 (2012) 165-175
113. Light vector meson production in pp collisions at $\sqrt{s} = 7$ TeV, Physics Letters B 710 (2012), pp. 557-568
114. Measurement of Event Background Fluctuations for Charged Particle Jet Reconstruction in Pb-Pb collisions at $\sqrt{s_{NN}} = 2.76$ TeV, JHEP 03 (2012) 053
115. Particle-yield modification in jet-like azimuthal di-hadron correlations in Pb-Pb collisions at $\sqrt{s_{NN}} = 2.76$ TeV, Phys. Rev. Lett. 108, 092301 (2012)
116. Heavy flavour decay muon production at forward rapidity in proton-proton collisions at $\sqrt{s} = 7$ TeV, Phys. Lett. B 708 (2012) 265
117. Harmonic decomposition of two-particle angular correlations in Pb-Pb collisions at $\sqrt{s_{NN}} = 2.76$ TeV, Phys. Lett. B 708 (2012) 249-264
118. J/ψ polarization in pp collisions at $\sqrt{s} = 7$ TeV, Phys.Rev.Lett. 108 (2012) 082001

Conferences

1. XXII DAE-BRNS High Energy Physics Symposium, 12th-16th December 2016, University of Delhi, Delhi, India
Poster Presentation: Production of D-mesons in p+p and p+Pb collisions at LHC energies.
2. 7th International Conference On Physics And Astrophysics Of Quark Gluon Plasma, 2nd – 6th February 2015, VECC, Kolkata, India
Poster Presentation: Collective Flows at RHIC Energies Using Dynamical Simulation Model.
3. XXI DAE-BRNS High Energy Physics Symposium, 8th-12th December 2014, IIT Guwahati, India
Poster Presentation: Study of $\Lambda(1520)$ production in pp and p-Pb collisions with the ALICE experiment at the LHC
4. XXIV International Conference on Ultra-relativistic Nucleus-Nucleus Collisions (Quark Matter 2014), 19th – 24th May, 2014, Darmstadt, Germany
Poster Presentation: Study of $\Lambda(1520)$ resonance production with the ALICE experiment at the LHC
5. Triggering Discoveries in High Energy Physics, 9th – 14th September 2013, University of Jammu, India
6. VIIIth SERC School On Experimental High Energy Physics, 20th June to 10th July 2011, VECC, Kolkata, INDIA
7. 6th International Conference On Physics And Astrophysics Of Quark Gluon Plasma, 2010, Goa, India

Acknowledgements

I would like to thank many people who have inspired and helped me during my Ph.D. course. First and foremost, I would like to express my sincere gratitude to my thesis supervisor Prof. Pradip Kumar Sahu for giving me the opportunity to work on such fascinating subject. Because of him I could become a part of ALICE collaboration. I acknowledge him for his help and support at every step of my graduate study.

I would like to thank all the professors and fellow students of Institute of Physics, Bhubaneswar for creating a good ambiance of learning. I thank the European Organization for Nuclear Research (CERN) for giving me opportunities to use their facilities to carry out this research work. I would like to take the opportunity to acknowledge all of my collaborators of ALICE. I would like to thank all the resonance group convenors like Anders Garritt Knospe , Viktor Riabov, Francesca Bellini, Christina Markert and others for their guidance in my data analysis work. I really feel great for interacting with people from ALICE-INDIA collaboration like Prof. Tapan Nayak, Prof. Bedangadas Mohanty, Prof. D. P. Mahapatra, Prof. Anand Dubay and many more.

It was a great experience to be a part of the institute of Physics, Bhubaneswar. I was very lucky to have a nice colleagues like Shubhashis Rana, Sabita Das, Partha Bagchi and others in my batch. I specially thanks to Partha for his continuous help and moral support which made me feel like I was staying with my brother. I would like to thank Nihar Ranjan Panda being my friend from my M.Sc. and being a colleague in our group. I thank Srikanta Tripathy, colleague of our high energy group who was always pushing me to work faster. I really like his knowledge in many field besides Physics. Sarita Sahoo, colleague of our high energy group, contributed a lot for getting nice results

in ALICE data analysis and her efforts are very appreciable. I would like to thank Mohammed Younus (Post. Doc.), Srikanta for the collaboration work on D mesons. Also, many thanks to my supervisor for the work on compact stars. Younus, Srikant, Mriganka Mondal (Post. Doc.) and Sarita helped me a great for my synopsis presentation and thesis correction. So I really thankful to them and specially thanks to Mriganka for rechecking my whole thesis. I would also thanks Aditya Mishra, IIT Indore, who made my first CERN visit very comfortable and memorable. Before recalling any body else, I would like to thank and appreciate Dr. Ajay Kumar Dash, my senior in IOP, who has been helping me in research work till now.

I would like to thank my institute official staffs for their support in official work. I would like to thank our mess cooks Gokuli, Swain, Bijaya and others for preparing homely foods. I would like to thank all my IOP colleagues with whom I had spent memorable moments.

Last but not least, I would like to thank my parents and elder father and elder mother for taking my care and supporting all my wanting in my life. I specially thank my schoolmate, my friend, my colleague and finally my wife Mrs. Sarita Sahoo for her moral support, her encouragement in research, her caring and many more.

There are many more people that I would like to thank in helping me get to this point. There is certainly not enough space here to do everyone justice though I hope that my profound appreciation is understood.

SYNOPSIS

The main goal of the relativistic heavy ion collisions is to study nuclear matter under extreme conditions of temperature and density. Lattice QCD predicts that at sufficiently high temperature and/or nuclear density, colored quarks and gluons, which are confined in a hadron become de-confined resulting in a new phase of matter, called the Quark Gluon Plasma (QGP). In a QGP phase, quarks and gluons are able to move over regions larger than a hadronic length. The QGP is believed to have existed in the early Universe, when the universe was a few microseconds old. Understanding the properties of QGP could provide valuable insights on the evolution of our universe. Since the evolution of this hot and dense matter happens within few fm/ c , we need different probes to investigate different phases of evolution; cold and hot nuclear matter effects on final observed spectra of particles, initial anisotropy and its effect on collective motion of final state particles, and so on.

Some hadronic resonance states due to their short lifetimes (\sim few fm/ c) are important to investigate some properties like the time span of the hadronic scattering medium formed in relativistic heavy-ion collisions. In particular, the $\Lambda(1520)$ (commonly known as Λ^*) baryonic resonance is important because its lifetime (~ 12.6 fm/ c) is comparable to the time scale of the hot and dense matter produced in heavy-ion collisions. The characteristic properties such as mass, width, yield and transverse momentum spectra of Λ^* may be very sensitive to the dynamics and in-medium effects. Basically the decay products of Λ^* , the protons and kaons, may undergo in-medium effects such as re-scattering. The re-generation process (pseudo-elastic interactions; $p + K \rightarrow \Lambda^* \rightarrow p + K$) may compensate for the Λ^* yield, lost in re-scattering, if the system formed has a long expansion time.

Another effect on final state particle spectra in heavy ion collisions are cold and hot nuclear matter effects. Hadron spectra in heavy ion collisions are observed to be highly suppressed relative to those in p+p collisions. It has been suggested that the modification in spectra of the observed particles in the heavy ion collision have effects of cold nuclear matter before formation of QGP which are often masked by hot and dense matter effects. In order to account all these effects in hot and dense matter , it is absolute necessary to fix the baseline for such observations. So the first aim of this thesis is to study on the existence of any hadronic scattering medium that can affect Λ^* yield in p-Pb collision system at $\sqrt{s_{NN}} = 5.02$ TeV, where we do not expect any hot nuclear matter effect. Then we calculate cold nuclear matter effect on D-meson production in the same system using different simulation model.

In the first part of this thesis, we have studied on Λ^* resonance in pp collisions at $\sqrt{s} = 7$ TeV and in p-Pb collisions at $\sqrt{s_{NN}} = 5.02$ TeV in the rapidity ranges $-0.5 < y < 0.5$ and $-0.5 < y < 0$, respectively, in the center of mass frame. The $\langle p_T \rangle$ and dN/dy has been calculated in minimum bias pp and p-Pb collisions. Also we have calculated those in four multiplicity bins in p-Pb system; 0-20%, 20-40%, 40-60% and 60-100%. These values are compared with the same results of Λ^* in pp collisions at $\sqrt{s} = 200$ GeV (PRL 97,132301(2006), STAR experiment). The ratio of Λ^* over $\Lambda(1115)$ (ground state particle) has been calculated in all multiplicity bins in p-Pb collisions and in minimum bias pp collisions. Published result from ALICE predicts a hadronic scattering medium which affects more the K^* yield when one goes from lower to higher multiplicity bins. However we have found that Λ^* over Λ ratio stays flat over all multiplicity bins in p-Pb system and matches with the same result in pp collision. This suggests that the lifetime of the hadronic medium in p-Pb collisions is not so long to affect the yield of Λ^* . We have

found that the prediction of Λ^*/Λ from statistical hadronisation model agrees within uncertainty with the the results from pp collision.

In the second part we have studies the cold nuclear matter effect on D-mesons production (D^0 , D^+ and D^{*+}) in p-Pb collisions at $\sqrt{s_{NN}} = 5.02$ TeV using different simulation models (HIJING, AMPT, NLO (MNR) and FONLL) and compared the results with ALICE data. We have calculated the p_T -differential production cross-section of different D-mesons using all four model in both the said collision systems and compared with the ALICE published results. We have found most of the model are able to explain the data within uncertainties. HIJING under-predict the cross-section in p-Pb collisions at lower and intermediate p_T regions whereas NLO over-predicts the cross-section in higher p_T end. We have calculated nuclear modification factor from all the models and found that all the systems predicts a cold nuclear matter effect for p-Pb collisions at $\sqrt{s_{NN}} = 5.02$ TeV.

In the last part of the thesis, as an application to astrophysical bodies, we have studied the different modes of radial oscillations of compact stars by inclusion of hyperons in presence of magnetic field. Compact stars are classified into three categories: neutron stars (NSs), quark stars (Qs) and hybrid stars (HSs). Stars having only hadronic matter are NSs, Qs having only quark matter up to u, d and s quarks and stars having quark core surrounded by a mixed matter (hadronic matter and quark matter) followed by hadronic matter are HSs. A huge magnetic field is predicted to be persisting in the core of the neutron star and is observed in the surface of the neutron star. We have studied the effect of such huge magnetic field in the matter inside the compact objects basically the equation of state (EOS) of the matters. Since matter inside the star are very dense for both hadronic and quark matter, we have considered relativistic mean field theory in the hadronic matter and simple MIT bag model

in the quark matter in the presence of strong magnetic field. We have calculated the phase transition between hadronic and quark phases, maximum mass and eigenfrequencies of radial pulsation of NS, HS and QS in the presence of such a huge magnetic field. The mixed phase have been constructed by using Glendenning conjecture in between hadron and quark phases. We have found in the presence of magnetic field, the EOS in both matter becomes soft. As a result, the maximum mass has reduced and the period of radial oscillation has changed significantly and there is a sudden dip in the period of radial oscillations in the HS, which signifies the transition from one to another matter.

List of Figures

1.1	(Color Online) The fundamental particles and the force-mediating bosons of Standard Model. Data values of the figure are taken from [9]	2
1.2	(Color Online) The QCD phase diagram [16]	5
1.3	(Color Online) Ratios of the mid-rapidity p_T -integrated yields for different hadron species measured by the STAR experiment for Au+Au collisions at $\sqrt{s_{NN}} = 200$ GeV (circles). The horizontal lines represent statistical model fits to the measured particle yield ratios. The inset shows the extracted variation of γ_S as a function of centrality. Plot taken from [31].	9
1.4	(Color Online) Fit of the hadron yields measured in ALICE with statistical hadronization model [37]. The K^{*0} is not included in fit.	10
1.5	T_{kin} vs. β_T extracted by a simultaneous fit to the pion, kaon and proton spectra, measured in ALICE and STAR experiment, to a Blast Wave function. [37, 38]	11
1.6	The left plot shows R_{AA} and right plot shows R_{CP} for charged hadrons for different centralities measured by STAR collaboration for Au-Au collisions at $\sqrt{s_{NN}} = 200$ GeV. The shaded bands indicate the systematic uncertainty related to the number of participant and number of binary collision scaling calculations. [42]	12
1.7	(Color Online) Nuclear modification factor in Pb-Pb at $\sqrt{s_{NN}} = 2.76$ TeV and p-Pb collisions at $\sqrt{s_{NN}} = 5.02$ TeV.[43, 44]	13

List of Figures

1.8	(Color Online) Strangeness enhancement for multi-strange hadrons measured in SPS[45] (on right plot shown by faint open markers), RHIC[46] (on right plot shown by dark open markers) and LHC [47] energies (on both plots shown by solid markers). Blue, red and black markers are for Ω , Ξ and Λ , respectively. . . .	14
1.9	(Color Online) v_2 , v_3 and v_4 coefficients measured for charged particles as a function of p_T for various centrality classes [50]. The dashed line represents the WHDG model calculations for neutral pions v_2 [51] extrapolated to the LHC collision energy. For clarity, the markers for v_3 and v_4/ψ_2 results are slightly shifted along the horizontal axis. Error bars (shaded boxes) represent the statistical (systematic) uncertainties.	15
1.10	(Color Online) Schematic diagram of re-scattering and re-generation of resonances (here Λ^*) during hadronic scattering medium in heavy ion collision.	19
1.11	Schematic diagram of the nuclear modification of bound nucleons.[72, 73]	21
2.1	(Color online) CERN accelerator complex at the LHC [83]	28
2.2	(Color online) Schematic diagram of the ALICE detector. [87]	33
2.3	Layout of ITS detector	35
2.4	Conceptual view of the TPC, showing the dimensions and components. [92]	36
2.5	(Color online) The measured energy loss dE/dx vs momentum using TPC in Pb-Pb collisions at $\sqrt{s_{NN}} = 2.76$ TeV.	38
3.1	(Color online) The Z- position of vertex in pp (left) and in p-Pb (right) collisions.	46
3.2	(Color online) Multiplicity distribution in % of the accepted events in the range 0-100%..	47
3.3	(Color online) The quality assurance plots for DCA cuts along z-axis (on left) and in xy-plane (right) are shown from in p-Pb collisions data.	48

3.4	(Color online) $n\sigma$ of TPC tracks as proton on left and as kaon on right. The areas within the solid black lines are showing the region of PID selection from the TPC detector.	50
3.5	(Color online) $n\sigma$ of TOF tracks as proton on left and as kaon on right. The areas within the solid black lines are showing the region of PID selection from the TOF detector.	50
3.6	(Color online) In upper plot, the US distribution is shown by black solid markers, normalised MEB and LSB are shown by open red and open blue markers. In lower two plots it shows signal peaks after subtracting MEB (left) and LSB (right) by black solid markers. The solid red and blue lines show the Voigtian fits to the signal peaks and the dashed red and blue lines show the polynomial fits to the residual backgrounds, respectively. This is for pp collisions at $\sqrt{s} = 7$ TeV.	52
3.7	(Color online) The plot shows the mass resolution for Λ^* in pp (blue solid marker) and p-Pb (red solid marker) collisions in different p_T bins.	54
3.8	(Color online) These plots show Λ^* signal after subtracting MEB in different p_T bins in pp collisions at $\sqrt{s} = 7$ TeV.	55
3.9	(Color online) These plots show Λ^* signal after subtracting MEB in different p_T bins in p-Pb minimum bias collisions at $\sqrt{s_{NN}} = 5.02$ TeV.	55
3.10	(Color online) These plots show Λ^* signal after subtracting MEB in different p_T bins in p-Pb collisions at $\sqrt{s_{NN}} = 5.02$ TeV for 0-20% multiplicity bin.	56
3.11	(Color online) These plots show Λ^* signal after subtracting MEB in different p_T bins in p-Pb collisions at $\sqrt{s_{NN}} = 5.02$ TeV for 20-40% multiplicity bin.	56
3.12	(Color online) These plots show Λ^* signal after subtracting MEB in different p_T bins in p-Pb collisions at $\sqrt{s_{NN}} = 5.02$ TeV for 40-60% multiplicity bin.	57
3.13	(Color online) These plots show Λ^* signal after subtracting MEB in different p_T bins in p-Pb collisions at $\sqrt{s_{NN}} = 5.02$ TeV for 60-100% multiplicity bin.	57

List of Figures

3.14	(Color online) The blue and red circles show the reconstruction efficiency×acceptance for pp collisions and p-Pb collisions, respectively.	59
3.15	(Color online) Red line shows the total systematic uncertainties and blue line shows the statistical uncertainties for minimum bias p-Pb collisions on the left plot and for minimum bias pp collisions on the right plot in different p_T bins. . .	62
3.16	(Color online) The left and on the right plots show the mass and width of Λ^* , respectively. The shadowed bands show their respective PDG values.	63
3.17	(Color online) In the figure, the black markers show the p_T -spectrum of Λ^* in pp collisions at $\sqrt{s} = 7$ TeV and is fitted with Tsallis-Levy (green), BG blastwave (blue), m_T exponential (violet) and Boltzmann (magenta) functions.	64
3.18	(Color online) In the figure, the black markers show the p_T -spectrum of Λ^* in minimum bias p-Pb collisions at $\sqrt{s_{NN}} = 5.02$ TeV and is fitted with Tsallis-Levy (red), BG blastwave (black), m_T exponential (blue) and Boltzmann (magenta) functions.	65
3.19	(Color online) Same as Fig. 3.18, but for 0-20% multiplicity bin.	66
3.20	(Color online) Same as Fig. 3.18, but for 20-40% multiplicity bin.	66
3.21	(Color online) Same as Fig. 3.18, but for 40-60% multiplicity bin.	67
3.22	(Color online) Same as Fig. 3.18, but for 60-100% multiplicity bin.	67
3.23	(Color online) The figure shows p_T spectra of Λ^* in p-Pb collisions for minimum bias (magenta), 0-20% (black), 20-40% (red), 40-60% (green) and 60-100% (blue) multiplicity bins. All spectra are fitted separately with Tsallis-Levy function. . .	68
3.24	(Color online) The left plot shows the $\langle p_T \rangle$ of Λ^* (red marker) versus energy in pp collisions. The right plot shows dN/dy of Λ^* versus energy in pp collisions. [110]	70

- 3.25 (Color online) The figure shows the $\langle p_T \rangle$ of different particles having different masses. Red solid markers, green solid circles and open red circles are showing the pp collision results published by ALICE at $\sqrt{s} = 7$ TeV , 2.76 TeV and 900 GeV , respectively. Star markers are showing the results of pp at $\sqrt{s} = 200$ GeV from STAR experiment. Dashed red line is showing the ISR parameterization [111]. 71
- 3.26 (Color online) The figure shows the ratio of $\Lambda(1520)$ yield and $\Lambda(1115)$ yield in pp collisions at $\sqrt{s} = 200$ GeV and 7 TeV by blue and green markers, respectively. Red line shows the prediction of statistical hadronization model [112]. 72
- 3.27 (Color online) The figure shows the measured values of dN/dy for Λ^* in p-Pb collisions for minimum bias (blue solid markers), multiplicity bins (black solid markers) and in pp collisions (solid green markers). 72
- 3.28 (Color online) The figure shows the measured values of $\langle p_T \rangle$ for Λ^* (black), Ω (red), Ξ^* (green), Σ (blue), ϕ (magenta) and K^* (cyan) in p-Pb collisions. 73
- 3.29 (Color online) The figure shows the ratio of $\Lambda(1520)$ yield over $\Lambda(1115)$ yield in p-Pb collisions at $\sqrt{s_{NN}} = 5.02$ TeV by black solid markers and same in pp collisions at $\sqrt{s} = 200$ GeV and 7 TeV by green and red markers, respectively. Red band shows the prediction of statistical hadronization model. 73
- 3.30 (Color online) Ratio of K^{*0} and ϕ to charged K measured in the three collision systems, as a function of the cube root of the average charged particle density ($\langle dN_{ch}/d\eta_{lab} \rangle^{1/3}$) measured at mid-rapidity, used as a proxy for the system size. Squares represent K^{*0}/K , circles refer to ϕ/K . Statistical uncertainties (bars) are shown together with total (hollow boxes) and multiplicity-uncorrelated (shaded boxes) systematic uncertainties. Measurements in pp at $\sqrt{s} = 7$ TeV and Pb-Pb collisions at $\sqrt{s_{NN}} = 2.76$ TeV are taken from [114] and [115], respectively. 74

List of Figures

4.1	(Color online) p_T differential inclusive production cross-section of D-meson in pp collisions at $\sqrt{s} = 7$ TeV. Solid markers represent the ALICE data points [166]. Statistical errors are in bars while systematic errors are in boxes. Small dash-dotted magenta line, dashed green line, long dash-dotted blue line and solid red line represent HIJING, AMPT, NLO and FONLL results, respectively.	88
4.2	(Color online) p_T differential inclusive production cross-section of D mesons in p-Pb data at $\sqrt{s_{NN}} = 5.02$ TeV. Solid markers represent the ALICE data points[167]. Statistical errors are in bars while systematic errors are in boxes. Small dash-dotted magenta line, green dashed line, blue long dash-dotted line and red solid line represent HIJING, AMPT, NLO and FONLL results, respectively.	89
4.3	(Color online) Nuclear modification factor for D-meson in p-Pb $\sqrt{s_{NN}} = 5.02$ TeV. Solid markers represent the ALICE data points [167]. Statistical errors are in bars while systematic errors are in boxes. Magenta dotted line, green dashed line, red dash-dotted line, cyan solid line and blue solid line represent HIJING, AMPT, FONLL, NLO and NLO with Cronin K_T brodening results, respectively.	90
5.1	pressure against energy density for zero and non zero value of magnetic field. $B=0$ (solid line) and $B=2 \times 10^{15}G$ with $alpha = 0.005$ (dotted line).	99
5.2	Top figure is the maximum gravitational mass against central energy density for both zero and non zero magnetic field. $B=0$ (solid line) and $B=2 \times 10^{15}$ G (dotted line). Bottom figure is the period of oscillation in seconds against gravitational mass in solar mass for zero and non zero value of magnetic field. $B=0$ (solid line) and $B=2 \times 10^{15}G$ with $\alpha = 0.005$ (dotted line) for fundamental mode (1) and higher harmonics (2-5).	100

- 5.3 Figure shows the pressure against energy density for zero and non zero value of magnetic field. Solid green and black lines ($B=0$) and dashed blue and red lines ($B=2 \times 10^{15}G$ with $\alpha = 0.005$) are for density dependent bag pressure $B_G = 160 \text{ MeV/fm}^3$ and $B_G = 170 \text{ MeV/fm}^3$, respectively, for fixed value of $\beta = 2$ 104
- 5.4 Left figure is the maximum gravitational mass against central energy density for both zero and non zero magnetic field for density dependent bag pressure $B_G = 170 \text{ MeV/fm}^3$. Solid lines and dashed lines are the representations in absence and presence of magnetic field, respectively. Right figure shows the period of oscillation in seconds against gravitational mass in solar mass unit for zero and non zero value of magnetic field ($B=2 \times 10^{15}G$ with $\alpha = 0.005$), for density dependent bag pressure $B_G = 170 \text{ MeV/fm}^3$. Solid lines and dashed lines correspond to the absence and presence of magnetic field, respectively and are representing fundamental mode (1) and higher harmonics (2-5). 104
- 5.5 Same as figure 5.4, but for density dependent bag pressure $B_G = 160 \text{ MeV/fm}^3$ 105
- 5.6 Figure shows pressure against energy density for zero (green and black solid lines are for $B_G = 170 \text{ MeV/fm}^3$ and $B_G = 160 \text{ MeV/fm}^3$, respectively) and non zero (blue and red dashed lines are for $B_G = 170 \text{ MeV/fm}^3$ and $B_G = 160 \text{ MeV/fm}^3$, respectively) values of magnetic field. $B = 2 \times 10^{15}G$ with $\alpha = 0.005$ 108
- 5.7 Left panel of figure shows gravitational mass in solar mass unit against central energy density for zero (solid line) and non zero (dashed line) value of magnetic field $B = 2 \times 10^{15}G$ with $\alpha = 0.005$. Here the density dependent bag pressure B_G is 170 MeV/fm^3 . Right panel of figure shows period of oscillation in seconds against gravitational mass in solar mass unit for zero and non zero values of magnetic field. $B=0$ (solid lines) and $B = 2 \times 10^{15}G$ (dashed lines) for fundamental mode (1) and higher harmonics (2-5) with density dependent bag pressure B_G is 170 MeV/fm^3 109
- 5.8 Same as Fig 5.7, but for the density dependent bag pressure B_G is 160 MeV/fm^3 109

List of Tables

1.1	List of resonances with their hadronic (dominant) decay channel, branching ratio, decay width and decay length. [62]	18
2.1	Summary of the ALICE detector subsystems. The position is the approximate distance from the interaction point to the face of the detector and corresponds to the radius for barrel detectors (inner and outer radius for the TPC and TRD) or the position along the beam (z coordinate) for the others. [89, 90]	34
3.1	Tsallis-Levy fit parameters to Λ^* spectra in pp and p-Pb collisions.	69
3.2	Boltzmann Gibbs Blast-Wave fit parameters to Λ^* spectra in pp and p-Pb collisions.	69
3.3	dN/dy and $\langle p_T \rangle$ of Λ^* in pp and p-Pb collisions from Tsallis-Levy fit.	70

Contents

List of Publications	ix
Acknowledgements	xxiii
Synopsis	xxv
List of Figures	xxxvi
List of Tables	xxxvii
Contents	xlii
Chapter 1 Introduction	1
1.1 The Standard Model	1
1.2 Deconfinement in QCD	3
1.3 QCD Phase Diagram	4
1.4 Experimental Facilities of Hadron Colliders	6
1.5 Experimental Observables for QGP	8
1.5.1 Particle Yields and Transverse Momentum Spectra	8
1.5.2 Nuclear Modification Factor	11
1.5.3 Strangeness Enhancement	13

Contents

1.5.4	Anisotropic Flow	14
1.5.5	Heavy Flavour	16
1.6	Resonance Production and In-Medium Effects	17
1.6.1	History on Resonances	17
1.6.2	Resonance In-Medium Effects	18
1.6.3	Re-scattering Effect and Re-generation Effect	18
1.7	Heavy-Flavour Production in p-Pb Collisions	20
1.7.1	Initial-State Effects and the Role of p-A Collisions	20
1.8	Phase Transition in Compact Stars	22
1.8.1	Compact Stars	22
1.8.2	Phase Transition in Compact Stars	23
1.9	About the Thesis	24
Chapter 2 A Large Ion Collider Experiment at the LHC		27
2.1	The Large Hadron Collider	27
2.1.1	ALICE at the LHC	32
2.2	The ALICE Detector	32
2.2.1	The Inner Tracking System	34
2.2.2	The Time Projection Chamber	36
2.2.3	The Transition Radiation Detector	38
2.2.4	The Time Of Flight	39
2.2.5	V0 and T0	40
2.2.6	Zero Degree Calorimeter	40
2.2.7	The Muon spectrometer	41
2.2.8	The Photon Multiplicity Detector	41
2.2.9	ALICE COsmic Ray DEtector	42
2.3	ALICE Online and Trigger	42

2.3.1	DAQ	42
2.3.2	CPT	43
2.3.3	HLT	43
Chapter 3 Measurement of $\Lambda(1520)$ resonance production in pp and p-Pb collisions		45
3.1	Introduction	45
3.2	Data sample and event selection	45
3.3	Track Selection	47
3.4	Particle identification with TPC and TOF	49
3.5	Raw yield extraction	51
3.6	Raw yield correction	58
3.7	Systematic uncertainties	60
3.8	Results	63
3.8.1	Mass and Width	63
3.8.2	Transverse momentum spectra	63
3.8.3	Yield and mean transverse momentum	69
3.8.4	Comparison and ratio	69
3.9	Summary	75
Chapter 4 Production of D mesons in pp and p-Pb collisions at the LHC energies		77
4.1	Introduction	77
4.2	Models used	80
4.2.1	The HIJING model	80
4.2.2	The AMPT model	81
4.2.3	The NLO model	82
4.2.4	The FONLL model	86

Contents

4.3	Results and discussion	87
4.4	Summary	91
Chapter 5	Phase transition in magnetized compact stars	93
5.1	Introduction	93
5.2	Radial pulsation of non-rotating star	95
5.3	Magnetic field in hadronic phase	97
5.4	Magnetic field in quark phase	102
5.5	Phase transition and mixed phase	107
5.6	Summary	112
Chapter 6	Summary and Outlook	115
6.1	Summary	115
6.2	Future Prospective	117
References		119

1 Introduction

All known matter of the Universe today is made up of quarks and leptons, held together by fundamental forces which are governed by the exchange of particles known as gauge bosons. The Standard Model which is the theory of the elementary particles and their fundamental interactions provides a remarkable insights into the fundamental structure of matter [1]. This model was proposed by Glashow, Salam and Wienberg in 1970 [2, 3, 4] and is applicable over a wide range of conditions in explaining experimental results with very high precision.

In the early 1970s, Fritzsche, Gell-Mann and Leutwyler modelled the strong interaction using a Yang-Mills gauge quantum field theory with coloured quarks and an octet of coloured gluons [5]. In this non-abelian theory the force-mediating gluons also carry colour charge and could undergo self-interactions, unlike in quantum electrodynamics (QED), where the photon carries no electric charge. Shortly afterwards, Gross, Wilczek and Politzer [6, 7, 8] discovered that non-abelian gauge theories have the feature of asymptotic freedom.

1.1 The Standard Model

The high-energy physics has validated the standard model and confirmed its predictions through a large variety of experiments. The collisions between

1 Introduction

relativistic heavy ions allow to study the nuclear matter under the conditions of extremely high temperature and high energy density. In these conditions, the Standard Model predicts that the nuclear matter can undergo a new state of matter, where the quarks and the gluons are expected to be deconfined.

Standard model depicts the elementary particles can be categorized into 6 quarks, 6 leptons, 4 gauge bosons and the recently discovered Higgs boson. Each group of quarks and leptons can be subdivided into generations. The six quarks are paired into three generations: the up (u) and down (d) quarks are belong to the first generation; the charm (c) and strange (s) are from second generation; and the top (t) and bottom (b) are the third generation. The leptons are also arranged into three generations: the electron (e) and electron neutrino (ν_e); the muon (μ) and muon neutrino (ν_μ); the tau (τ) and tau neutrino (ν_τ). Each quarks and leptons also have their corresponding anti-particle. There

Three Generations
of Matter (Fermions)

	I	II	III	
mass→	2.4 MeV	1.27 GeV	171.2 GeV	0
charge→	$\frac{2}{3}$	$\frac{2}{3}$	$\frac{2}{3}$	0
spin→	$\frac{1}{2}$	$\frac{1}{2}$	$\frac{1}{2}$	1
name→	u up	c charm	t top	γ photon
				H Higgs
Quarks	4.8 MeV $-\frac{1}{3}$ $\frac{1}{2}$ d down	104 MeV $-\frac{1}{3}$ $\frac{1}{2}$ s strange	4.2 GeV $-\frac{1}{3}$ $\frac{1}{2}$ b bottom	0 0 1 g gluon
	<2.2 eV 0 $\frac{1}{2}$ ν_e electron neutrino	<0.17 MeV 0 $\frac{1}{2}$ ν_μ muon neutrino	<15.5 MeV 0 $\frac{1}{2}$ ν_τ tau neutrino	91.2 GeV 0 1 Z weak force
Leptons	0.511 MeV -1 $\frac{1}{2}$ e electron	105.7 MeV -1 $\frac{1}{2}$ μ muon	1.777 GeV -1 $\frac{1}{2}$ τ tau	80.4 GeV ± 1 1 W weak force
				Bosons (Forces)

Figure 1.1: (Color Online) The fundamental particles and the force-mediating bosons of Standard Model. Data values of the figure are taken from [9]

are four fundamental forces at work in the universe namely the strong force, the weak force, the electromagnetic force and the gravitational force. These

fundamental forces result from the exchange of mediator particles called gauge bosons. Each of the fundamental force has its mediator(s); the strong force is mediated by the exchange of gluons (g), the weak force is carried by W^\pm and Z^0 bosons, the photon (γ) is responsible for the electromagnetic force and the graviton is supposed to be the corresponding carrier for gravitational force. But the gravity does not fit comfortably into the standard model. More importantly, the standard model also predicts the existence of Higgs boson [10, 11] which is responsible for the generation of mass for the subatomic particles. The ATLAS [12] and CMS [13] experiments at the CERN LHC announced the experimental evidence of Higgs like particle around the mass region of 126 GeV. Francois Englert and Peter Higgs, for their independent contribution to the theory of Higgs mechanism for the generation of mass of sub-atomic particles, were awarded with the 2013 Nobel prize.

1.2 Deconfinement in QCD

The strong force couples to the colour charge of the quarks and is the force which keeps the quarks inside the nucleons and binds the nucleons together inside the nuclei of atoms. The strong interaction exhibits two interesting features: confinement and asymptotic freedom. At large distances or small momentum (Q^2) transfers, the coupling strength (α_s) of the strong interaction, is very large and increases as the distance between two quarks increases. This phenomenon is called confinement and is the reason that quarks are never found single but are instead always bound together in groups of three (baryons) or as quark-antiquark pairs (mesons). Asymptotic freedom describes the feature that the coupling between quarks becomes small when the distances between the quarks are small i.e. when the momentum transfer is large. In other

words, at asymptotically high energies, α_s tends to zero and the quarks behave like free particles. So the effective strength of the interaction between quarks and gluons depends on their interaction condition.

The QCD coupling constant, α is related to the scale of momentum transfer Q and is given by the relation [14]

$$\alpha_s(Q^2) \sim \frac{12\pi}{(33 - 2n_f)\ln(Q^2/\Lambda^2)} \quad (1.1)$$

where n_f is the number of quark flavours and Λ is the scale parameter. During asymptotic freedom, the coupling constant is small, so perturbative QCD (pQDC) is a good description for this situation. Otherwise, when distance increases a nonperturbative treatment is necessary to describe the coupling force.

1.3 QCD Phase Diagram

Thermodynamic properties of a system are expressed in terms of a phase diagram in the space of thermodynamic parameters. In QCD, a space diagram in terms of temperature (T) and chemical baryonic potential (μ_B) (or net baryon density (ρ_B)) describes different thermodynamic phases. Each point on the diagram corresponds to a stable thermodynamic state, characterized by various thermodynamic functions. Figure 1.2 shows the QCD schematic phase diagram which depicts QCD matter at different temperatures and baryon densities. At sufficiently high temperature $T > T_c$, a plasma state of weakly interacting, deconfined quarks and gluons (QGP) is expected to exist. The QCD calculation on lattice at high temperature and zero baryonic density shows this transition is a cross-over [15].

But at high ρ_B and at low T , if baryonic chemical potential increases beyond a critical value, there is a possibility of formation of baryon rich quark-gluon

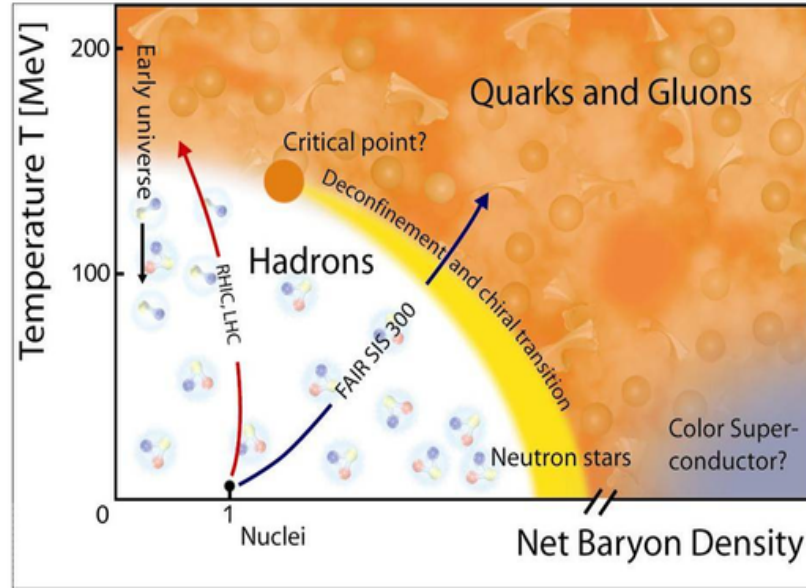


Figure 1.2: (Color Online) The QCD phase diagram [16]

plasma. This phase transition may correspond to 1st order phase transition. We may expect such plasma inside the core of neutron stars. Also at the same condition QCD calculation suggests that the quarks form a color superconducting phase [15]. In the region when $\mu/3$ (chemical potential for a quark) is not much greater than mass of s quark, then Fermi momentum of s quark (K_{Fs}) are much smaller than Fermi momentum of u and d quarks ($K_{Fu,d}$). So Cooper pairing is effectively restricted to the two light flavors. And the pairs condensate to form 2 flavor color superconducting (2SC) state. For larger μ , K_{Fs} should increase up to the point where s quarks can participate in the pairing. In this case a more symmetric “color-flavor-locked” (CFL) condensate can occur.

So by changing the temperature and baryon density, we can fetch a region where the first order phase transition stops and as we increase temperature, we have only a cross-over for this transition. But ALICE is doing experiments at such a high energy that the temperature is so high and only cross-over is the via for the hadronic matter to undergo quark degrees of freedom.

1.4 Experimental Facilities of Hadron Colliders

The Intersecting Storage Rings (ISR) [17], a particle accelerator at CERN, was composed of two interlaced rings with diameters of 150 metres. It was the world's first hadron collider, and ran from 1971 to 1984, with a maximum center of mass energy of 62 GeV. The ISR performed the first-ever proton-proton and proton-antiproton collisions. The Super Proton Synchrotron (SPS) [18, 19] is a particle accelerator at CERN having a circular tunnel of 6.9 kilometres (4.3 miles) in circumference. SPS can accelerate proton beam up to 450 GeV energy. It takes particles from the Proton Synchrotron and accelerates them to provide beams for the Large Hadron Collider, the NA61 and NA62 experiments, the COMPASS experiment and the CNGS project. W and Z boson particles were discovered by SPS in 1983 when the collider was running proton and antiproton. The Tevatron [20] which is a circular particle accelerator at the Fermi National Accelerator Laboratory (Fermilab) was the second most powerful accelerator. It was able to accelerate proton beam close to 1 TeV. The Relativistic Heavy Ion Collider (RHIC) [21], at Brookhaven National Laboratory (New York), is the one out of two heavy-ion colliders, and the only spin-polarized proton collider. It can collide heavy ion (Au) from 7.7 GeV to 200 GeV center of mass energy. RHIC can collide different types of particles like; *d-Au*, *Cu-Cu*, *Cu-Au*, *Au-Au*, *U-U* ($^{63}\text{Cu}^{29+}$, $^{197}\text{Au}^{79+}$, $^{238}\text{U}^{92+}$). There are mainly four experiments associated with RHIC: STAR (the Solenoidal Tracker At RHIC), PHENIX (Pioneering High Energy Nuclear Interaction eXperiment), BRAHMS (Broad RAnge Hadron Magnetic Spectrometers), PHOBOS. The evidence of RHIC experiments shows the existence of quark-gluon plasma. Their beam energy scan programme focus on the search of QCD critical point. The spin physics at RHIC works on missing proton spin by colliding

high energy beams of polarized protons.

The Large Hadron Collider (LHC) [22] is the world's largest and the most powerful particle accelerator which is 175 metres beneath the Franco-Swiss border near Geneva, Switzerland. Its inception was on 10th September 2008. The LHC consists of a 27 kilometre ring of superconducting magnets. Thousands of magnets of different varieties and sizes are used to direct the beams around the accelerator. These include 1232 dipole magnets 15 metres in length which bend the beams, and 392 quadrupole magnets, each 5–7 metres long, which focus the beams. Just prior to collision, another type of magnet is used to "squeeze" the particles closer together to increase the chances of collisions. The beams inside the ring can collide at four locations where four particle detectors are placed: They are ATLAS (A Toroidal LHC ApparatuS), CMS (Compact Muon Solenoid), LHCb (LHC-beauty) and ALICE (A Large Ion Collider Experiment). It allows physicists to test predictions from standard model, supersymmetric theories. The ATLAS and CMS experiments have presented their results on the mass of the Higg's boson on 2013. LHC has facility to collide pp, p-Pb and Pb-Pb ($^{208}\text{Pb}^{82}$) at center of mass energy of the order of TeV. Recently in 2015, it has enhanced its proton beam energy up to 6500 GeV. This thesis is partly based on the ALICE data at the LHC. ALICE is mainly focusing on the physics of strongly interacting matter at extreme energy densities. The Quark-Gluon Plasma (QGP) and its evolution properties are necessary to understand QCD phase transition and color confinement. ALICE data for Pb-Pb collisions at $\sqrt{s_{NN}} = 2.76$ TeV shows a strong evidence for the formation of QGP.

1.5 Experimental Observables for QGP

Since the hot and dense medium created in nucleus-nucleus collisions is extremely short-lived and only the final-state particles are measured in the detectors, so from final-state observables one extrapolate backwards to characterize the properties of the system at early times. The nature of the final-state of relativistic nucleus-nucleus collisions with their large particle multiplicities and variety of species of produced particles leads to a large range of experimental observables which can be used to probe and characterize the properties of the produced system. Many signatures of QGP formation and associated characteristics of the medium have been proposed ([23, 24]). For example, proposed signatures of deconfinement include suppression of charmonium production [25] and enhanced production of multi-strange particles [26] whereas modifications of meson masses has been predicted to be a signature of chiral symmetry restoration [27]. The properties of the hard/heavy probes may be modified by medium effects, for example, high- p_T partons (jets) lose energy as they traverse the dense medium, and measurements of the jet observables (after the parton fragments) may provide information on the medium density (i.e. gluon density). A selection of bulk observables and what information they can provide about the properties of the medium created in ultra-relativistic heavy-ion collisions are discussed in the following sections.

1.5.1 Particle Yields and Transverse Momentum Spectra

From nucleus-nucleus collisions, the yields and transverse momentum spectra for various particle species have been measured. Particle yields can provide information about the system from the time of chemical freeze-out when the

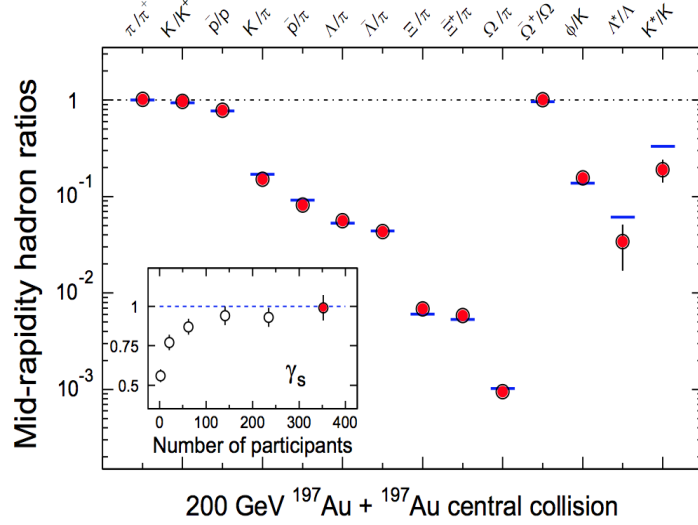


Figure 1.3: (Color Online) Ratios of the mid-rapidity p_T -integrated yields for different hadron species measured by the STAR experiment for Au+Au collisions at $\sqrt{s_{NN}} = 200$ GeV (circles). The horizontal lines represent statistical model fits to the measured particle yield ratios. The inset shows the extracted variation of γ_s as a function of centrality. Plot taken from [31].

inelastic collisions cease and the chemical abundances become fixed. Statistical Thermal Models ([28, 29, 30]), have been very successful in describing the particle ratios observed at RHIC and LHC using only a few model parameters (i.e. chemical freeze-out temperature T_{ch} , baryon and strangeness chemical potentials μ_B and μ_S and strangeness suppression factor γ_s) extracted from fitting to particle yield ratio data. Comparison of statistical model results to data from the STAR and ALICE experiment are presented in Fig. 1.3 and 1.4 [31, 37]. The Fig. 1.3 shows the integrated p_T yield ratios measured by the STAR experiment in Au+Au collisions at $\sqrt{s_{NN}} = 200$ GeV. The solid horizontal lines show the statistical model fits to the particle ratios [33] using only 3 parameters ($T_{ch} = 163 \pm 4$ MeV, $\mu_B = 24 \pm 4$ MeV, $\gamma_s = 0.99 \pm 0.07$). These values are similar to values obtained using different variations of the statistical model [34, 35] for RHIC data. The inset in the figure is the evolution of the strangeness suppression factor γ_s which is a measure of how far the system is from chemical equilibrium. For the most central collisions, the γ_s value

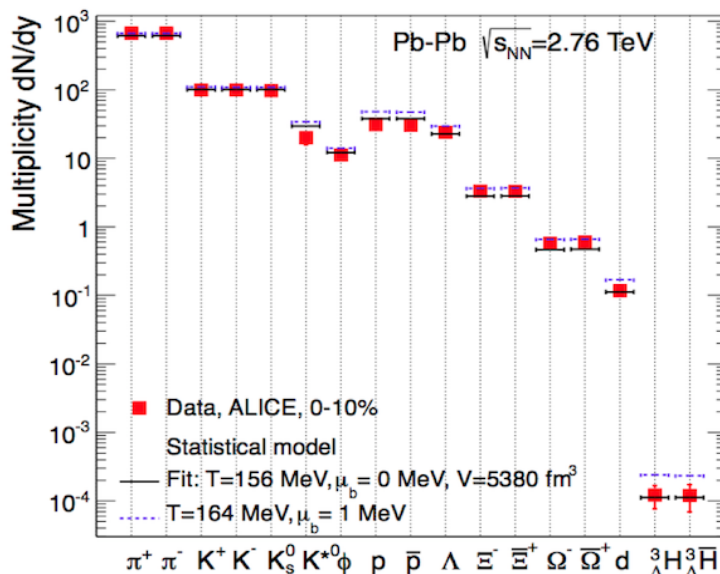


Figure 1.4: (Color Online) Fit of the hadron yields measured in ALICE with statistical hadronization model [37]. The K^{*0} is not included in fit.

obtained from the statistical model fits is consistent with unity, providing a strong argument in favour of the system, which is created in central collisions at RHIC, being in chemical equilibrium.

The Fig. 1.4 describes the comparison of hadron yields measured in central Pb-Pb collisions at $\sqrt{s_{NN}} = 2.76$ TeV with statistical thermal model.

Measurements of particle transverse momentum distributions provide information on the properties of the system at thermal or kinetic freeze-out when all elastic collisions have ceased. The idea of a common collective outward expansion velocity β_T of particles in the system is consistent with the observations that the $\langle p_T \rangle$ of heavier particles is larger than for lighter particles (i.e. for the same outward velocity, more massive particles will have a larger momentum) and that $\langle p_T \rangle$ increases as a function of centrality [31, 36]. The particle p_T spectra can be fitted with a Blast-Wave function [39] inspired from hydrodynamic models. The Fig. 1.5 shows T_{kin} vs β_T extracted by the simultaneous fit to the pion, kaon and proton spectra in ALICE from Pb-Pb collisions at

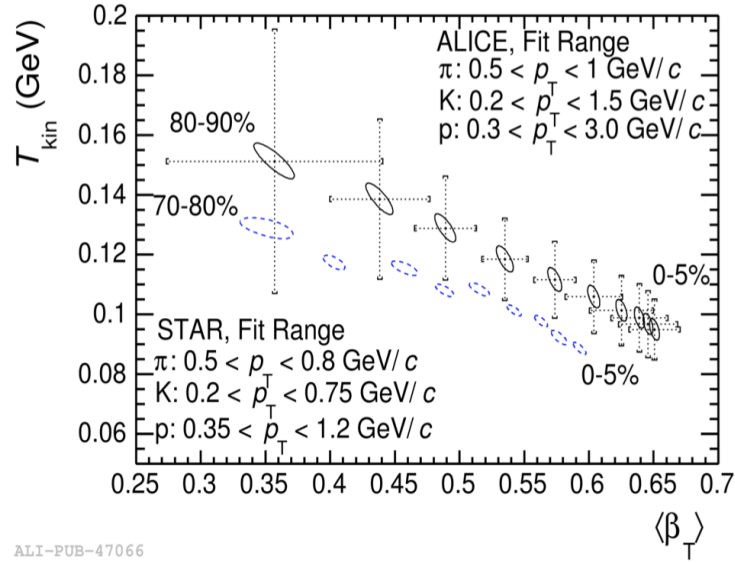


Figure 1.5: T_{kin} vs. β_T extracted by a simultaneous fit to the pion, kaon and proton spectra, measured in ALICE and STAR experiment, to a Blast Wave function. [37, 38]

$\sqrt{s_{NN}} = 2.76$ TeV [37] and in STAR from Au-Au collisions at $\sqrt{s_{NN}} = 200$ GeV [38]. This shows that the system created in central collisions expands faster than peripheral collisions and freezes out at lower temperature.

1.5.2 Nuclear Modification Factor

Hadron spectra in AA collisions can be a tool for the study of properties of the dense medium created in the collisions and particle production mechanisms in different p_T ranges. The effects of the medium on particle production can be studied by comparing particle spectra from central AA collisions to the spectra from pp collisions. The nuclear modification factor R_{AA} , for a given particle, is the ratio of the p_T distribution of the particle in AA collisions (for a given centrality) scaled by the number of binary collisions, N_{bin} , appropriate for the centrality, divided by the p_T spectrum of the corresponding particle in pp collisions:

$$R_{AA}(p_T) = \frac{1}{T_{AA}} \frac{d^2 N^{AA} / dp_T d\eta}{d^2 \sigma^{NN} / dp_T d\eta}, \quad (1.2)$$

1 Introduction

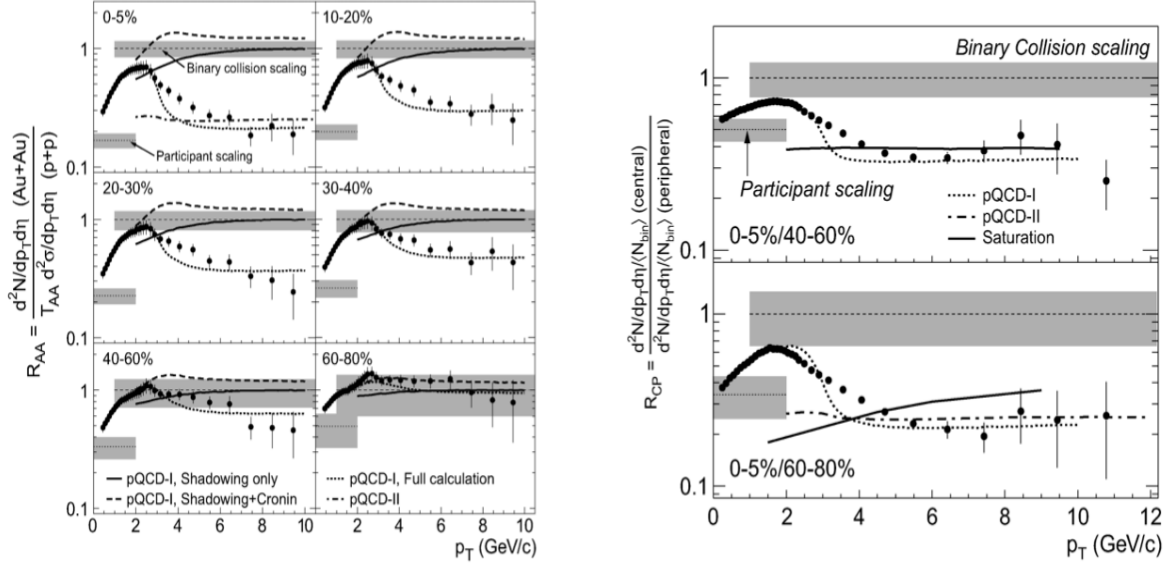


Figure 1.6: The left plot shows R_{AA} and right plot shows R_{CP} for charged hadrons for different centralities measured by STAR collaboration for Au-Au collisions at $\sqrt{s_{NN}} = 200$ GeV. The shaded bands indicate the systematic uncertainty related to the number of participant and number of binary collision scaling calculations. [42]

where $T_{AA} = \langle N_{bin} \rangle / \sigma_{inel}^{NN}$ is average nuclear thickness function, $\langle N_{bin} \rangle$ is the average number of binary NN collisions calculated using MC Glauber simulations and σ_{inel}^{NN} is the inelastic pp cross-section. Respecting R_{AA} , comparison can be made of the yields in central AA collisions to those in peripheral collisions to quantify the differences between the systems created in collisions with different centralities:

$$R_{CP}(p_T) = \frac{d^2 N^{AA} / dp_T d\eta|_{central}}{d^2 N^{AA} / dp_T d\eta|_{peripheral}} \frac{\langle N_{bin} \rangle|_{peripheral}}{\langle N_{bin} \rangle|_{central}} \quad (1.3)$$

R_{AA} and R_{CP} should be equal to unity if particle production in AA collisions scale with the number of binary collisions. However, for intermediate to high p_T , there is a suppression of particle production in central to mid-central AA collisions when compared to pp collisions and in central AA collisions when

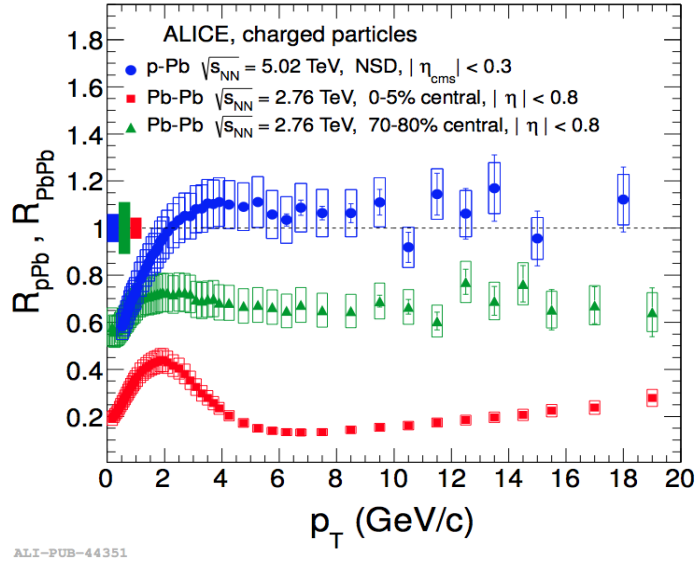


Figure 1.7: (Color Online) Nuclear modification factor in Pb-Pb at $\sqrt{s_{NN}} = 2.76$ TeV and p-Pb collisions at $\sqrt{s_{NN}} = 5.02$ TeV.[43, 44]

compared to peripheral AA collisions [31, 36, 40, 41].

The STAR experimental results are shown in Fig.1.6 [42]. Fig.1.7 shows a comparison of R_{PbPb} of charged hadrons in different centralities in Pb-Pb collisions at $\sqrt{s_{NN}} = 2.76$ TeV [43], and also the figure shows R_{pPb} in p-Pb collisions at $\sqrt{s_{NN}} = 5.02$ TeV [44] which is close to unit above $p_T > 2$ GeV/c. R_{PbPb} in Pb-Pb collisions emphasizes the observation are due to final state effects and due to formation of a hot and dense medium in the collisions.

1.5.3 Strangeness Enhancement

A long standing prediction for a signature of QGP formation is the enhancement of strange hadrons. The production channels for $s\bar{s}$ pair formation in the QGP is high because of high gluon density, gluon fusion and annihilation of light quark pairs than pp interactions where QGP is not expected to be formed. The production of strange hadrons relative to nonstrange hadrons is suppressed in hadronic reactions when one go from SPS [45] to RHIC [46] to LHC [47]

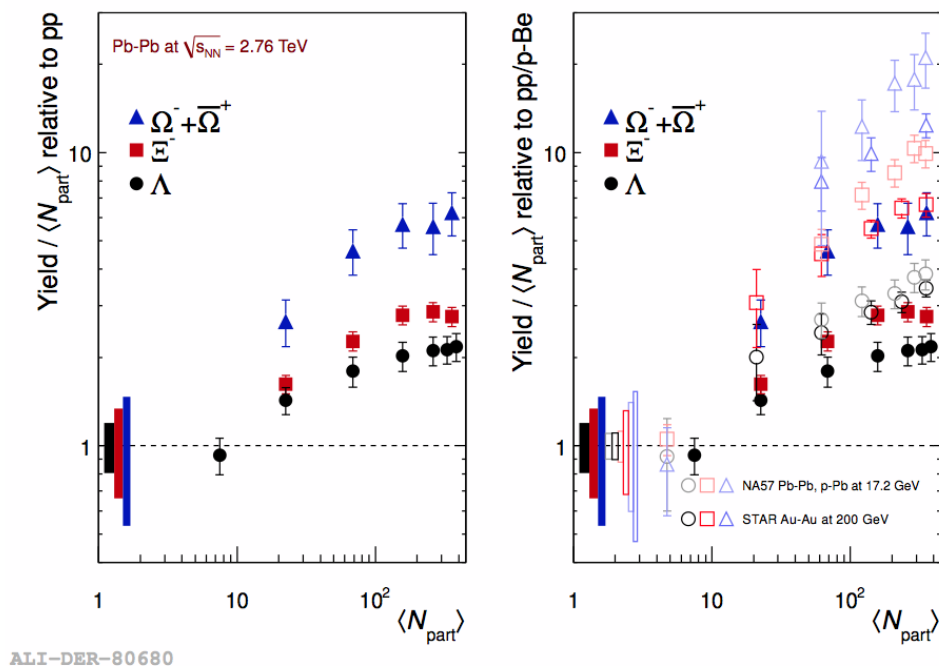


Figure 1.8: (Color Online) Strangeness enhancement for multi-strange hadrons measured in SPS[45] (on right plot shown by faint open markers), RHIC[46] (on right plot shown by dark open markers) and LHC [47] energies (on both plots shown by solid markers). Blue, red and black markers are for Ω , Ξ and Λ , respectively.

energies and this happens for all the multi-strange species.

The Fig. 1.8 shows the strangeness enhancement plot for multi-strange hadrons in Pb–Pb collisions at $\sqrt{s_{NN}} = 2.76$ TeV measured in ALICE and it is compared with the results from lower energy experiments.

1.5.4 Anisotropic Flow

Due to asymmetry in the overlap region, looks like an almond shape, during non-central heavy ion collisions, the interactions among constituents of the system generate a pressure gradient which is larger along the short axis than along the long axis of the almond-shaped collision region. Therefore, the initial spatial anisotropy causes the nuclear matter to also have a momentum anisotropy. Consequently, the azimuthal distribution of produced particles carry the information about the pressure of the nuclear matter produced in the

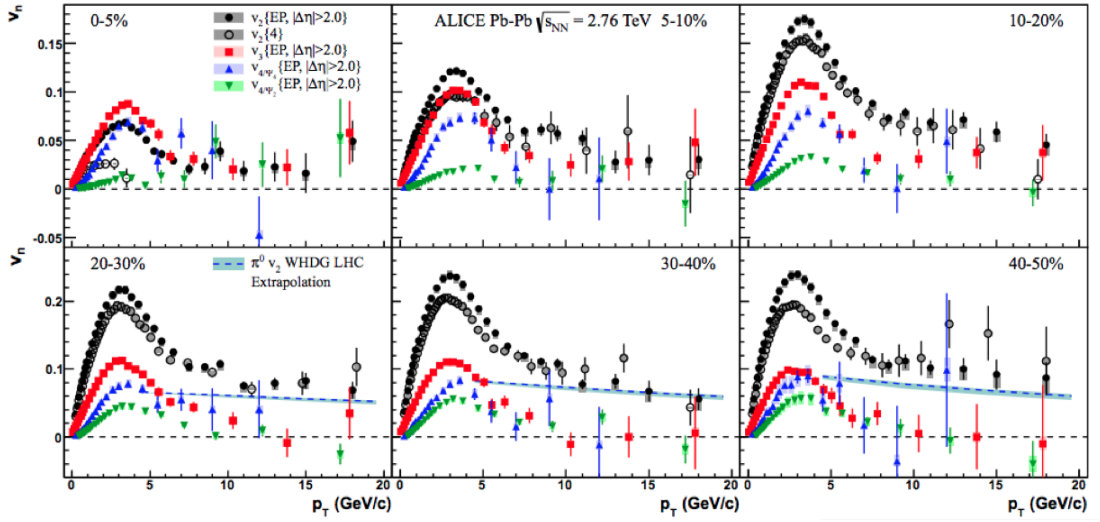


Figure 1.9: (Color Online) v_2 , v_3 and v_4 coefficients measured for charged particles as a function of p_T for various centrality classes [50]. The dashed line represents the WHDG model calculations for neutral pions v_2 [51] extrapolated to the LHC collision energy. For clarity, the markers for v_3 and v_4/ψ_2 results are slightly shifted along the horizontal axis. Error bars (shaded boxes) represent the statistical (systematic) uncertainties.

early stage of the heavy ion collisions [48]. The azimuthal distribution of produced particles can be expanded in terms of Fourier series [49];

$$\frac{dN}{d\phi} \propto 1 + \sum_{n=1}^{\infty} v_n \cos[n(\phi - \psi_n)] \quad (1.4)$$

where ϕ is the azimuthal angle of the particle, ψ_n is the reaction plane angle and v_n is the n^{th} harmonic coefficient. The first harmonic coefficient, v_1 , is called the directed flow and the second harmonic coefficient, v_2 , is called the elliptic flow. The elliptic flow magnitude was measured in RHIC, where v_2 reaches a value compatible with the one predicted by hydrodynamics for a “perfect fluid”, that is a fluid without internal friction and vanishing shear viscosity [52]. At LHC, the elliptic flow has been studied by ALICE [53] as a function of centrality and found to reach its maximum between 30% and 50% centrality, where the asymmetry of the collision is more enhanced. In comparison to RHIC, the integrated v_2 of charged particles increases by about 30%,

indicating that the hot and dense matter created at LHC still behaves like a fluid with almost zero viscosity. Besides v_2 , ALICE has measured triangular, v_3 , and quadrangular, v_4 , azimuthal anisotropic flow with respect to both second and fourth order event planes, v_{4/ψ_2} and v_{4/ψ_4} [53, 54]

1.5.5 Heavy Flavour

Heavy quarks are produced in the early stage of the AA collisions. Thus, heavy quarks experience the full evolution of the system and can be studied to investigate the properties of the medium. In particular, they are expected to lose energy interacting with the constituents of the medium, while their multiplicity is not expected to change. The energy lost by a particle in the medium (ΔE) depends on the characteristics of the particle traversing it (energy, mass and colour charge) and provides fundamental information on the plasma properties, like the gluon density, particle-medium interaction coupling, temperature and thickness. Through the measurement of charm and beauty meson production at low and high momentum, it is also possible to investigate whether the hadronization mechanism happens in the medium or via fragmentation in the vacuum, respectively. Hadronization via recombination in the medium would occur if a quark and an antiquark (or three quarks) are close themselves in the phase space combine together to form a meson (or a baryon). In this case the momentum of the hadron is equal to the sum of the momenta of the original quarks [55]. Instead, in case of hadronization via fragmentation of a high-momentum parton in the vacuum, the hadron carries a fraction of the original momentum of the parton. A possible hadronization via recombination of the charm quark with the partons in the medium would affect the D_s^+ meson production: the medium created in heavy-ion collisions presents an enhanced multiplicity of strange quarks [56], and if c quarks recombine in the medium,

an enhancement of D_s^+/D with respect to pp collisions is expected [57, 58]. Recombination can also be responsible of an enhanced charmed baryon (e.g. λ_c^+) production relative to D mesons.

1.6 Resonance Production and In-Medium Effects

Strongly decaying particles have life-times (τ) about 10^{-23} s (about the time a light signal takes to cross a proton) and such particles are called resonances [59]. Resonances' decay lengths are in the scale of few fermi. Their widths (Γ) and life-times obey the uncertainty principle $\Gamma \times \tau = \hbar c$. A typical resonance is the $\Lambda(1520)$ baryon resonance (commonly known as Λ^*) which has a life-time of 12.6 fm/c and width of 15.7 MeV/c² [60]. Some resonances are excited states of corresponding stable particles, like Λ^* is the excited state of $\Lambda(1115)$.

1.6.1 History on Resonances

In 1960, Luis W. Alvarez, et al, announced the discovery of the first resonance $\Sigma^*(1385)$ at the Rochester High Energy Physics Conference. In $K^- + p \rightarrow \Lambda + \pi^+ + \pi^-$ experiments, they had shown that the π^\pm recoiled against a combination of $\Lambda + \pi^\pm$ had a unique mass and broadened by the effects of the uncertainty principle. The mass of the $\Lambda\pi$ combination was calculable as 1385 MeV and the isospin as 1. In the same year the $K^*(890)$ and $\Lambda(1405)$ were discovered. Soon after that, the ρ , ω and η vector meson resonances were discovered. In 1962, the $\Xi^*(1530)$ resonance was discovered and reported. By the year 1967, around 1411 resonances had been discovered [61]. Now-a-days, relativistic heavy ion collisions experiments use resonances as tool to study various properties of the hot and dense nuclear matter under extreme conditions. The table 1.1 reports most of the resonances [62] people are measuring

and/or have measured in AA , pp and pA collisions.

Resonances	Decay Channel	Branching Ratio	Width (MeV/c ²)	Decay Length (fm)
$\rho^0(770)$	$\pi^+\pi^-$	$\sim 100\%$	149.1	1.3
$K^{*0}(892)$	$K\pi$	$\sim 100\%$	47.4	4.2
$f_0(980)$	$\pi^+\pi^-$	dominant	40-100	2-5
$\phi(1020)$	K^+K^-	48.9%	4.266	46
$\Delta(1232)$	$p\pi$	$>99\%$	~ 120	~ 1.6
$\Sigma^{*0}(1385)$	$\Lambda\pi$	87%	36	5.5
$\Lambda(1520)$	pK	22.5%	15.7	12.7
$\Xi^{*0}(1530)$	$\Xi\pi$	$\sim 100\%$	9.1	22

Table 1.1: List of resonances with their hadronic (dominant) decay channel, branching ratio, decay width and decay length. [62]

1.6.2 Resonance In-Medium Effects

Resonances with extremely short life-times can decay inside the medium before all the in-medium effects cease. Thus by measuring resonance production, one can access information about how the resonances encounter the hot-dense medium. In the case of the ρ resonance, it can scatter with a π in the medium to temporarily form a resonance state. After the resonance state decays back to a ρ and a π , the ρ properties might have been modified by this t-channel interactions. It was predicted that in the hot-dense medium, a downward mass shift for the ρ and K^* resonance and a upward mass shift for the Δ resonance can be expected [63]. Thus a systematic measurement of various types of resonances, such as $\rho(770)$, $K^*(892)$, $\Delta(1232)$, etc., and their properties in the hot-dense matter, such as masses, widths and line shapes in relativistic heavy ion collisions is needed to study the hadrons' in-medium effects.

1.6.3 Re-scattering Effect and Re-generation Effect

The resonances can be produced during hadronization of the evolving fireball produced in heavy-ion collisions. Their short lifetimes make it possible for

the resonances' decayed daughters to undergo a period of re-interaction in the hadron gas phase [64, 65, 66, 67]. A fraction of the resonances may decay before the kinetic freeze-out stage and their hadronic decay daughter particles might be re-scattered by other particles in the hadron gas. This is called the resonance daughter particles' re-scattering effect. This leads to loss of the resonance yields. Further the hadrons in the medium can scatter pseudo-elastically and re-generate some resonances in the medium. This is called the re-generation effect, and this effect can increase the resonance yield. The schematic diagram of these process are shown in the Fig. 1.10.

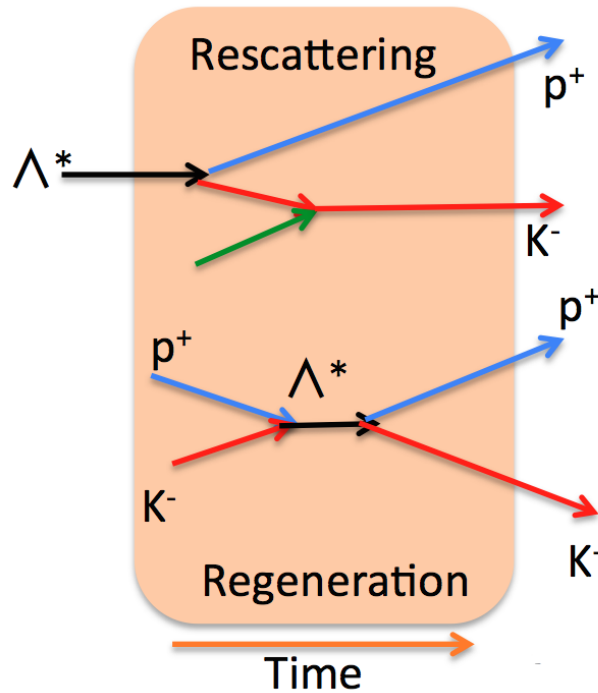


Figure 1.10: (Color Online) Schematic diagram of re-scattering and re-generation of resonances (here Λ^*) during hadronic scattering medium in heavy ion collision.

The fraction of the resonance yields destroyed by its daughter particles' re-scattering effect depends on the resonance life-time, its daughter particle's interaction cross sections with the hadrons in the medium, the time scale between the chemical and kinetic freeze-outs and the density of the medium. The

amount of the resonance signals which can be produced by the re-generation effect depends on the interaction cross sections for hadrons to produce the resonance, the time scale allowed for this re-generation effect and the medium density. Due the resonance daughter particles' re-scattering effect and the re-generation effect, resonances are useful tools to probe the fireball evolution properties between chemical and kinetic freeze-outs, and the time scale between the two freeze-outs [64, 68, 69, 70, 71].

1.7 Heavy-Flavour Production in p-Pb Collisions

For hard processes, such as heavy-flavour production, in the absence of nuclear and medium effects, a proton-nucleus, pA , collision would behave as a superposition of independent nucleon-nucleon (NN) collisions. The charm and beauty differential yields would then scale from pp to pA proportionally to the average number collisions ($\langle N_{coll} \rangle$) of inelastic NN collisions (binary scaling):

$$\frac{d^2 N_{pA}^{HQ}}{dp_T dy} = \langle N_{coll} \rangle \times \frac{d^2 N_{pp}^{HQ}}{dp_T dy} \quad (1.5)$$

Initial-state effects, such as the modification of the parton distribution functions in the nucleus, can determine a deviation from binary scaling. Partons can also suffer initial state radiation or experience momentum broadening due to multiple soft scattering before the hard process. These effects are addressed by comparing the charm production in p-Pb to that in pp collisions.

1.7.1 Initial-State Effects and the Role of p-A Collisions

The colliding nuclei behave as a mere incoherent superposition of their constituent nucleons. In the initial state, the nuclear environment affects the quark and gluon distribution, which are modified in bound nucleons depending on

the partons fractional momentum x and the atomic mass number A . The bound nucleon PDFs $f_i^A(x, Q^2)$ for each parton flavour “i” are usually expressed by

$$f_i^A(x, Q^2) \equiv R_i^A(x, Q^2) f_i^N(x, Q^2), \quad (1.6)$$

where $R_i^A(x, Q^2)$ denotes the nuclear modification to the free nucleon PDF $f_i^N(x, Q^2)$. Experiments of deep inelastic scattering (DIS) with nuclei have measured overall nuclear effect on the quark structure function in full x region [72, 73] is shown in Fig. 1.11. The figure illustrates different effects; shadow-

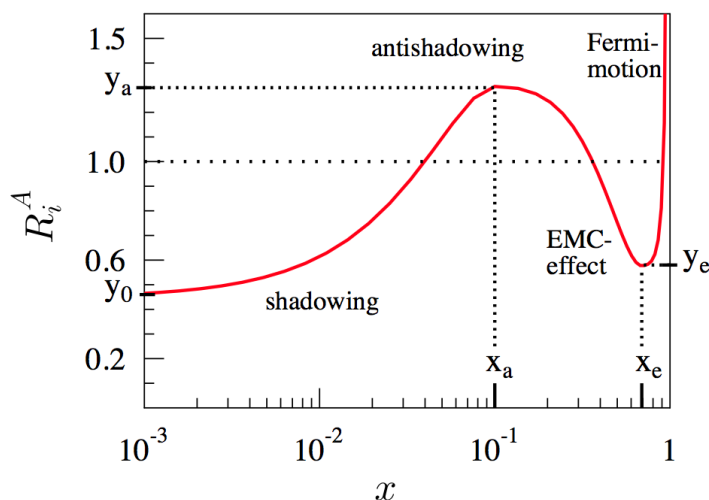


Figure 1.11: Schematic diagram of the nuclear modification of bound nucleons.[72, 73]

ing in the small x region ($x < 0.05$), anti-shadowing in the moderate values of x ($0.05 < x < 0.3$), EMC effect in the region $0.3 < x < 0.7$ and Fermi motion when $x \rightarrow 1$. A direct consequence of shadowing is the reduction of hard-scattering cross sections in the phase-space region characterised by small x incoming partons, hence, at mid-rapidity, low- p_T outgoing partons. The measurement of the nuclear modification factor of the D meson p_T distribution in p-Pb collisions at the LHC energy is a sensitive tool to probe nuclear PDFs. Partons can also lose energy in the initial stages of the collision via initial state radiation, thus modifying the centre-of-mass energy of the partonic system, or

experience transverse momentum broadening due to multiple soft collisions before the $c\bar{c}$ pair is produced. This effect is known as Cronin effect and it was first observed in 1987 [74].

1.8 Phase Transition in Compact Stars

1.8.1 Compact Stars

Compact stars, i.e. white dwarfs and neutron stars, are the final stages in the evolution of ordinary stars. After hydrogen and helium burning, the helium reservoir in the star's core is burned up to carbon and oxygen. The nuclear processes in the core will stop and the star's temperature will decrease. Consequently, the star shrinks and the pressure in the core increases. As long as the star's mass is above a certain value, it will be able to initialise new fusion processes to heavier elements. The smaller the mass, the more the core has to be contracted to produce the required heat for the next burning process to start. If the star's initial mass is below eight solar masses, the gravitational pressure is too weak to reach the required density and temperature to initialize carbon fusion. Due to the high core temperature, the outer regions of the star swell and are blown away by stellar winds. What remains is a compact core mainly composed of carbon and oxygen. The interior consists of a degenerate electron gas which is responsible for the intrinsic high pressure. The compact remnant starts to emit its thermal energy and a white dwarf is born. As there are no fusion processes taking place in the interior of the white dwarf, electron degeneracy force, other than thermal pressure, is needed to keep the star in hydrostatic equilibrium.

If the initial mass of an ordinary star exceeds eight solar masses, carbon and

oxygen burning starts in the core. As long as they produce the required temperature to keep the star in hydrostatic equilibrium, new burning processes to heavier elements will take place in the core while the fusion of lighter elements will continue in the outer shells. Once iron is produced in the core, there is no burning process left to generate energy as the fusion to heavier elements requires energy to be put in. So the mass of the iron core increases while its radius decreases as there is less thermal pressure to work against gravity. At some critical mass, the iron core collapses. The density increases so much that the electrons are captured by nuclei and combine with protons to form neutrons. Therefore, the atomic nuclei become more and more neutron-rich with increasing density. At some critical density, the nuclei are not able to bind all the neutrons anymore, neutrons start to drop out and form a neutron liquid which surrounds the atomic nuclei. For even larger density, there will be just a dense and incompressible core of neutrons with a small fraction of electrons and protons. Neutrons in neutron stars are then degenerate like electrons in white dwarfs. The radii of neutron stars are typically 10 km.

1.8.2 Phase Transition in Compact Stars

The heavy ion experiments at RHIC, LHC and FAIR are designed to study strongly interacting matter under extreme conditions of high temperature and/or high baryon density. These experiments are also expected to shed light on the properties of a new phase of strongly interacting matter, the Quark Gluon Plasma (QGP) and on the nature of the deconfinement phase transition. On the other hand, compact stars, due to their large central densities, serve as a natural laboratory to study the properties of the strongly interacting matter at high densities and small temperature, in particular, the possibility of a deconfining phase transition and this phase transition is shown in Fig. 1.2.

A compact star is build up of cold and dense matter, classified in the following. If it is composed of nuclear matter or deconfined quark matter it is called a neutron star or quark star, respectively. Furthermore it may simultaneously be composed of both confined and deconfined quarks, in which case it is a hybrid star. As we expect the density in the interior to be larger than at the surface, a hybrid star consists of a quark core and a nuclear mantle.

1.9 About the Thesis

The chapter 1 and chapter 2 are the introduction of the thesis and about the ALICE detector system, respectively. The thesis includes the study on $\Lambda(1520)$ in pp and p-Pb collisions at $\sqrt{s_{NN}} = 7$ TeV and 5.02 TeV, respectively. The main objective of the study is to see any hadronic scattering medium effect on $\Lambda(1520)$ resonance production in p-Pb collisions at $\sqrt{s_{NN}} = 5.02$ TeV. Also the thesis give the measurement of yield and mean transverse momentum of the resonance in the said collision systems at the LHC energies. This part is covered by chapter 3. The thesis also contains a comparative study on cold nuclear matter effect in p-Pb collisions at $\sqrt{s_{NN}} = 5.02$ TeV using four simulation models. Our aim is to see how the cold matter effect is implemented in models and how they are able explain the published result of ALICE. For this, we have studied the cold nuclear matter effect on D mesons. We have also measured the p_T -differential cross-section of D mesons in pp and p-Pb collisions at $\sqrt{s_{NN}} = 7$ TeV and 5.02 TeV, respectively, from different models and compared with the published results from ALICE. Chapter 4 covers this study. On the above part we have studied a system where we are not expecting formation of any QGP. Complementing the above part, we also have studied the phase transition in astronomical objects. There we have calculate the different

mode of frequencies in neutron stars, quark stars and hybrid stars. Our aim is to show how the frequencies behaves in the presence of phase transition and what is the effect of magnetic field on equation of state of different compact stars. Chapter 5 describes about this study. Finally, conclusion of the thesis is given in chapter 6.

2 A Large Ion Collider Experiment at the LHC

A Large Ion Collider Experiment (ALICE) has been collecting data from November 2009. In the first phase of data taking, Large Hadron Collider (LHC) successfully ran pp collisions at $\sqrt{s} = 0.9, 2.76, 7$ and 8 TeV, Pb-Pb collisions at $\sqrt{s_{NN}} = 2.76$ TeV and 5.02 TeV, and finally p-Pb collisions at $\sqrt{s_{NN}} = 5.02$ TeV and 8 TeV. In phase 2, LHC is producing pp collisions at $\sqrt{s} = 13$ TeV and Pb-Pb collisions at $\sqrt{s_{NN}} = 5$ TeV. ALICE has been designed and optimized to study the high particle-multiplicity environment of ultra-relativistic heavy-ion collisions.

2.1 The Large Hadron Collider

The Large Hadron Collider [75, 76, 77] is a two concentric superconducting rings hadron accelerator and collider installed in the 27 km tunnel. The CERN accelerator complex combines LHC together with the Proton Synchrotron (PS)[78] and Super Proton Synchrotron (SPS)[19], among the others shown in fig. 2.1. Four main experiments, namely, ATLAS[79] (A Toroidal LHC ApparatuS), CMS[80] (Compact Muon Solenoid), ALICE[122] (A Large Ion Collider Experiment) and LHCb[82] (LHC Beauty). ATLAS and CMS, the bigger ones,

2 A Large Ion Collider Experiment at the LHC

are multi-purpose detectors built to discover the Higgs boson and hints of new physics beyond the Standard Model. LHCb is dedicated to the physics of the flavour, focusing on the study CP-violation using B meson decay channels. ALICE is dedicated to the physics of Quark Gluon Plasma through the observation of high-energy heavy-ion collisions.

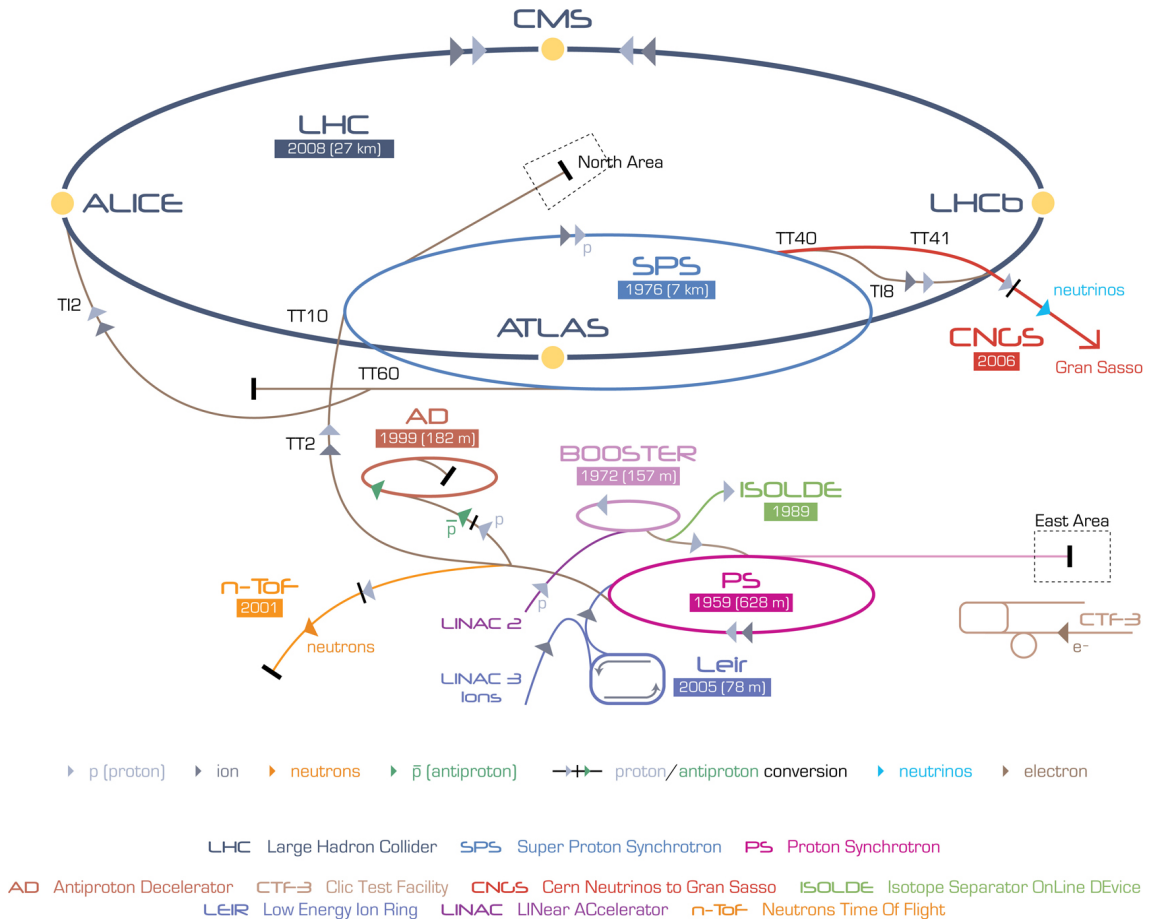


Figure 2.1: (Color online) CERN accelerator complex at the LHC [83]

The LHC was initially designed to provide pp collisions at the energy of $\sqrt{s} = 14$ TeV and Pb-Pb collisions at $\sqrt{s_{NN}} = 5.5$ TeV. However, after the technical incident of 2008 [84] due to the quenching of a magnet in 2010 and 2011 [85], the LHC ran for pp collisions at $\sqrt{s} = 7$ TeV and Pb-Pb collisions at $\sqrt{s_{NN}} = 2.76$ TeV. Later in 2012 it has increased its energy, so that it has produced pp collisions at $\sqrt{s} = 8$ TeV and p-Pb collisions at $\sqrt{s_{NN}} = 5.02$ TeV. After

two years of maintenance and upgrading, in May 2015, it again started with a significant increased energy of 13 TeV pp collisions

Besides energy, one most important accelerator parameter is the instantaneous (often the peak value within a fill) luminosity, L , which is the proportionality factor between the event rate R and the interaction cross-section of the process under study (σ_{int}):

$$R = L\sigma_{int} \quad (2.1)$$

The instantaneous luminosity depends only on the colliding beam parameters at the interaction point and can be determined as

$$L = \frac{N_b^2 n_b f \gamma}{4\pi \varepsilon_n \beta^*} F \quad (2.2)$$

where N_b is the number of particles per bunch, n_b is the number of bunches per beam, f is the revolution frequency, γ is the relativistic gamma factor, ε_n is the normalized transverse beam emittance, β^* is the amplitude function at the interaction point (IP), F is the geometrical reduction factor that accounts for the crossing angle at the IP. It is worthy to remind that the transverse emittance and the amplitude function are related to the bunch cross-sectional size (σ_L) by the relation:

$$\sigma_L^2 = \frac{1}{\pi} \beta \varepsilon \quad (2.3)$$

The transverse emittance gives how successful is the process of “packing” protons into bunches during the injector chain. A low emittance particle beam shows that the particles are confined to a small distance and have nearly the same momentum. This is important to keep the particle beam confined in their orbit all along the beam transport and accelerating chain. The β function is determined precisely by the quadrupole focusing strength of magnetic

configuration. If the amplitude is small, the beam is squeezed. The value of the amplitude function at the interaction point, referred to as β^* , is the most significant. In order to achieve higher luminosity, it is important to keep the emittance low and β^* small, depending on the capability of the beam-focusing hardware near the interaction point. Moreover, in order to have β^* small at the interaction point, β is kept at larger values along the orbit. Since the emittance depends on the beam momentum during the acceleration, the normalised emittance, $\varepsilon_n = \gamma\beta\varepsilon$, which does not vary during the acceleration is most commonly considered, as in equation 2.2. If the particles in each bunch are assumed to be distributed in the three spatial directions according to Gaussian distributions; in transverse direction the standard deviation of a bunch is σ_{xy} , and σ_z is the standard deviation in longitudinal direction w.r.t. beam pipe, then the F factor can be obtained from the total crossing angle at the IP, θ_c , as

$$F = \left[1 + \left(\frac{\theta_c \sigma_z^2}{2\sigma_{xy}^*} \right)^2 \right]^{-1/2}. \quad (2.4)$$

The maximum number of particles per bunch is limited to $N_b = 1.15 \times 10^{11}$. The number of bunches per beam may vary according to the definition of different filling schemes during the machine operations. The beam parameters, ε and β^* in particular, have been optimized in order to tune the luminosity in different interaction points depending on capability of the installed experiments at those points. ATLAS and CMS are the two highest luminosity experiments, which can run at a peak luminosity of the order of $L \sim 10^{33} \text{cm}^{-2}\text{s}^{-1}$ while LHCb can run at the design luminosity value of $L \sim 10^{32} \text{cm}^{-2}\text{s}^{-1}$. In order to avoid pile-up in the main tracker detector, the maximum luminosity sustainable by ALICE in pp collisions is limited to the value $L \sim 10^{30} \text{cm}^{-2}\text{s}^{-1}$.

The proton source is a simple bottle of hydrogen gas. An electric field is

used to strip hydrogen nuclei from their electrons to yield protons. The Linear Accelerator 2 (Linac2) is the first accelerator in the chain where the protons get accelerated to the energy of 50 MeV. The beam is then injected into the Proton Synchrotron Booster (PSB), which accelerates the protons to 1.4 GeV. Here a multiple splitting technique is used to generate the bunch trains. Then the Proton Synchrotron (PS) pushes the beam to 25 GeV. Protons are then sent to the Super Proton Synchrotron (SPS) where they are accelerated to 450 GeV and then they are injected at the threshold energy into the LHC. The protons are finally transferred to the two beam pipes of the LHC. After the injection of all bunches from the SPS to the LHC is completed, the energy ramp up procedure starts and accelerates the beams to the desired energy level. The beam in one pipe circulates clockwise while the beam in the other pipe circulates anticlockwise. It takes 4 minutes and 20 seconds to fill each LHC ring, and 20 minutes for the protons to reach the energy of 4 TeV. The LHC RF cavities operate at 40 MHz. In the ultimate LHC filling pattern, each of the available bunch slots is split in 10 buckets, each of them being 2.5 ns long. But only one out of 10 is filled with a bunch, so the minimum bunch separation is 25 ns. In the injection scheme there can be maximum 2808 number of bunches that can be arranged in the 3564 available 25 ns slots of the LHC. However, the empty buckets can in fact contain small amount of particles, which are called “satellite” or “ghost” bunches. Protons are not the only particles accelerated in the LHC. The first collisions between stable beams of lead took place on the November 2010 [86]. Lead ions for the LHC start from a source of heated (500⁰C) lead cylinder. The vaporised and partially ionised lead atoms enter Linac 3 in order to be completely stripped off the remaining electrons. Lead ions (82⁺⁸²) are then collected and accelerated in the Low Energy Ion Ring (LEIR). After that they follow the same route to maximum energy as the

protons. The nominal luminosity of lead ion beam is $L \sim 10^{27} \text{ cm}^{-2} \text{ s}^{-1}$.

2.1.1 ALICE at the LHC

ALICE [87, 88], located at Point 2 on the LHC, is designed as a general purpose heavy-ion detector with the goal of enabling a deeper understanding of the strong QCD sector of the Standard Model. It surveys the extreme states of matter created in heavy-ion collisions. A main purpose of heavy-ion experiments is the extraction of the physics, originating from the quark gluon plasma phase and from the follow-up phases of a hot hadronic gas. For that purpose, dedicated detectors with well developed particle identification (PID) capabilities and very precise low p_T tracking are needed. The ALICE detector is, therefore, designed to measure charged-particle densities up to $dN/dy \approx 8000$. The schematic diagram of the detector is shown in the Fig. 2.2. ALICE has measured proton-proton collisions to study QCD in the absence of a strongly interacting medium. These measurements provide a baseline for heavy-ion collisions. In this context, an even more important baseline is given by the study of proton-lead collision system. This system should provide insights into cold nuclear matter effects, without a phase transition to the QGP. Hence, it will help to disentangle hot and cold medium effects in heavy-ion collisions.

2.2 The ALICE Detector

The ALICE setup can be divided into two independent groups of detectors. The first set is located inside the central barrel, enclosed in the L3 solenoid magnet which provides a 0.5 Tesla magnetic field. The central barrel detectors include the Inner Tracking System (ITS), the Time Projection Chamber

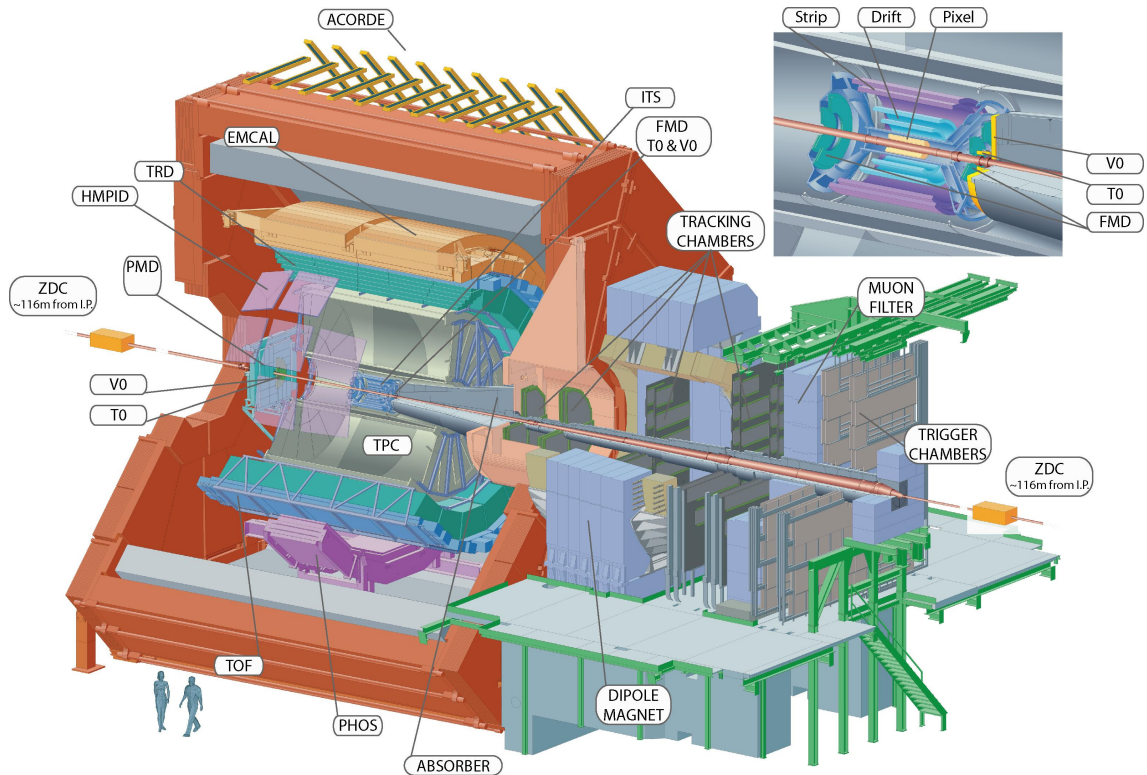


Figure 2.2: (Color online) Schematic diagram of the ALICE detector. [87]

(TPC), the Transition Radiation Detector (TRD), the Time Of Flight (TOF), the High Momentum Particle Identification Detector (HMPID), the Electro-Magnetic Calorimeter (EMCal) and the PHOTon Spectrometer (PHOS). Other small angle detectors are the Zero-Degree Calorimeters (ZDC), the Photon Multiplicity Detector (PMD), Forward Multiplicity Detector (FMD), the T0 and the V0 detectors. The forward muon arm consists of a complex arrangement of absorbers, a large dipole magnet (with field 0.67 T) and fourteen planes of tracking and triggering chambers. An array of scintillators called Alice COsmic Ray DETector (ACORDE) is located on top of the ALICE solenoid magnet. A summary of all the sub-detectors is given in Table 2.1.

2 A Large Ion Collider Experiment at the LHC

Detectors	Position (m)	Acceptance	Acceptance	technology	purpose
SPD (layer 1, 2)	0.039, 0.076	$\pm 2, \pm 1.4$	full	Si Pixel	tracking, vertex
SDD (layer 3, 4)	0.15, 0.239	$\pm 0.9, \pm 0.9$	full	Si drift	tracking, PID
SSD (layer 5, 6)	0.38, 0.43	$\pm 0.97, \pm 0.97$	full	Si strip	tracking, PID
TPC	0.848, 2.466	± 0.9 ($r=2.8\text{m}$) ± 1.5 ($r=1.4\text{m}$)	full	Ne drift, MWPC	tracking, PID
TRD	2.90, 3.68	± 0.84	full	TR, Xe drift, MWPC	tracking, e^\pm id
TOF	3.78	± 0.9	full	MRPC	PID
HMPID	5.0	± 0.6	$1.2^0 - 58.8^0$	C_6F_{14} , RICH, MWPC	PID
PHOS	4.6	± 0.12	$220^0 - 320^0$	PbWO_4	photons
EMCAL	4.36	± 0.7	$80^0 - 187^0$	Pb, scint	photons, jets
ACORDE	8.5	± 1.3	$-60^0 - 60^0$	scintillator	cosmics
MCH	-14.22, -5.36	$-4.0 < \eta < -2.5$	full	MWPC	muon tracking
MTR	-17.12, -16.12	$-4.0 < \eta < -2.5$	full	RPC	muon trigger
ZDC:ZN	± 116	$\eta < 8.8$	full	W+quartz	forward neutrons
ZDC:ZP	± 116	$6.5 < \eta < 7.5$	$-9.7^0 - 9.7^0$	brass, quartz	forward protons
ZDC:ZEM	7.25	$4.8 < \eta < 5.7$	$-16^0 - 16^0$ & $164^0 - 196^0$	Pb, quartz	photons
PMD	3.64	$2.3 < \eta < 3.9$	full	Pb+PC	photons
FMD disc 1	inner: 3.2	$3.62 < \eta < 5.03$	full		
FMD disc 2	inner: 0.834	$1.7 < \eta < 3.68$	full		
	outer: 0.752		full	Si strip	charged particle
FMD disc 3	inner: -0.628	$-3.4 < \eta < -1.7$	full		
	outer: -0.752		full		
VZERO-A	3.4	$2.8 < \eta < 5.1$	full	scint.	time, vertex
VZERO-C	-0.897	$-3.7 < \eta < -1.7$	full		
T0A	3.75	$4.61 < \eta < 4.92$	full	quartz	time, vertex
T0C	-0.727	$-3.28 < \eta < -2.97$	full		

Table 2.1: Summary of the ALICE detector subsystems. The position is the approximate distance from the interaction point to the face of the detector and corresponds to the radius for barrel detectors (inner and outer radius for the TPC and TRD) or the position along the beam (z coordinate) for the others. [89, 90]

2.2.1 The Inner Tracking System

The ITS [103] provides precise information of primary vertex with a resolution better than $100 \mu\text{m}$ and reconstruct the secondary vertices from the decays of hyperons and D and B mesons. Also it could identify particles with momentum below $200 \text{ MeV}/c$ with resolution 10-12%. This improves the momentum and angle resolution for particles reconstructed by the TPC and to reconstruct particles traversing dead regions of the TPC. It surrounds the beam pipe and has six cylindrical layers of high resolution position sensitive silicon based detectors and are located at radii between 3.9 and 43 cm. Starting from the beam

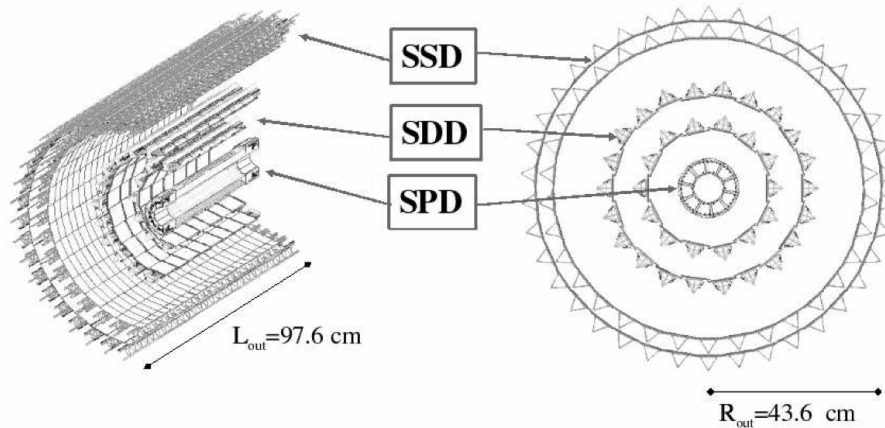


Figure 2.3: Layout of ITS detector

pipe radially outwards it consist of two Silicon Pixel Detectors (SPD), two Silicon Drift Detectors (SDD) and two Silicon Strip Detectors (SSD) as shown in Fig. 2.3. Because of the high particle density expected in heavy-ion collisions at LHC (as many as 50 particles per cm^2 have been predicted for the inner layer) and in order to achieve the required impact parameter resolution, SPD have been chosen for the innermost two layers, and SDD for the following two layers. The four outer layers have analogue readout and therefore can be used for particle identification via dE/dx measurement in the non-relativistic ($1/\beta^2$) region. So the ITS stand-alone is featured as a low- p_T particle spectrometer.

It covers the rapidity range of $|\eta| < 0.9$ for all vertices located within the length of the interaction diamond ($\pm 1\sigma$, i.e. ± 5.3 cm along the beam direction). The momentum and impact parameter (i.e. the distance of closest approach of a track to the primary interaction vertex) resolution for low-momentum particles are dominated by multiple scattering effects in the material of the detector; therefore the amount of material in the active volume has been kept to a minimum, an average of 7.7% of radiation length for tracks crossing the ITS perpendicularly to the detector surfaces ($\eta = 0$).

2.2.2 The Time Projection Chamber

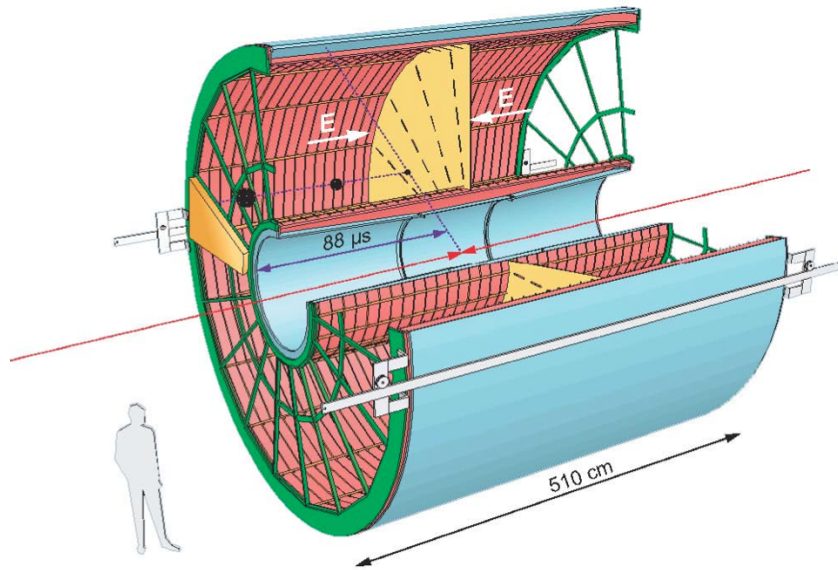


Figure 2.4: Conceptual view of the TPC, showing the dimensions and components. [92]

TPC [92] is the main tracking detector in the central barrel of the ALICE experiment at the LHC. Its function is to provide track finding (efficiency larger than 90%), charged particle momentum measurement (resolution better than 2.5% for electrons with momentum of about 4 GeV/c), particle identification (dE/dx resolution better than 10%), vertex determination and two-track separation (resolution of few MeV/c) in the region $p_T < 10$ GeV/c and pseudorapidity $|\eta| < 0.9$. The TPC, shown in figure 2.4, is cylindrical in shape and 5 m in length with an inner radius of 85 cm and an outer radius of 247 cm. The resolution on dE/dx is lower than 10%. The detector is made of a large field cage, weighing about 8 tonnes and filled with 90m³ of Ne, CO₂ and N₂. The voltage gradient in the TPC is ~ 400 V/cm, with a high voltage of 100 kV at the central electrode at $z = 0$. The two read-out planes are at $z = \pm 2.5$ m. After ionisation, electrons are transported from either side of the central electrode to the end plates, where there are readout pads. For signal readout Multi Wire Proportional Chambers (MWPC) at the end plates are used. Each of the two end

plates has 36 readout chambers arranged in 18 sectors. Each sector contains an Inner Readout Chamber (IROC) and an Outer Readout Chamber (OROC). When a charged particle traverse through the gas of TPC, it ionizes the gas and produces primary electrons. These electrons drift along the electric field. Since the magnetic field is oriented parallel to the electric field (along z direction), the drifting electrons are not influenced by it. At the end of drift path, the electrons are amplified by an avalanche process around the anode wires. By collecting the information of originating time of charged track and the times when readout pads get signal, the 3-dimensional space points are constructed in the TPC volume. Then tracks can be reconstructed in TPC and the transverse momenta can be obtained from the curvature of the tracks. The TPC can reconstruct a primary track of momentum 100 MeV/c up to 100 GeV/c. The particle identification is performed by the simultaneous measurement of the specific energy loss, charge and momentum of each particle that traverse through the detector. The energy loss in TPC is described by the parameterized Bethe-Bloch formula which is given by;

$$f(\beta\gamma) = \frac{P_1}{\beta^{P_4}} \left(P_2 - \beta^{P_4} - \ln \left(P_3 + \frac{1}{(\beta\gamma)^{P_5}} \right) \right), \quad (2.5)$$

where P_i are the fit parameters extracted for each data taking period, β is the particle velocity, γ is the Lorentz factor.

The energy loss dE/dx vs momentum in Pb-Pb collisions at $\sqrt{s_{NN}}=2.76$ TeV measured in TPC is shown in figure 2.5. The energy loss bands for each particle species are fitted with the function 2.5. Below 1 GeV/c or even less, each particle species have their respective distinguished bands. So each track can be identified track by track in this momentum region. But at higher momenta particles can be separated on a statistical basis via multi-gaussian fits

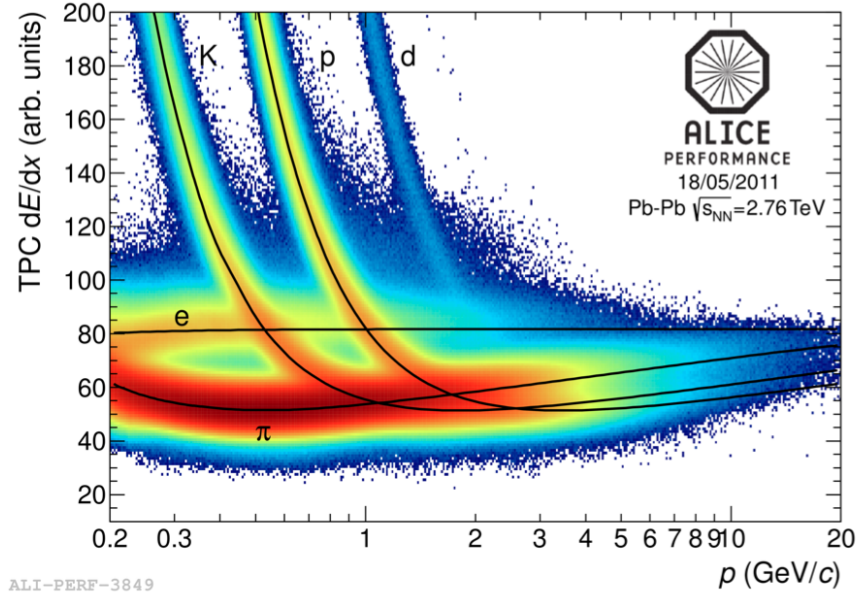


Figure 2.5: (Color online) The measured energy loss dE/dx vs momentum using TPC in Pb-Pb collisions at $\sqrt{s_{NN}} = 2.76$ TeV.

to the difference between the dE/dx measured and dE/dx expected (value from fitting). Resolution cut is applied to identify particles which is given by,

$$N\sigma_{TPC} = \frac{dE/dx_{measured} - dE/dx_{expected}}{\sigma_{TPC}^{PID}}, \quad (2.6)$$

where $dE/dx_{measured}$ is the energy loss of the tracks measured in TPC, $dE/dx_{expected}$ is the expected energy loss of the tracks taken from the function fit. σ_{TPC}^{PID} is the PID resolution of the TPC; 5.2% in pp collisions and 6.5% in central Pb-Pb collisions.

2.2.3 The Transition Radiation Detector

The TRD [93] is dedicated to the electron identification for $p_T > 1$ GeV/c. It consists of a radiator and Multi Wire Proportional Chamber (MWPC) placed around the TPC at radial distance of 2.9 to 3.68 m over the full azimuthal angle and $|\eta| < 0.84$. When relativistic charged particles cross the interface of two media of different dielectric constant, transition radiation is emitted, with

photons in the KeV range of 1 to 30 keV. Since the transition radiation photons are in the keV range they are detected by the gaseous detector. To optimize the absorption of X-rays a gas mixture of Xe/CO₂ (85/15) is used. The pion being heavier do not emit radiation below certain momentum. So the TRD can extend the pion rejection capability of the TPC up to very high momentum. The electron identification is crucial for the study of electrons p_T spectrum and light and heavy vector meson resonances through their leptonic channel decay.

2.2.4 The Time Of Flight

The TOF detector is dedicated to charged particle identification in the pseudo-rapidity region $\eta < 0.9$. It is a gas based Multi-gap Resistive Plate Chamber (MRPC) and placed around the TRD at a radial distance of 2.70 to 3.99 m. The TOF has an ability to detect particles with 99.9% efficiency and a time resolution about 85 ps in Pb-Pb collisions and 120 ps in pp collisions. For particle identification it measures the particle's time of flight and takes the momentum information from TPC. Resolution cut is applied to identify particles which is given by,

$$N\sigma_{TOF} = \frac{Time_{measured} - Time_{expected}}{\sigma_{TOF}^{PID}}, \quad (2.7)$$

where measured time is the flight time of the particle measured by an algorithm of TOF and T0 detector, expected time is the flight time computed during the central tracking procedure, and σ_{TOF}^{PID} is the PID resolution of the TOF detector. The TOF can provide more than 2σ π/K separation up to momentum 3 GeV/c and 3σ K/p separation up to 4 GeV/c in Pb-Pb collisions at $\sqrt{s_{NN}} = 2.76$ TeV.

2.2.5 V0 and T0

The VZERO (V0) [94] detectors are the plastic scintillator detectors located asymmetrically on both sides of the interaction point. It covers the full azimuth within $2.8 < \eta < 5.1$ (V0A) and $-3.7 < \eta < -1.7$ (V0C). The V0A and V0C is at a distance of 3.4 m and 0.9 m from the IP on the opposite side, respectively. The time resolution is about 1 ns. It is mainly used for triggering and rejection of beam gas events through its timing information. It is also used for the determination of centrality in Pb-Pb collisions.

The T0 detector consists of two arrays (T0A and T0C) of Cherenkov counters. Like the V0, T0A is placed at 375 cm from the IP on the opposite side respect to the muon spectrometer, while T0C is located just in front of the absorber, at 727 cm from the IP. The eta coverage for T0A and T0C are, respectively, $4.61 < \eta < 5.92$ and $-3.28 < \eta < -2.97$. The Time Zero's main purpose is that of generating a start time for the TOF detector. This time corresponds to the real time of the collision. The T0 is used also for the online monitoring of the luminosity and to generate an early “wake-up” signal for the TRD, prior to the L0 trigger.

2.2.6 Zero Degree Calorimeter

The purpose of ZDC [95] is to estimate the centrality of the collisions by detecting the spectator nucleons that keep their trajectory in the forward direction along the beam pipe. So ZDCs are placed at 116 m on either side of the interaction point, very close to the beam pipe. The ZDCs are also used to estimate the reaction plane in nucleus collisions and to reject parasitic collisions (when fragments collide with the main bunch displaced about 30 cm from the centre of the experiment). Each ZDC is made of two calorimeters; one for the

spectator neutrons (ZN), is placed between the beam pipes and other for the spectator protons (ZP), is located externally to the outgoing beam pipe where positive particles are deflected and separated by the neutrons by the magnets in the LHC beam pipe.

2.2.7 The Muon spectrometer

The Forward Muon Spectrometer [96] has been designed to identify heavy-flavour vector mesons (J/Ψ , Υ , Υ' , etc.) at forward rapidity, through their leptonic decay to $\pm\mu$ pairs. The detector is located externally to the central barrel and covers the pseudo-rapidity region $-4.0 < \eta < -2.5$. A 3.5m long carbon conic-shaped absorber has been placed in front of the spectrometer, still inside the L3 magnet, to screen the detector from most of the primary and secondary particles produced in the interaction point. The trigger system (Muon Trigger, MTRG) is given by four planes of Resistive Plane Chambers (RPC) operating in streamer mode. The MTRG is placed after a 1.2 m thick iron filter-wall, that allow only muons with $p > 4 \text{ GeV}/c$ to reach the trigger chambers. An inner beam shield protects the spectrometer from secondaries produced at large rapidity.

2.2.8 The Photon Multiplicity Detector

The PMD [97, 98] is installed to measure the multiplicity of photons produced in pp and Pb-Pb collisions in the forward rapidity. It can also be used for the determination of reaction plane. It is located at a distance of 3.67 m from the interaction point in the A side of the ALICE and it covers a pseudo-rapidity $2.3 < \eta < 3.9$ with full azimuth. The PMD consists of two planes (charged particle veto and pre-shower) separated by a $3X_0$ thick converter (1.5 cm Pb and 0.5 cm Stainless Steel). The physics goal of the PMD are as follows:

2 A Large Ion Collider Experiment at the LHC

1. Measurement of global observables like multiplicity, pseudo-rapidity distributions are useful in understanding particle production mechanism. PMD can extend our understanding of particle production in forward rapidities.
2. Measurement of azimuthal anisotropy and flow of photons can be used to probe the thermalization of the medium formed in heavy-ion collisions.
3. Signals of chiral-symmetry restoration (e.g. disoriented chiral condensate) can be studied through the measurement of $N_\gamma/N_{charged}$ in a common phase space.

2.2.9 ALICE COsmic Ray DEtector

The ACORDE [88] is an array of plastic scintillator counters placed on top of the ALICE magnet. It triggers cosmic muons to align and calibrate central barrel tracking detectors and detects single and multiple muon events, which allow the study of high energy cosmic rays with 90% efficiency. Atmospheric muons need at least 17 GeV of energy to reach the detector underground, and the TPC can track and measure the momentum of muons up to 2 TeV, defining a wide range of energy in which the ALICE detector can measure cosmic rays with the use of the ACORDE triggering.

2.3 ALICE Online and Trigger

2.3.1 DAQ

The ALICE Data Acquisition system (DAQ) [99, 100] controls and manages the flow of data from the ALICE detector to the permanent storage during LHC collisions. After the CTP has issued a positive trigger decision to the detectors, the data is sent by the DAQ system via many hundreds of optical data cables to a computer farm known as Local Data Concentrators (LDC). The LDCs

assemble the data into the sub-events and then passed onto one of 40 Global Data Collectors (GDCs) to merge them into a whole event. This event is stored by DAQ in one of 20 Global Data Storage servers temporarily, before being archived to the tape at CERN where it becomes available for off-line analysis.

2.3.2 CPT

The ALICE Central Trigger Processor (CTP) [99, 100] is a low level hardware trigger. It consists of 24 Local Trigger Units (LTU) for each detector system. It receives and processes trigger signal from trigger detectors like SPD, TRD, TOF, PHOS, EMCAL, T0, V0, MTR, etc. The first level trigger is the L0 (delivered after $1.2 \mu s$), the second level is L1 (delivered after $6.5 \mu s$), and the final trigger is L2 (delivered after $100 \mu s$). After final trigger a event is stored. The output of the CTP goes to the LTUs of each detector and then to the front end electronics of the detector. The CTP forms 50 independent trigger classes combining 24 L0 inputs, 24 L1 inputs and 12 L2 inputs.

2.3.3 HLT

The High Level Trigger (HLT) [100] performs to refine the event data collected by the DAQ (which can reach at a rate of 25 Giga Byte/s) retaining the physics informations. For this, it first collects the detector information in parallel with the DAQ LDC. Its computer farm performs an on-line reconstruction and analysis to decide if the event is worth of keeping. Then, it can read out only part of the detector in which there is interesting information. Finally, it compresses the data by over an order of magnitude before it is sent to the DAQ to be stored at CERN.

3 Measurement of $\Lambda(1520)$ resonance production in pp and p-Pb collisions

3.1 Introduction

The measurements of resonance productions in ultra-relativistic heavy-ion collisions provide information on the properties of the hadronic medium formed and different stages of its evolution. The measurements of the short-lived resonances allow us to estimate the time span of the hadronic phase between the chemical and the kinetic freeze-out. Their measurements in pp and p-Pb collisions can be baseline for the measurements in heavy ion collisions and can provide data for tuning event generators inspired by Quantum Chromodynamics. This chapter discusses the results of Λ^* resonance production in pp collisions at $\sqrt{s} = 7$ TeV and in p-Pb collisions at $\sqrt{s_{NN}} = 5.02$ TeV.

3.2 Data sample and event selection

Data produced in 2010 has been used for the analysis on pp collisions and the corresponding period is LHC10d. Similarly, for p-Pb collisions, the analysis has used data produced in 2013 and the corresponding periods are LHC13b and LHC13c. The pp analysis has been done over 120 Millions events, where as

3 Measurement of $\Lambda(1520)$ resonance production in pp and p-Pb collisions

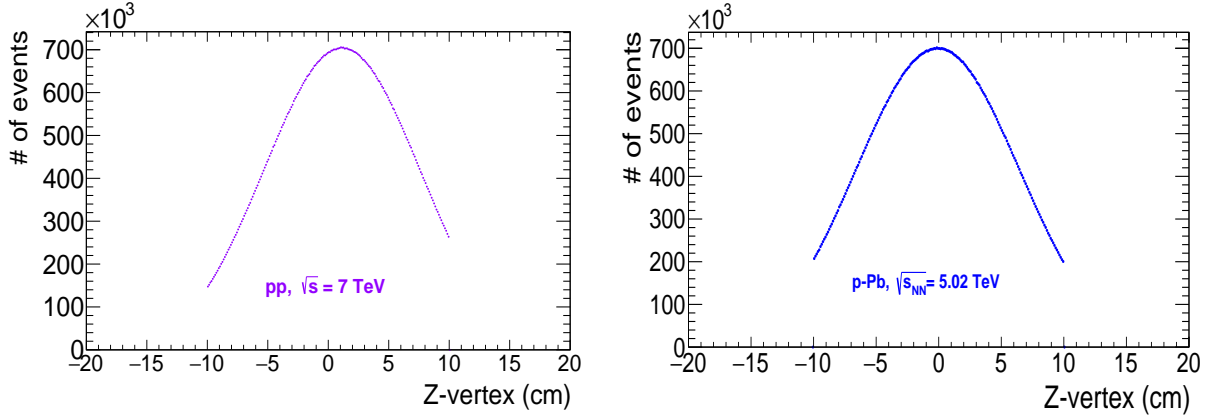


Figure 3.1: (Color online) The Z- position of vertex in pp (left) and in p-Pb (right) collisions.

100 Millions events has been analysed in p-Pb collisions. The minimum bias events for pp collisions are selected for the analysis which require interaction trigger with a single hit either in the SPD detector or in any one of the VZERO detectors [101]. The non-single diffractive (NSD) events for p-Pb collisions require V0AND trigger which is an offline V0 selection [101]. The primary collision vertices are reconstructed using either the hits in SPD or by using the tracks of TPC and ITS. The distance of primary collision vertex position from the center of laboratory frame along laboratory Z-axis is calculated and in the analysis, the Z-position of vertex is selected to be between ± 10 cm from the center of laboratory frame to ensure uniform detector acceptance in the central pseudorapidity region, $|\eta| < 0.8$. The events with Z-position of vertex far from the interaction point will cause a loss in the acceptance. The Z-position of vertex distribution in p-Pb and pp collisions are shown in Fig. 3.1. The centrality/multiplicity classes have been selected through the standard framework, where centrality/multiplicity is expressed in terms of percentiles of the raw multiplicity estimators. For these analyses, VZERO scintillator measured amplitude on the Pb direction (V0A) has been chosen as estimator. The accepted events are binned in four multiplicity intervals, according to the following: 0-20%, 20-40%, 40-60%, 60-100%. The events, which are coming

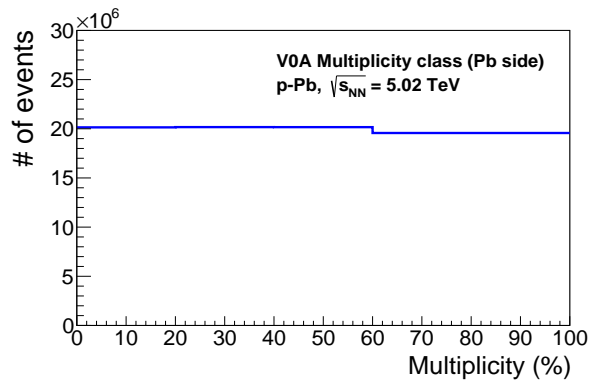


Figure 3.2: (Color online) Multiplicity distribution in % of the accepted events in the range 0-100%..

in 0-20% multiplicity bins are those 20% triggered events having higher measured amplitude in V0A compared to rest 80% events. The multiplicity distribution of the accepted events in the range 0-100% is shown in the Fig. 3.2.

3.3 Track Selection

The Λ^* is studied by reconstructing its invariant mass from its hadronic decay charged particles $p^\pm K^\pm$ having branching ratio 22.5% [62]. The production is studied in the rapidity region $-0.5 < y < 0.5$ for pp collisions and in the rapidity region $-0.5 < y < 0$ for p-Pb collision in the center of mass frame. Due to asymmetry in the p-Pb collisions, the shift in rapidity of center of mass frame towards the proton beam direction is 0.465 with respect to lab frame. The analysis combines both Λ^* and $\bar{\Lambda}^*$ and in the text it is denoted by Λ^* . The global tracking is done using the detectors ITS and TPC. The Kalman filter algorithm [102, 103] is applied for track fitting ($\chi^2/ndf \leq 4$). A refit is performed with the reconstructed tracks where the tracks are refitted inwards from the outermost layers of TPC to the innermost layers of ITS and are prolonged to the

3 Measurement of $\Lambda(1520)$ resonance production in pp and p-Pb collisions

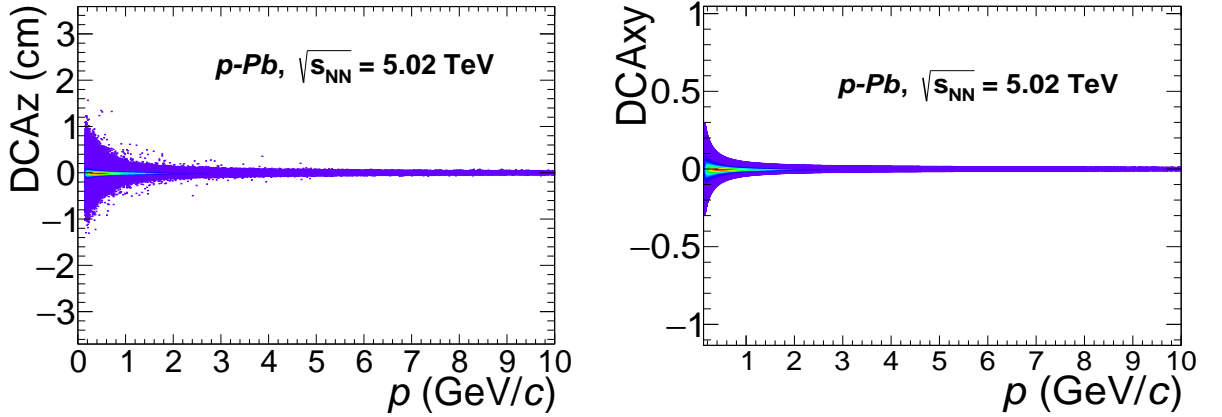


Figure 3.3: (Color online) The quality assurance plots for DCA cuts along z-axis (on left) and in xy-plane (right) are shown from in p-Pb collisions data.

reconstructed primary vertex and vice-versa. The tracks which passes successfully the refit of the reconstruction algorithm, from the outer layer of the detector to the primary vertex, through TPC and ITS are accepted in the analysis. Since the Λ^* has a very small lifetime, the decay daughters seem to originate near the interaction point. So they are selected from the primary tracks by applying a cut on distance of closest approach (DCA) to the primary vertex on the XY plane and along Z axis. The cut on the DCA_{XY} is implemented as a function of p_T . The default cut in pp collisions is $0.0182 + 0.035p_T^{1.01}$ cm and in p-Pb collision this is $0.0105 + 0.035p_T^{1.1}$ cm. The DCA component in the direction parallel to the beam has to be ≤ 2.0 cm. The quality assured plots for DCA cut are shown in Fig. 3.3. The above cuts on DCA reduces the contribution from the secondaries which may come from the weak decay of strange hadrons and interaction with the detector material. To maintain a reasonable momentum resolution a cut on transverse momentum $p_T > 0.15$ GeV/c is applied. In pp collisions the good quality tracks are selected by requiring a minimum 70 clusters inside TPC out of 159 possible, having fit with $\chi^2/ndf \leq 4$ and at least one hit in the inner sector of the SPD. For p-Pb collisions, a good quality track requires at least 70 crossed rows in TPC in stead of

cluster cut and the ratio of crossed rows over findable clusters should be ≥ 0.8 . The tracks with kinks ($K^\pm \rightarrow \mu^\pm + \nu_\mu$) are rejected through topological cut in the analysis. The pseudo-rapidity cut on each track is $\eta \leq 0.8$, which is well within the acceptance of TPC and TOF.

3.4 Particle identification with TPC and TOF

ALICE provides several methods to identify particles such as the measurement of the energy loss in the TPC detector and time-of-flight in TOF detector. So there is an expected value for energy loss and time-of-flight for a track for a certain momentum and mass. But in a detector one gets a distribution about the expected value. So one has to give some integral times the resolution (σ) cut to select a particular type of track. Suppose “ i ” indicates the detector used for PID ($i = \text{TPC, TOF}$) and “ j ” the particle species hypothesis (the term hypothesis is used because of uncertainty in choosing a specific particle species). So the $n\sigma$ cut can be defined as

$$n\sigma_{i,j} = \frac{X_{i,j} - X_{i,j}^{exp}}{\sigma_{i,j}^{PID}}, \quad (3.1)$$

where $X_{i,j}$ is a measured observable in the detector i , $X_{i,j}^{exp}$ is the predicted value of that observable in the mass hypothesis j and $\sigma_{i,j}^{PID}$ is the resolution on the measurement.

For analysis in pp collisions the pid cut is as follows: A 3σ pid cut on tracks (proton and kaon) has been applied while choosing tracks from TPC. While choosing proton and kaon tracks from TPC there is an upper bound on momentum as 1.1 GeV/ c and 0.6 GeV/ c , respectively, to avoid pK and K π band merging. This reduces significantly misidentification of the tracks and so the combinatorial background under the signal peak. Proton and kaon tracks above their threshold momentum have been chosen from TOF with a uniform 3σ pid

3 Measurement of $\Lambda(1520)$ resonance production in pp and p-Pb collisions

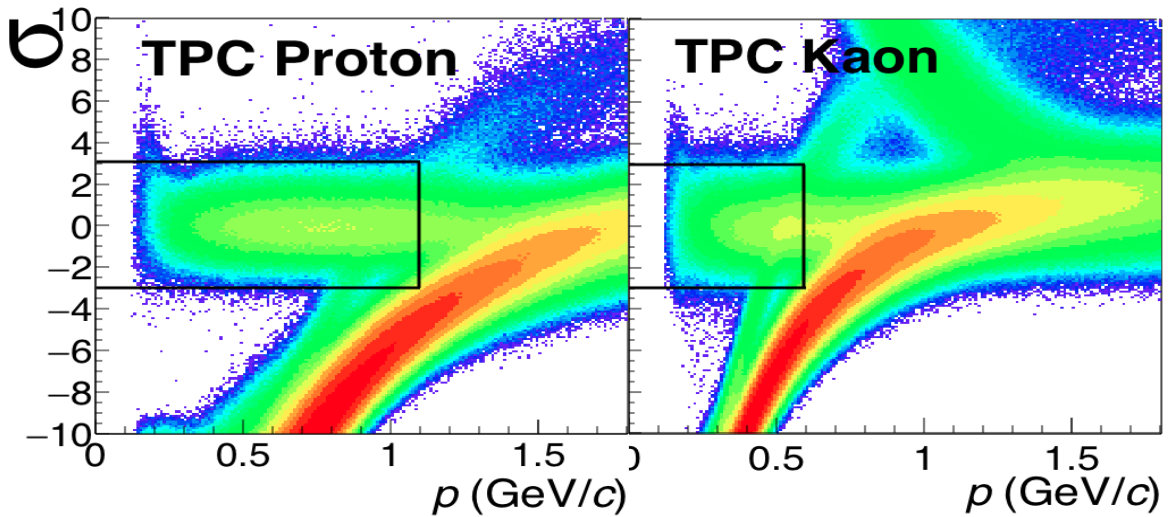


Figure 3.4: (Color online) $n\sigma$ of TPC tracks as proton on left and as kaon on right. The areas within the solid black lines are showing the region of PID selection from the TPC detector.

cut plus a 5σ cut on TPC as an veto. The σ distribution of TPC and TOF tracks as protons and kaons are shown in the Figs. 3.4 and 3.5. The rectangular areas covered by black lines are showing the areas within which protons and kaons are selected from different detectors.

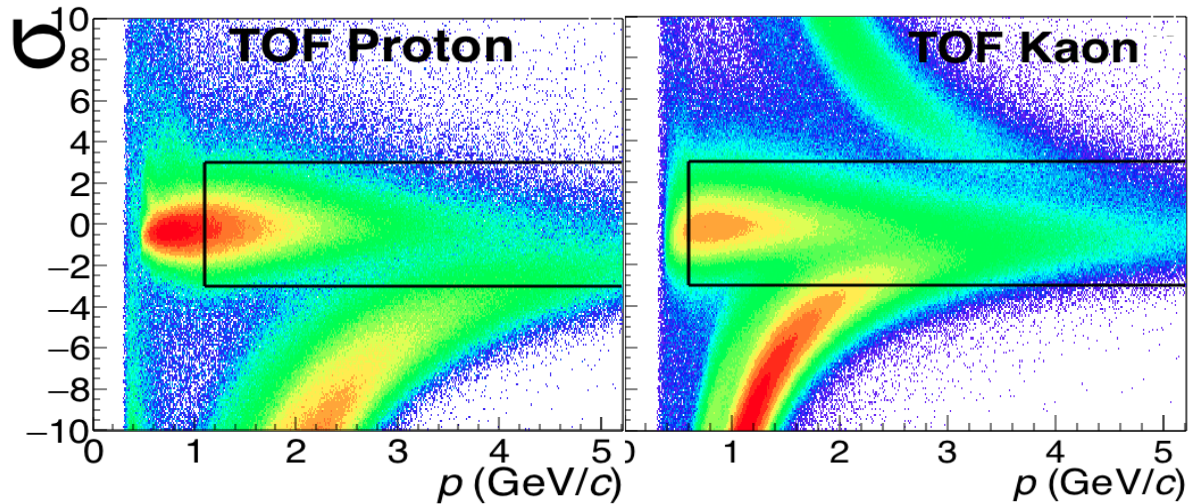


Figure 3.5: (Color online) $n\sigma$ of TOF tracks as proton on left and as kaon on right. The areas within the solid black lines are showing the region of PID selection from the TOF detector.

In case of p-Pb collision the PID cut strategy is little different. If a track is present in TOF, then a 3σ pid cut on TOF plus a 5σ cut on TPC has been

applied over all momentum region, But if a track is not present in TOF, then it has been chosen from TPC with a 3σ PID cut along with the same momentum restriction as given for the analysis in pp collisions.

3.5 Raw yield extraction

Invariant mass reconstruction is the only way in ALICE detector setup to extract the yield of a resonance. The invariant mass (M_{inv}) distribution is obtained from the combination of primary identified protons and kaons from the same events into unlike-sign pairs. This is given by the expression:

$$M_{pK} = \sqrt{(E_p + E_K)^2 - (\vec{p}_p + \vec{p}_K)^2}, \quad (3.2)$$

where E_p and E_K are the total energy of a proton and a kaon track with 3-momentum \vec{p}_p and \vec{p}_K , respectively. The distributions for p^+K^- and p^-K^+ are obtained separately and then summed bin by bin to obtain the total signal for pK. This summed distribution is indicated as US in the following sections. The US distribution in pp collisions is shown in the upper plot of the Fig. 3.6 by black solid markers. In order to extract the Λ^* signal it is necessary to remove or at least reduce the combinatorial background. This has been done with the mixed-event background (MEB) technique or like-sign background (LSB) technique. Here in MEB, invariant mass distribution is built by combining uncorrelated unlike-sign charged protons and kaons from different events. When applying this method, it is important to combine pairs from events with similar topology and multiplicity, to reproduce satisfactorily the kinematics properties of the combinatorial background. The events for the mixing have been selected by applying the ‘‘similarity’’ criteria listed below:

- difference in the z coordinate of the primary vertex position, $\Delta V_z < 1$ cm

3 Measurement of $\Lambda(1520)$ resonance production in pp and p-Pb collisions

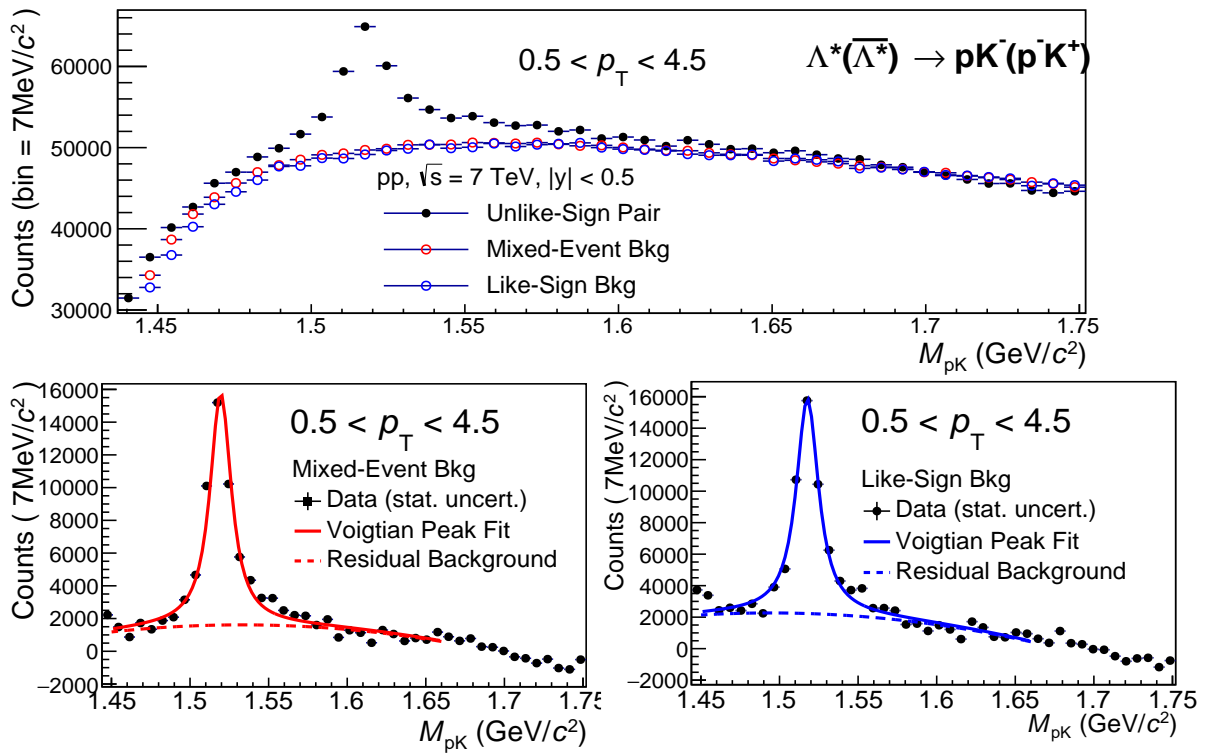


Figure 3.6: (Color online) In upper plot, the US distribution is shown by black solid markers, normalised MEB and LSB are shown by open red and open blue markers. In lower two plots it shows signal peaks after subtracting MEB (left) and LSB (right) by black solid markers. The solid red and blue lines show the Voigtian fits to the signal peaks and the dashed red and blue lines show the polynomial fits to the residual backgrounds, respectively. This is for pp collisions at $\sqrt{s} = 7$ TeV.

- difference in multiplicity, $\Delta M < 10$

A bunch of 10 events have been considered for mixing and the same criteria have been applied for the primary tracks selection and PID. The total mixed-event invariant mass distribution has to be normalised to the US distribution before subtraction, because the statistics of the mixed-event distribution is higher as consequence of mixing of tracks from 10 number of events. The normalisation range has been chosen far from the signal peak ($M_{inv} > 1.65$ GeV/c²). The normalised MEB is shown by open red circular markers in the upper plot of Fig. 3.6.

In LSB technique, the combinatorial background is constructed through the invariant mass of protons and kaons of same charge from same event. Since the number of positive and negative particles produced in relativistic heavy ion collisions are not same, the combinatorial background is constructed by taking the geometric mean of number of like sign pairs as shown in equation below.

$$N_{pK} = 2 \times \sqrt{N_{p^+K^+} \times N_{p^-K^-}}, \quad (3.3)$$

here $N_{p^+K^+}$ and $N_{p^-K^-}$ are the counts in the invariant mass spectra of p^+K^+ and p^-K^- , respectively. The LSB is shown by open blue circular markers in the upper plot of Fig. 3.6.

Even after the subtraction of combinatorial background, a certain amount of residual backgrounds remain under the Λ^* signal. This residual background may come from the following sources:

- correlated real pK pairs from particle decays
- effects of other correlations like elliptic flow.
- decayed from other particles but mis-identified as pK pairs.

3 Measurement of $\Lambda(1520)$ resonance production in pp and p-Pb collisions

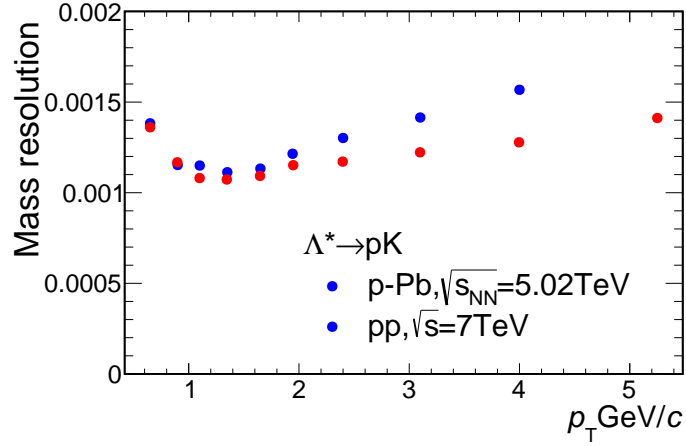


Figure 3.7: (Color online) The plot shows the mass resolution for Λ^* in pp (blue solid marker) and p-Pb (red solid marker) collisions in different p_T bins.

So after subtracting the combinatorial background, the peak has been fitted with a Voigtian function over a second order polynomial. This is shown in the lower two plots of the Fig. 3.6. The Voigtian function is a convolution form of Breit-Wigner and Gaussian functions. It is expressed as:

$$\frac{dN}{dm} = A \int \frac{\Gamma/2\pi}{(m - m') + \Gamma^2/4} \frac{e^{-(m' - m_0)^2/2\sigma^2}}{\sigma \sqrt{2\pi}} dm' \quad (3.4)$$

Where A , m_0 , Γ and σ are the fit parameters which represents the integral of the function (from 0 to ∞), mass peak position of the resonance, width of the resonance and the detector resolution.

The Gaussian function takes care the mass resolution of the signal coming due to the momentum resolution of the detectors. The mass resolution varies from 1 MeV to 1.6 MeV both in pp and p-Pb collisions and this is shown in Fig. 3.7. The Breit-Wigner function gives the raw yield, mass peak position and decay width of the signal and the polynomial rejects the residual background. The Λ^* signals with fitting in different p_T bins are shown in figures from 3.8 to 3.13.

3.5 Raw yield extraction

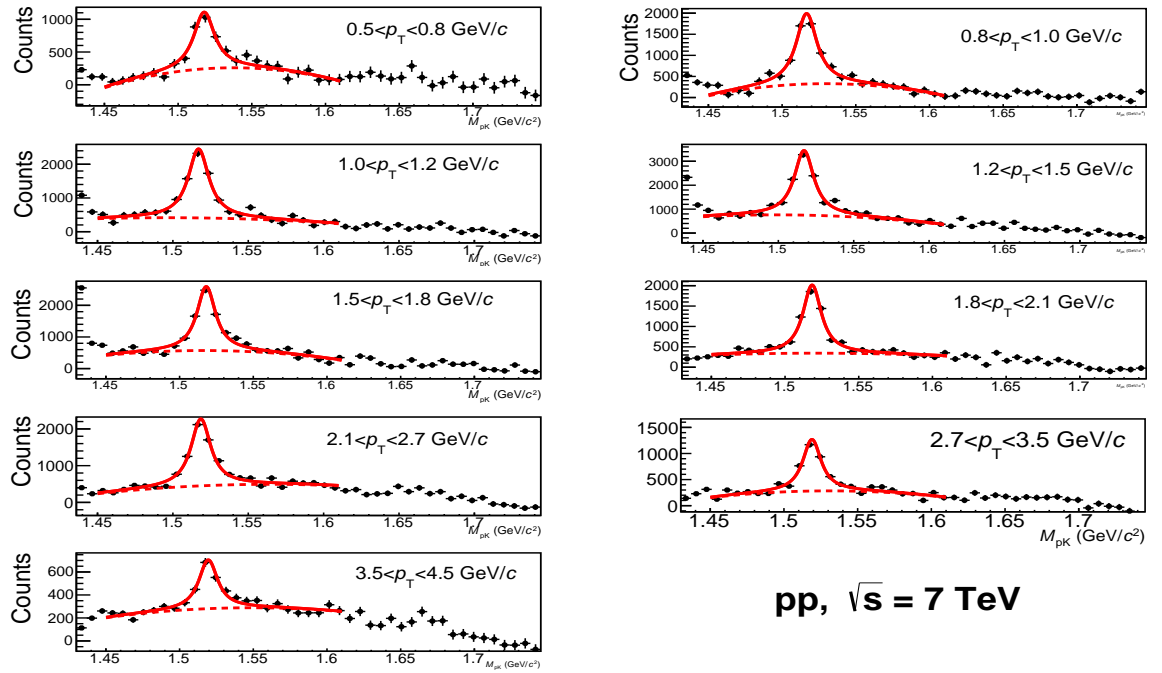


Figure 3.8: (Color online) These plots show Λ^* signal after subtracting MEB in different p_T bins in pp collisions at $\sqrt{s} = 7$ TeV.

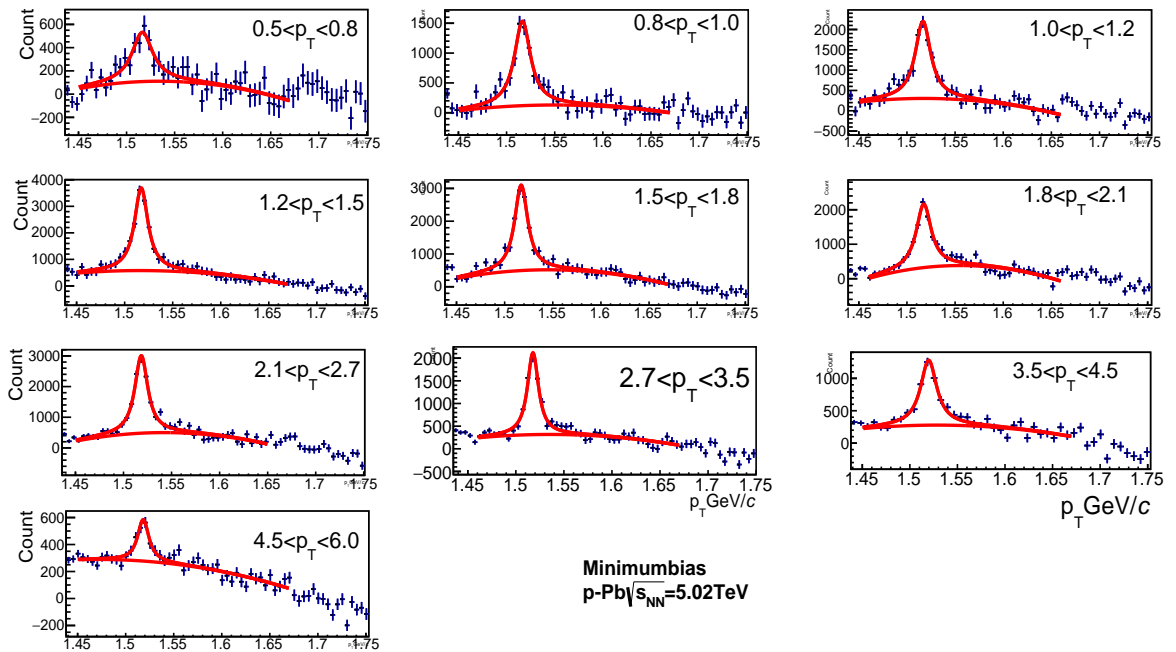


Figure 3.9: (Color online) These plots show Λ^* signal after subtracting MEB in different p_T bins in p-Pb minimum bias collisions at $\sqrt{s_{NN}} = 5.02$ TeV.

3 Measurement of $\Lambda(1520)$ resonance production in pp and p-Pb collisions

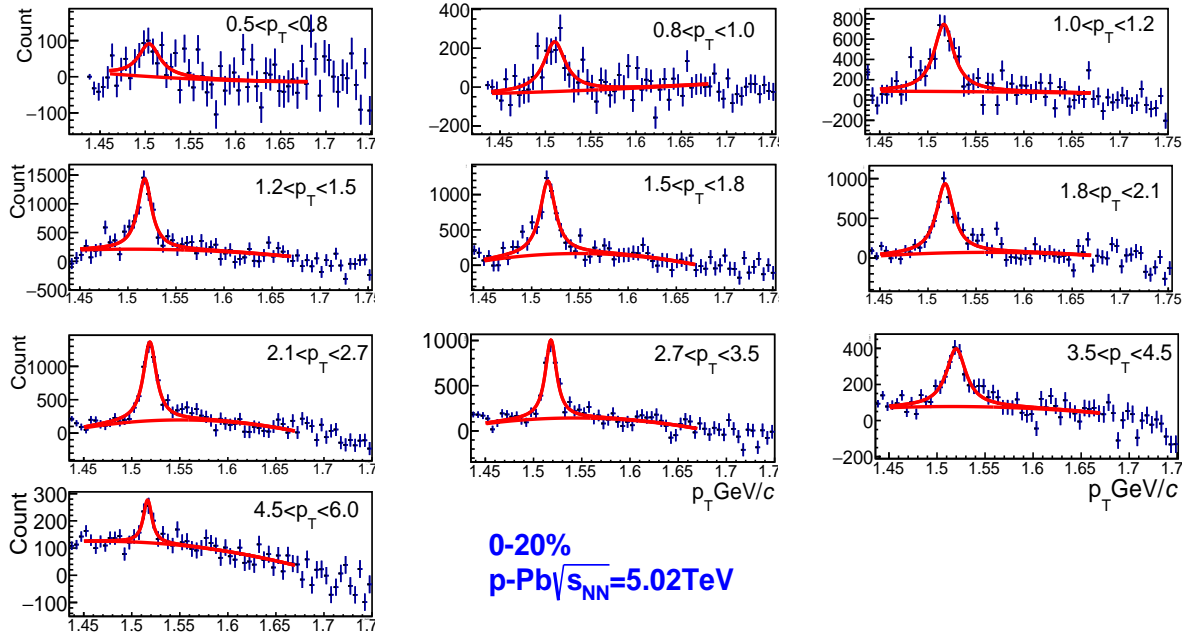


Figure 3.10: (Color online) These plots show Λ^* signal after subtracting MEB in different p_T bins in p-Pb collisions at $\sqrt{s_{NN}} = 5.02$ TeV for 0-20% multiplicity bin.

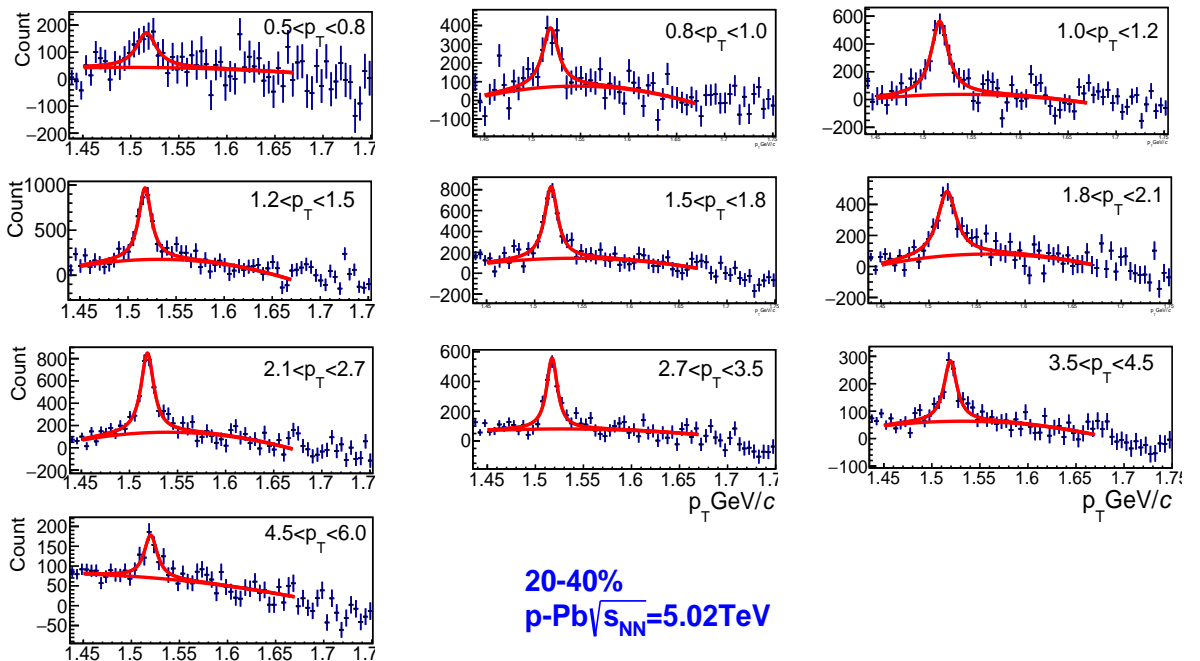


Figure 3.11: (Color online) These plots show Λ^* signal after subtracting MEB in different p_T bins in p-Pb collisions at $\sqrt{s_{NN}} = 5.02$ TeV for 20-40% multiplicity bin.

3.5 Raw yield extraction

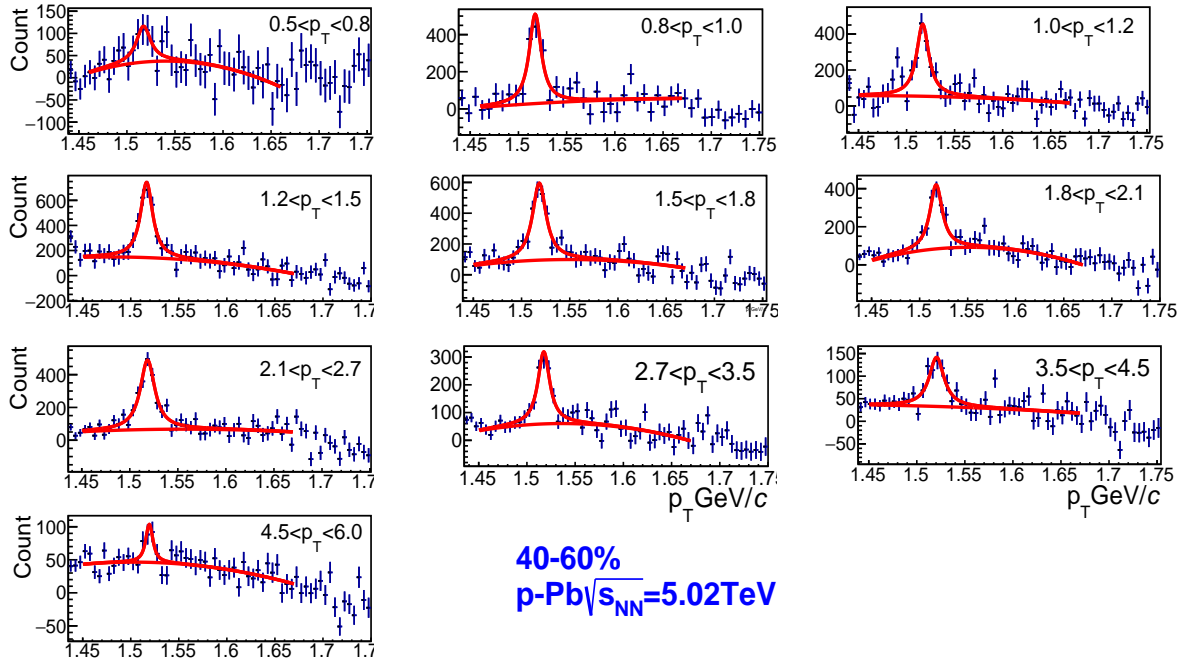


Figure 3.12: (Color online) These plots show Λ^* signal after subtracting MEB in different p_T bins in p-Pb collisions at $\sqrt{s_{NN}} = 5.02$ TeV for 40-60% multiplicity bin.

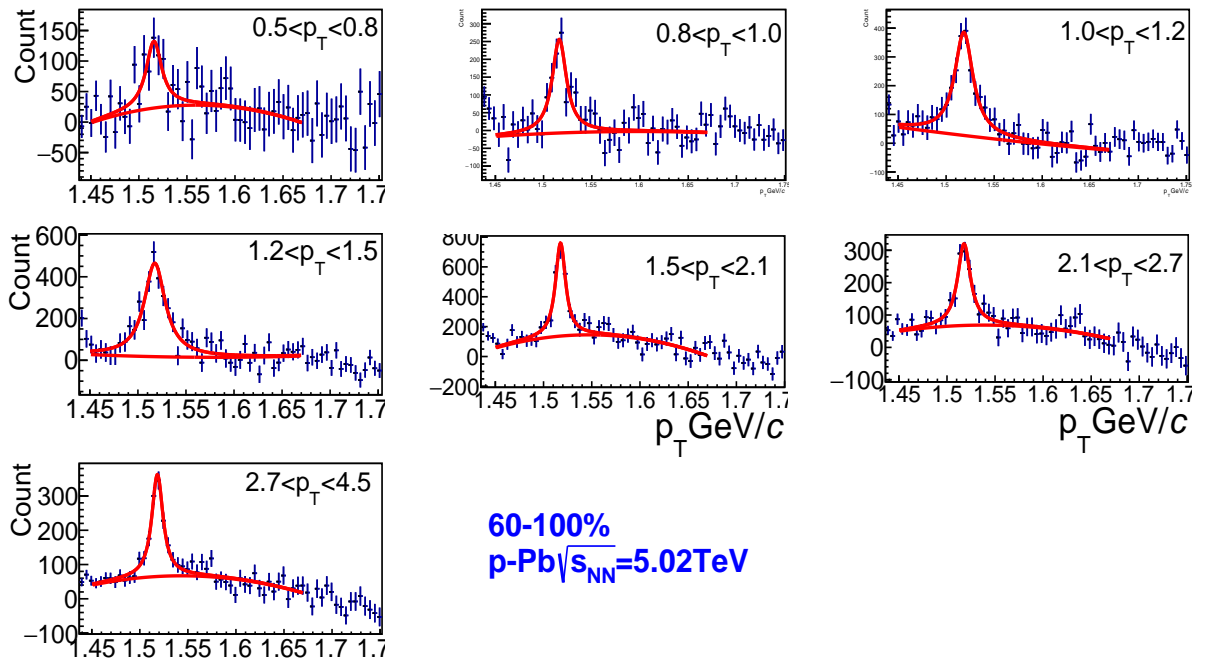


Figure 3.13: (Color online) These plots show Λ^* signal after subtracting MEB in different p_T bins in p-Pb collisions at $\sqrt{s_{NN}} = 5.02$ TeV for 60-100% multiplicity bin.

3.6 Raw yield correction

The raw yield of Λ^* has been corrected for the loss due to the detector acceptance, efficiency and the choice of track parameters made to improve the signal over the background. The reconstruction efficiency \times acceptance (ϵ_{eff}) of the detectors for Λ^* is calculated using the Monte Carlo simulation DPMJET [104] for p-Pb collisions and PYTHIA [104] for pp collisions. The generated Λ^* from monte-carlo events within a rapidity interval as given for real data are passed through the ALICE detector simulation, GEANT3 [105]. The ratio of number of Λ^* those are reconstructed after passing through all the track cuts and PID cuts in GEANT as given in real data to the input number of Λ^* within the same rapidity interval gives the reconstruction efficiency \times acceptance. This correction is p_T dependent and can be written as

$$\epsilon_{eff}(p_T) = \frac{N_{Reconstructed}^{\Lambda^*}}{N_{Generated}^{\Lambda^*}} \quad (3.5)$$

The efficiency \times acceptance contribution, shown in Fig. 3.14 is strongly p_T -dependent but independent of multiplicity bins for p-Pb collisions. In going from lower p_T bins to higher p_T bins, the track selection is switching from a higher tracking efficient detector (TPC) to a comparatively lower tracking efficient detector (TOF). So there is a dip in the reconstruction efficiency at $p_T \sim 2 \text{ GeV}/c$.

Apart from the above correction, the raw yield has been corrected by branching ratio of pK hadronic decay channel which is 0.225. The raw yield is also corrected for trigger efficiency and vertex efficiency. The final p_T spectra is

given as follows.

$$\frac{d^2N}{dp_T dy} = \frac{1}{N_{evt}} \frac{N_{raw} \varepsilon_{trigger} \varepsilon_{vertex}}{BR \varepsilon_{eff}} \frac{1}{dp_T dy}, \quad (3.6)$$

where

- N_{raw} is the raw yield
- N_{evt} is the number of events after physics selection,
- ε_{vertex} is the vertex correction factor,
- $\varepsilon_{trigger}$ is the correction to inelastic trigger class in pp collisions and correction to the non-single diffractive trigger class in p-Pb minimum bias collisions,
- BR is the branching ratio,
- ε_{eff} is the detector efficiency×acceptance,
- dp_T, dy are the width of transverse momentum and rapidity window, respectively.

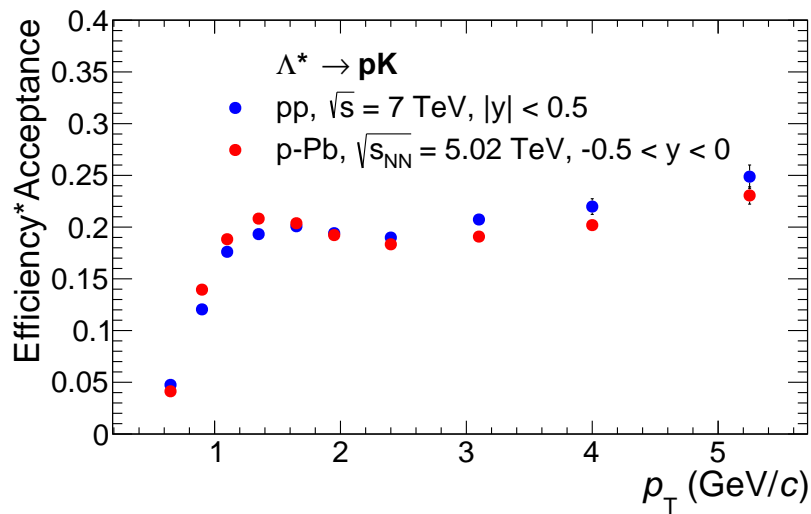


Figure 3.14: (Color online) The blue and red circles show the reconstruction efficiency×acceptance for pp collisions and p-Pb collisions, respectively.

3.7 Systematic uncertainties

The systematic uncertainties for Λ^* p_T -differential yields have been calculated from several sources. The strategy for calculating systematic uncertainty is as follows. If there are 2 or more alternative yields for a specific source of yield extraction (say different fitting ranges), then the standard deviation of default and alternative yields has been used as the systematic uncertainty for that specific source. If there is only one alternative yield, then the difference between the default yield and the alternative one has been chosen as systematic uncertainty for that source. The Barlow consistency check [106] has been done to confirm whether the source is really contributing to the systematic uncertainty or this is only a statistical fluctuation. Let each measurement be indicated by $(y_i \pm \sigma_i)$ and the central value (default measurement) by $(y_c \pm \sigma_c)$, one can define $\Delta\sigma_i$ as

$$\Delta\sigma_i = \sqrt{|\sigma_i^2 - \sigma_c^2|} \quad (3.7)$$

Then one calculates $n_i = \Delta y_i / \Delta\sigma_i$, where $\Delta y_i = (y_c - y_i)$. If $n_i < 1.0$, then the effects are due to the statistical fluctuation otherwise there is a systematic effect which means that the two measurements are not compatible within the statistical errors. In our case, for a measurement (i), we have calculated the distribution n_i for all p_T bins of Λ^* . If the measurement is consistent then the mean of the distribution will be close to zero and their rms will be within 1. The measurements which have passed (inconsistent) the Barlow check, they have been used to determine the systematic uncertainty.

Different sources of uncertainties are briefly discussed below.

Due to yield extraction

After subtracting combinatorial background, for raw yield extraction a signal

peak is fitted with a Voigtian function over a polynomial fit. A fitting range, normalisation range, 2^{nd} order polynomial and a mass resolution value are required to extract the raw yield. The raw yield has been calculated using "bin counting" method where one adds the bin counts in the ± 2 times the PDG width of Λ^* about the mass peak position and corrects for the tail fraction from the Voigtian fit. So to calculate the uncertainties, the yields have been extracted for 3 alternative fitting ranges, 2 alternative normalisation ranges, using a 3^{rd} order polynomial, mass resolution calculated from a different way and yield from direct Voigtian and 2^{nd} order polynomial fit.

Due to track cuts

Before selecting a track, different quality cuts have been applied on the track. Mainly, they are TPC cluster cut, TPC crossed rows, DCA cut along Z-axis and in XY-plane, χ^2/ndf for fitting clusters in TPC, global χ^2/ndf cut, etc.. By varying the default values of the cuts, their respective uncertainties have been calculated.

Due to PID cut

For particle identification, a 3 times the detector resolution cut has been applied on each track before invariant mass reconstruction. So this cut range is also varied to get the uncertainty.

Due to material budget and hadronic interaction

A Λ^* can decay to a proton and a kaon. To get the uncertainty due to material budget (MB) and hadronic interaction (HI) one has to know these uncertainties for proton and kaon tracks separately. So the MB uncertainty for Λ^* is the sum of MB uncertainty of its decayed proton and kaon tracks. This is similar for HI uncertainty.

The total uncertainty which is the quadrature sum of uncertainties from all source has been shown in Fig. 3.15 for pp and for p-Pb collisions at different

3 Measurement of $\Lambda(1520)$ resonance production in pp and p-Pb collisions

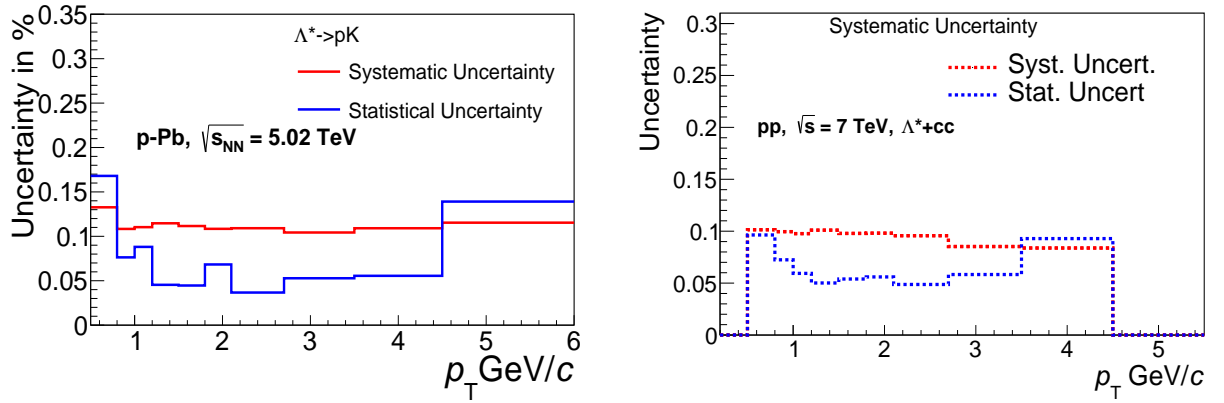


Figure 3.15: (Color online) Red line shows the total systematic uncertainties and blue line shows the statistical uncertainties for minimum bias p-Pb collisions on the left plot and for minimum bias pp collisions on the right plot in different p_T bins.

p_T bins. Since the source of uncertainties are same for minimum bias and for different multiplicity bins, the uncertainties calculated for minimum bias has been used for different multiplicity bins in p-Pb collisions.

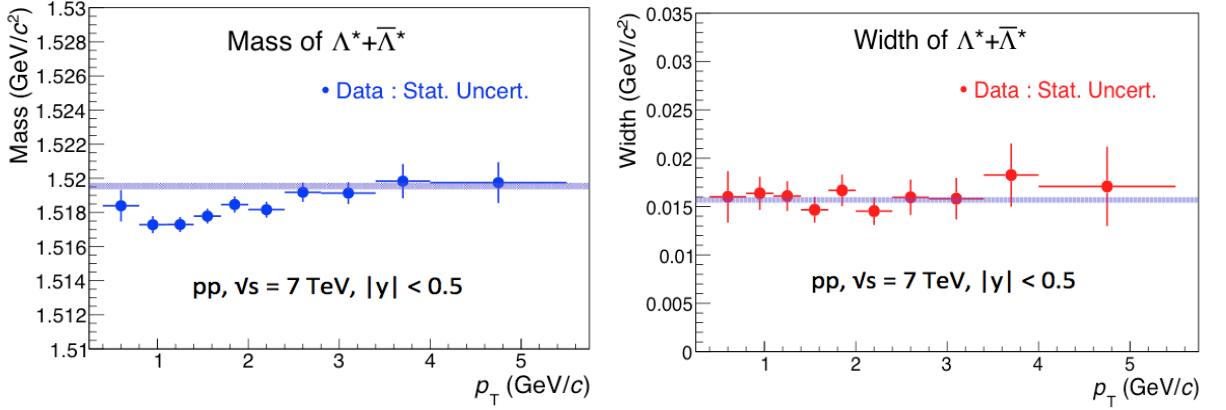


Figure 3.16: (Color online) The left and on the right plots show the mass and width of Λ^* , respectively. The shadowed bands show their respective PDG values.

3.8 Results

3.8.1 Mass and Width

The mass and width of Λ^* are shown in Fig. 3.16 for pp collisions at $\sqrt{s} = 7 \text{ TeV}$. Only statistical uncertainties are shown for both the results. There is a little drop in mass of Λ^* from its PDG value, but the measured width matches with the PDG value within the statistical uncertainty.

3.8.2 Transverse momentum spectra

The measured spectrum for Λ^* in pp collisions is reported in Fig. 3.17 and in minimum bias p-Pb collisions and its four multiplicity bins are reported in Figs. 3.18 to 3.23. Each spectrum is fitted with 4 different functions: Tsallis-Levy [107], Boltzmann-Gibbs blastwave [108], m_T exponential and Boltzmann functions:

1. Tsallis-Levy function:

$$\frac{1}{N_E} \frac{d^2N}{dp_T dy} = p_T \times \frac{dN}{dy} \times \frac{(n-1)(n-2)}{nC[nC + m(n-2)]} \times \left[1 + \frac{m_T - m}{nC} \right]^{-n}, \quad (3.8)$$

3 Measurement of $\Lambda(1520)$ resonance production in pp and p-Pb collisions

where $m_T = \sqrt{m^2 + p_T^2}$. C is the inverse slope parameter and n is the exponent. The Tsallis-Levy function describes both the exponential shape at lower p_T and power law distribution at higher p_T .

2. Boltzmann-Gibbs blast-wave function:

$$\frac{1}{N_E} \frac{d^2N}{dp_T dy} \propto p_T \int_0^R r dr m_T I_0\left(\frac{p_T \sinh \rho}{T_{kin}}\right) K_1\left(\frac{m_T \cosh \rho}{T_{kin}}\right), \quad (3.9)$$

where the velocity profile ρ is described by

$$\rho = \tanh^{-1} \beta_T = \tanh^{-1} \left(\left(\frac{r}{R} \right)^n \beta_s \right). \quad (3.10)$$

Here I_0 and K_1 are the modified Bessel functions, r the radial distance from the centre of the fireball in the transverse plane, R the radius of the fireball, $\beta_T(r)$ is the transverse expansion velocity, β_s the transverse expansion velocity

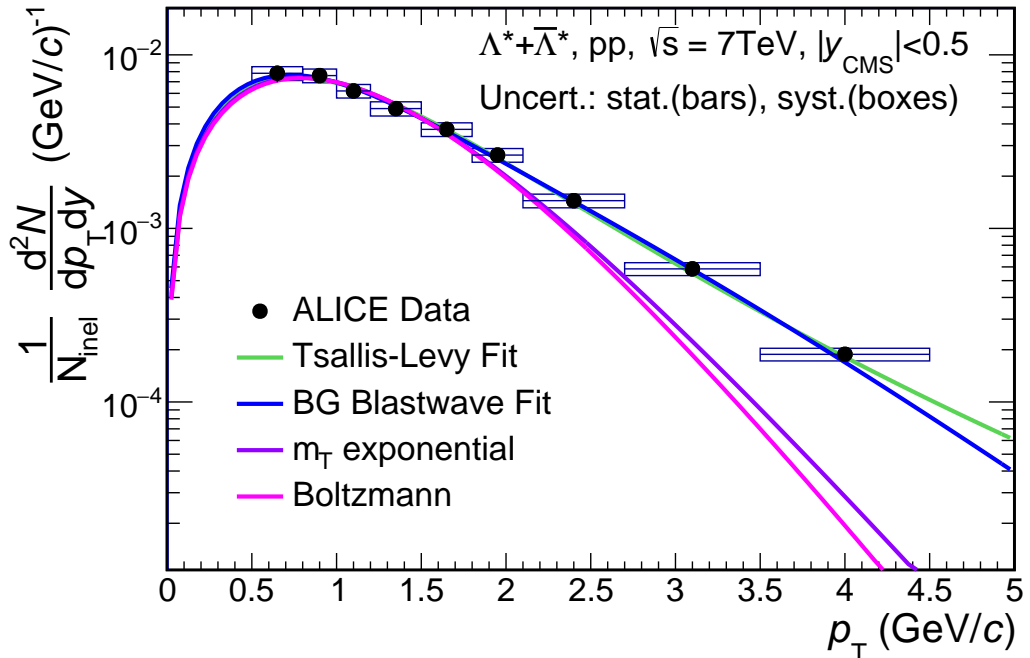


Figure 3.17: (Color online) In the figure, the black markers show the p_T -spectrum of Λ^* in pp collisions at $\sqrt{s} = 7$ TeV and is fitted with Tsallis-Levy (green), BG blastwave (blue), m_T exponential (violet) and Boltzmann (magenta) functions.

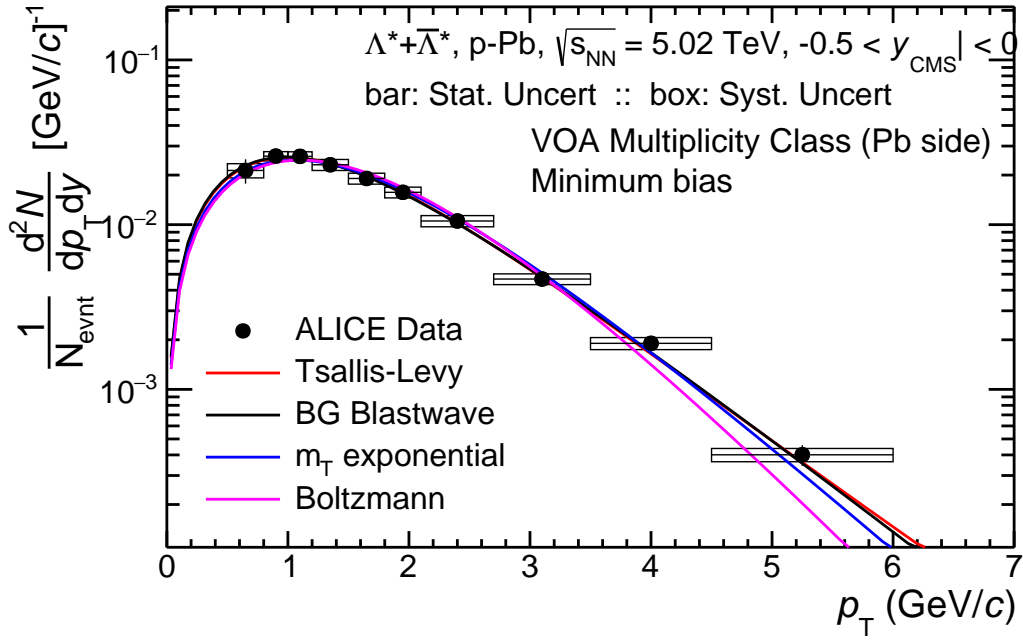


Figure 3.18: (Color online) In the figure, the black markers show the p_T -spectrum of Λ^* in minimum bias p-Pb collisions at $\sqrt{s_{NN}} = 5.02$ TeV and is fitted with Tsallis-Levy (red), BG blastwave (black), m_T exponential (blue) and Boltzmann (magenta) functions.

at the surface, n the exponent of the velocity profile and T_{kin} is the temperature of the kinetic freeze-out surface of the produced particle.

3. m_T Exponential:

$$\frac{1}{N_E} \frac{d^2N}{dp_T dy} = A p_T e^{-\frac{m_T}{C}} \quad (3.11)$$

where A is the normalisation factor and C is the inverse slope parameter.

Only Tsallis-Levy, BG blastwave can explain the Λ^* spectra over all p_T bins. The Tsallis-Levy fit has been chosen as the default fit for extracting the p_T integrated yield (dN/dy) and mean transverse momentum ($\langle p_T \rangle$) of the Λ^* for all cases. The fitting ranges of m_T Exponential and Boltzmann functions have been restricted in higher p_T region so that they can better explain the lower p_T points. These functions have been used to calculate uncertainty for dN/dy and $\langle p_T \rangle$ in lower extrapolation region.

3 Measurement of $\Lambda(1520)$ resonance production in pp and p-Pb collisions

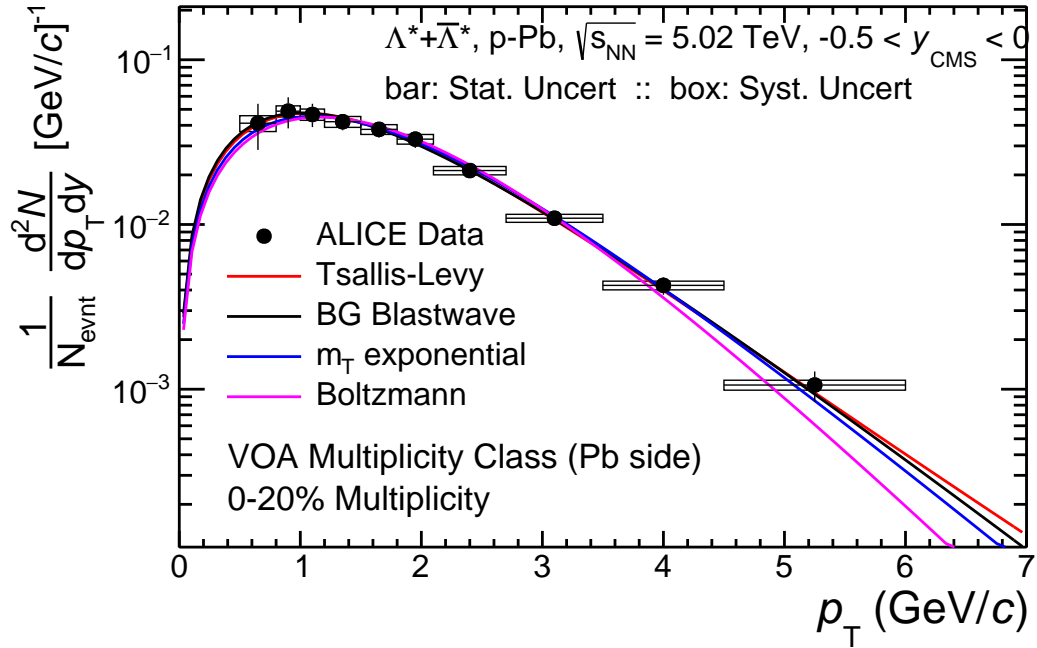


Figure 3.19: (Color online) Same as Fig. 3.18, but for 0-20% multiplicity bin.

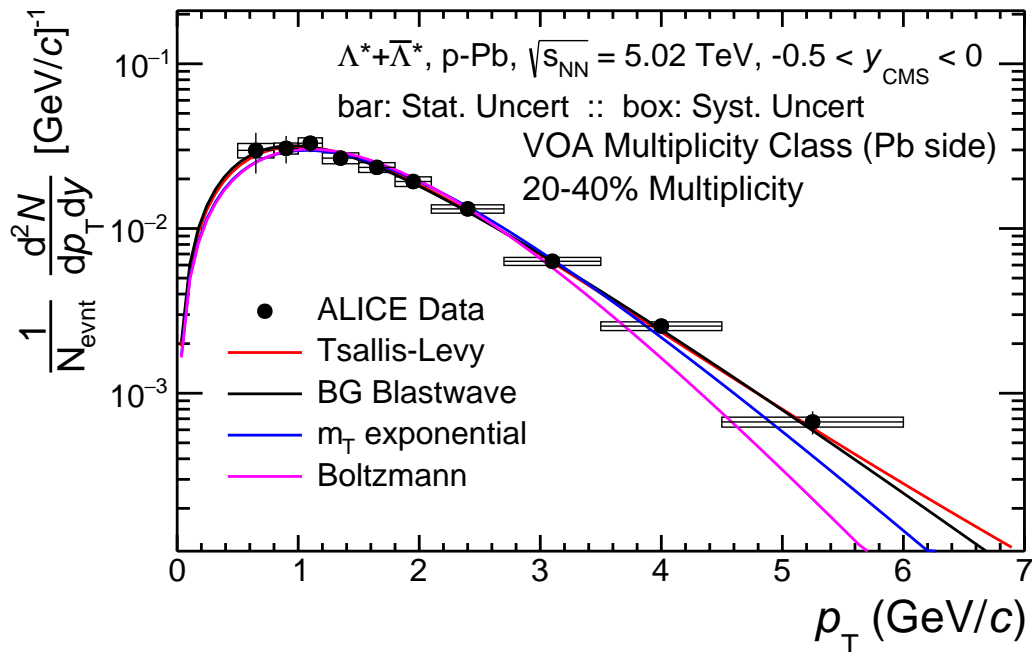


Figure 3.20: (Color online) Same as Fig. 3.18, but for 20-40% multiplicity bin.

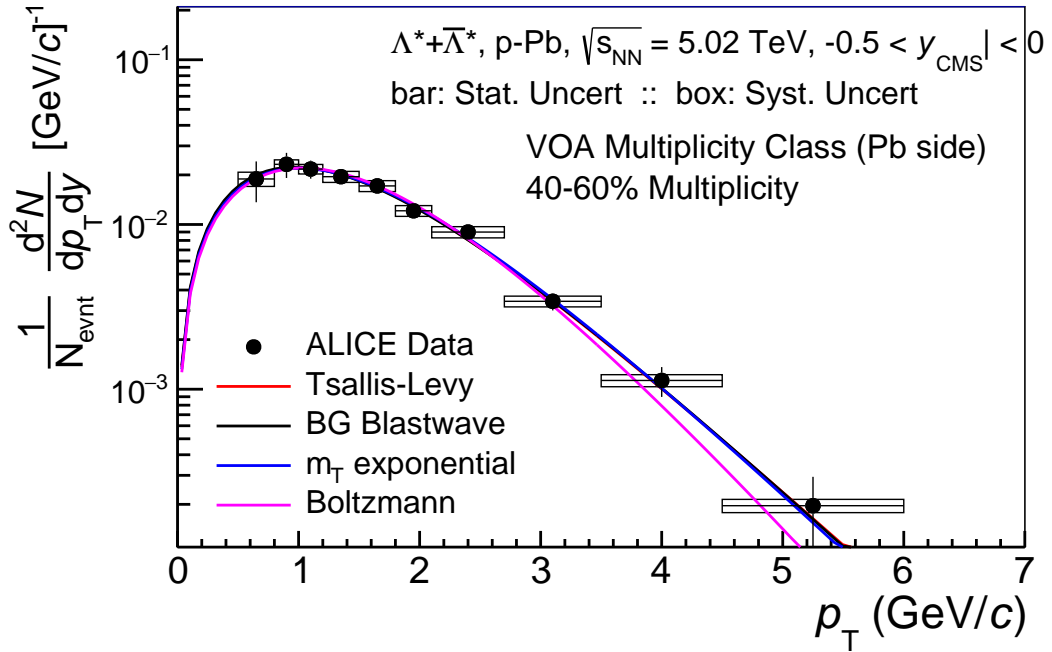


Figure 3.21: (Color online) Same as Fig. 3.18, but for 40-60% multiplicity bin.

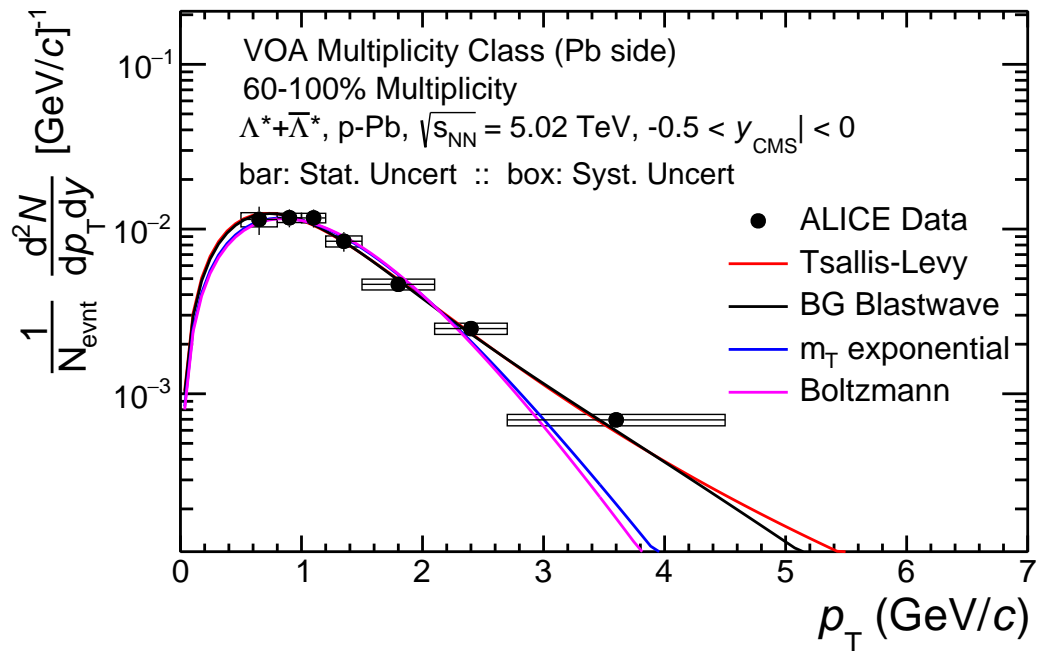


Figure 3.22: (Color online) Same as Fig. 3.18, but for 60-100% multiplicity bin.

3 Measurement of $\Lambda(1520)$ resonance production in pp and p-Pb collisions

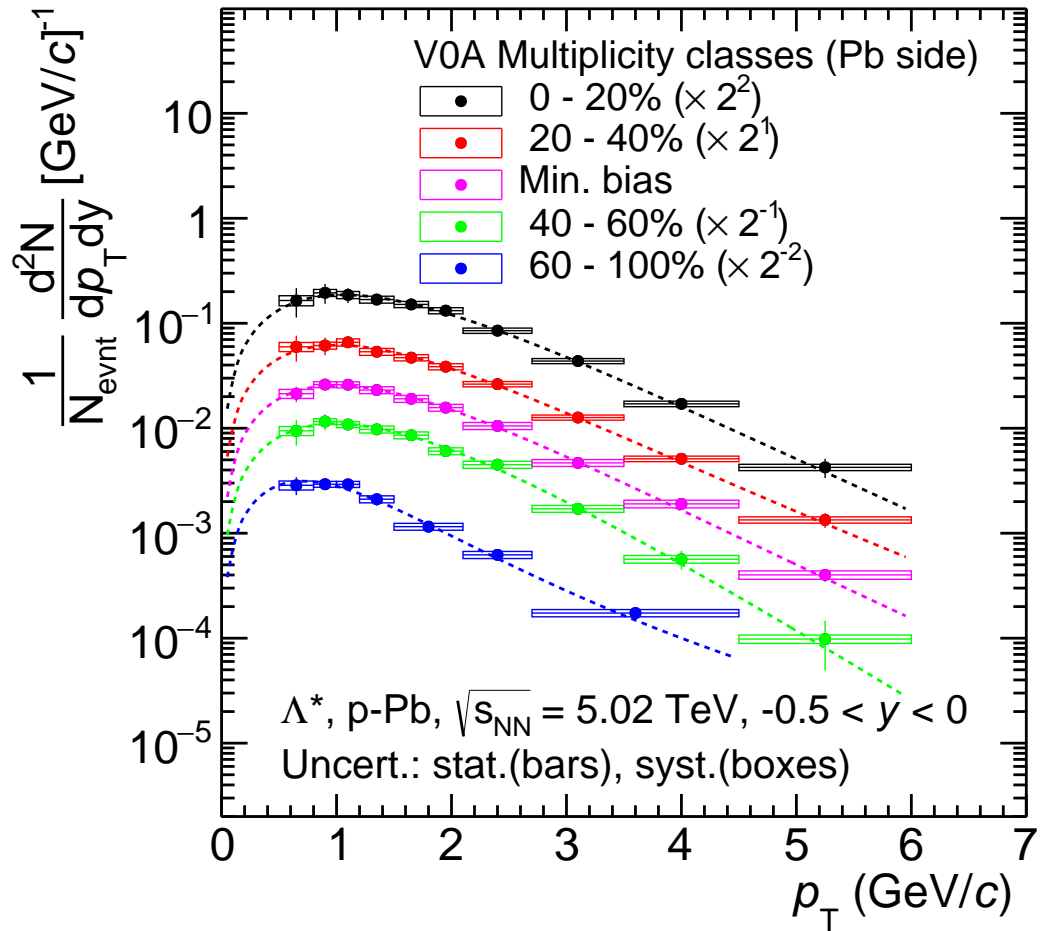


Figure 3.23: (Color online) The figure shows p_T spectra of Λ^* in p-Pb collisions for minimum bias (magenta), 0-20% (black), 20-40% (red), 40-60% (green) and 60-100% (blue) multiplicity bins. All spectra are fitted separately with Tsallis-Levy function.

Tsallis-Levy fit parameters			
System	$C(\text{GeV})$	n	χ^2/ndf
pp , Minimum bias	0.314 ± 0.030	7.51 ± 1.52	0.4
p-Pb , Minimum bias	0.539 ± 0.029	26.89 ± 12.08	0.35
p-Pb , 0-20%	0.587 ± 0.030	30.2 ± 14.8	0.27
p-Pb , 20-40%	0.525 ± 0.028	15.9 ± 3.4	0.4
p-Pb , 40-60%	0.532 ± 0.026	90.0 ± 112.2	0.54
p-Pb , 60-100%	0.284 ± 0.029	5.84 ± 1.096	1.13

Table 3.1: Tsallis-Levy fit parameters to Λ^* spectra in pp and p-Pb collisions.

BG Blast Wave fit parameters				
System	T (GeV)	β_s	n	χ^2/ndf
pp , Minimum bias	0.198 ± 0.055	0.788 ± 0.037	3.13 ± 0.714	0.31
p-Pb , Minimum bias	0.318 ± 0.176	0.679 ± 0.217	1.639 ± 0.038	0.37
p-Pb , 0-20%	0.278 ± 0.147	0.752 ± 0.162	1.49 ± 0.21	0.27
p-Pb , 20-40%	0.288 ± 0.107	0.761 ± 0.099	1.94 ± 0.38	0.35
p-Pb , 40-60%	0.256 ± 0.132	0.691 ± 0.205	1.33 ± 0.43	0.61
p-Pb , 60-100%	0.248 ± 0.058	0.814 ± 0.053	4.87 ± 2.87	1.31

Table 3.2: Boltzmann Gibbs Blast-Wave fit parameters to Λ^* spectra in pp and p-Pb collisions.

3.8.3 Yield and mean transverse momentum

The dN/dy of Λ^* has been calculated as the sum of integral of fit function in the lower extrapolation region, yield from data point and integral of fit function in the higher extrapolation region. The results from Tsallis-Levy fit has been used as the default results of dN/dy and $\langle p_T \rangle$. Other functions have been used to calculate the systematic uncertainty. The table 3.3 shows the dN/dy and $\langle p_T \rangle$ of Λ^* in pp and p-Pb collisions.

3.8.4 Comparison and ratio

The plots in the Fig. 3.24 show the comparison of dN/dy and $\langle p_T \rangle$ of Λ^* with the published results of STAR in pp collisions at $\sqrt{s} = 200$ GeV [110]. There is a significant increase in the results from RHIC to LHC energy. The Fig. 3.25 shows the $\langle p_T \rangle$ of different particles having different masses in pp

3 Measurement of $\Lambda(1520)$ resonance production in pp and p-Pb collisions

Tsallis-Levy fit results		
System	dN/dy	$\langle p_T \rangle$
System	\pm Stat. \pm Syst.	\pm Stat. \pm Syst.
pp, Minimum bias	$0.012 \pm 0.0003 \pm 0.001$	$1.27 \pm 0.021 \pm 0.041$
p-Pb, Minimum bias	$0.051 \pm 0.0014 \pm 0.004$	$1.59 \pm 0.025 \pm 0.035$
p-Pb, 0-20%	$0.102 \pm 0.0052 \pm 0.008$	$1.67 \pm 0.050 \pm 0.038$
p-Pb, 20-40%	$0.066 \pm 0.0031 \pm 0.005$	$1.62 \pm 0.046 \pm 0.037$
p-Pb, 40-60%	$0.043 \pm 0.0021 \pm 0.003$	$1.51 \pm 0.041 \pm 0.032$
p-Pb, 60-100%	$0.020 \pm 0.001 \pm 0.002$	$1.35 \pm 0.063 \pm 0.048$

Table 3.3: dN/dy and $\langle p_T \rangle$ of Λ^* in pp and p-Pb collisions from Tsallis-Levy fit.

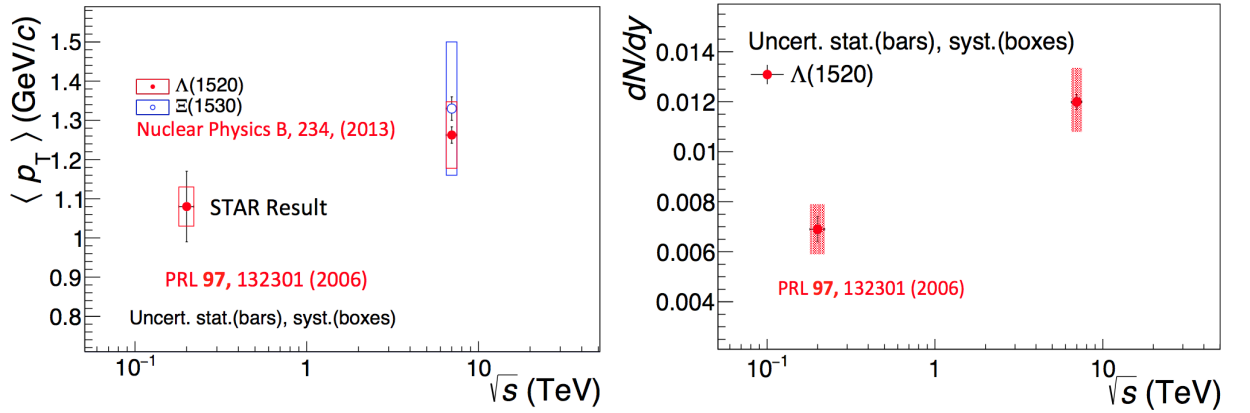


Figure 3.24: (Color online) The left plot shows the $\langle p_T \rangle$ of Λ^* (red marker) versus energy in pp collisions. The right plot shows dN/dy of Λ^* versus energy in pp collisions. [110]

collisions at different colliding energies [111]. The figure shows the $\langle p_T \rangle$ increases by increasing colliding energy and is higher for heavier mass particles. The Fig. 3.26 shows the yield ratio of $\Lambda(1520)$ and $\Lambda(1115)$ at $\sqrt{s} = 200$ GeV and 7 TeV. The prediction of statistical hadronization model [112] in pp collisions at $\sqrt{s} = 7$ TeV and $T = 160$ MeV agrees with the data within systematic uncertainty. The Figs. 3.27 and 3.28 show the measured dN/dy and $\langle p_T \rangle$ values of Λ^* in p-Pb collisions in minimum bias, in 4 multiplicity bins and in pp collisions. These measured values are compared with the measured $\langle p_T \rangle$ values of other particles in p-Pb collisions at the LHC energies [116]. This shows Λ^* follows the mass ordering. The Fig. 3.29 shows the ratios of $\Lambda(1520)$ yield over $\Lambda(1115)$ yield as a function of charge multiplicity in p-Pb

collisions at $\sqrt{s_{NN}} = 5.02$ TeV and in pp collisions at $\sqrt{s} = 200$ GeV and 7 TeV. The measurement shows that the ratio of a resonance over a stable particles stays flat over all charge multiplicity regions. So we may conclude that there is no significant effect of hadronic scattering medium on Λ^* yield. So the life span of the scattering medium in p-Pb collisions at $\sqrt{s_{NN}} = 5.02$ TeV is small enough compared to the life-time of Λ^* . But as shown in the Fig. 3.30, the published result of ALICE is showing a significant effect of the hadronic scattering medium on K^{*0} yield [113]. The figure shows the ratio of K^{*0} over K^- and ϕ over K^- . K^{*0} has a very small decay length (~ 4 fm), so the K^{*0} is showing suppression in its yield in larger system size compared to the smaller system size.

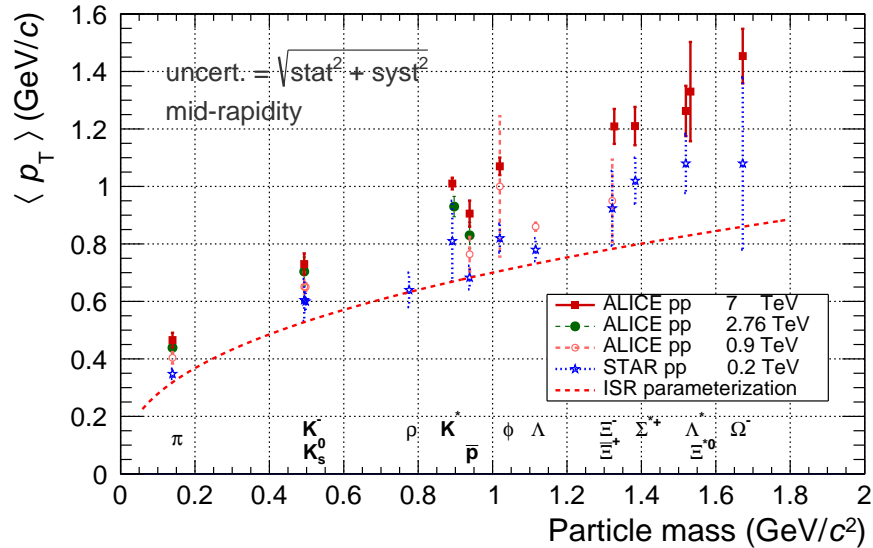


Figure 3.25: (Color online) The figure shows the $\langle p_T \rangle$ of different particles having different masses. Red solid markers, green solid circles and open red circles are showing the pp collision results published by ALICE at $\sqrt{s} = 7$ TeV, 2.76 TeV and 900 GeV, respectively. Star markers are showing the results of pp at $\sqrt{s} = 200$ GeV from STAR experiment. Dashed red line is showing the ISR parameterization [111].

3 Measurement of $\Lambda(1520)$ resonance production in pp and p-Pb collisions

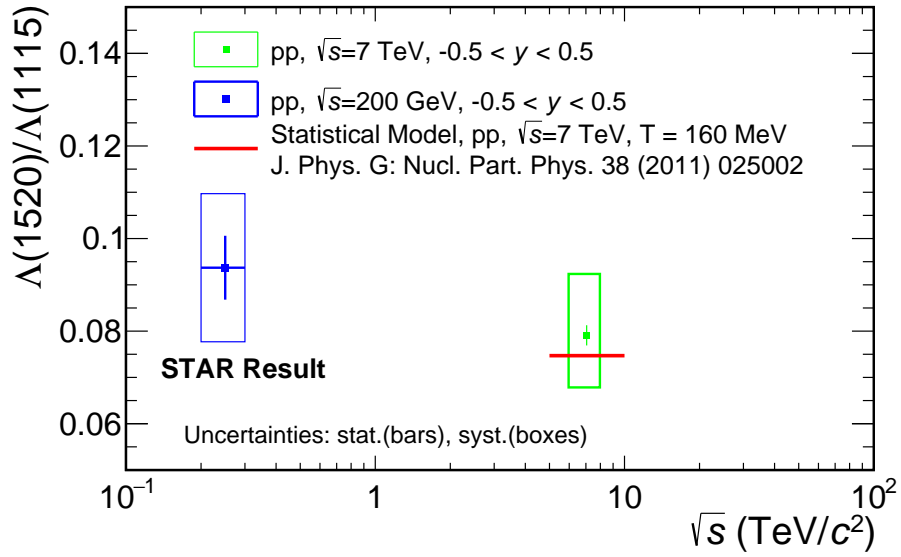


Figure 3.26: (Color online) The figure shows the ratio of $\Lambda(1520)$ yield and $\Lambda(1115)$ yield in pp collisions at $\sqrt{s} = 200$ GeV and 7 TeV by blue and green markers, respectively. Red line shows the prediction of statistical hadronization model [112].

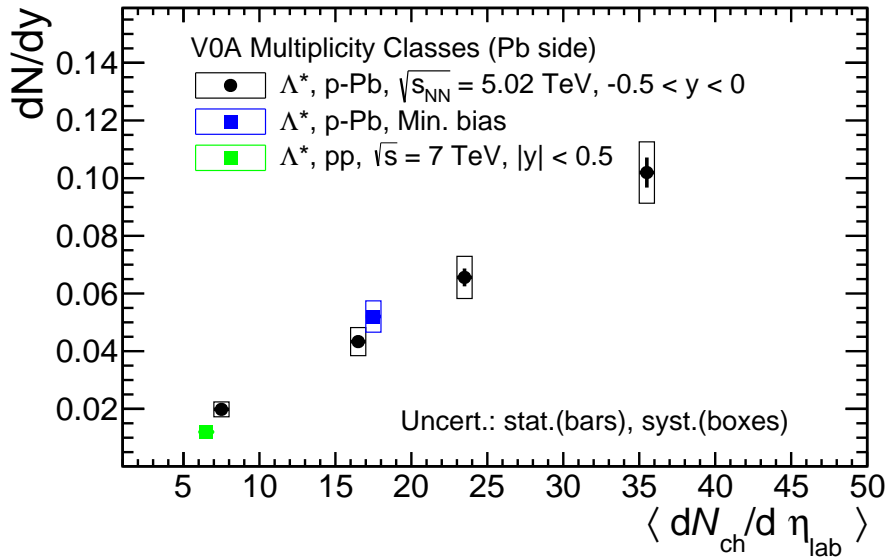


Figure 3.27: (Color online) The figure shows the measured values of dN/dy for Λ^* in p-Pb collisions for minimum bias (blue solid markers), multiplicity bins (black solid markers) and in pp collisions (solid green markers).

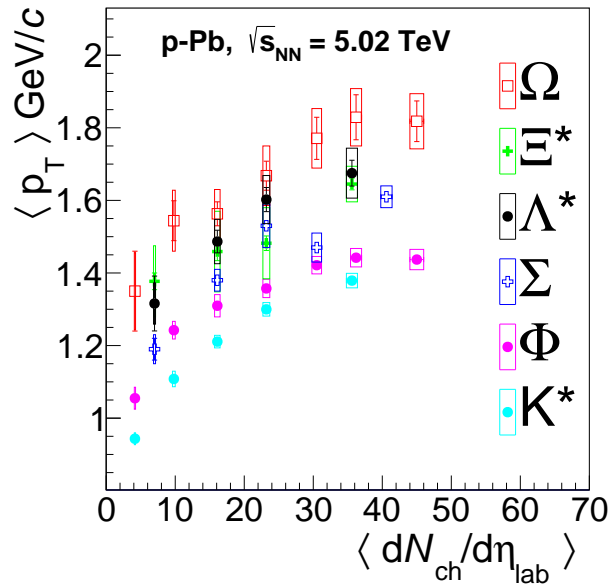


Figure 3.28: (Color online) The figure shows the measured values of $\langle p_T \rangle$ for Λ^* (black), Ω (red), Ξ^* (green), Σ (blue), ϕ (magenta) and K^* (cyan) in p-Pb collisions.

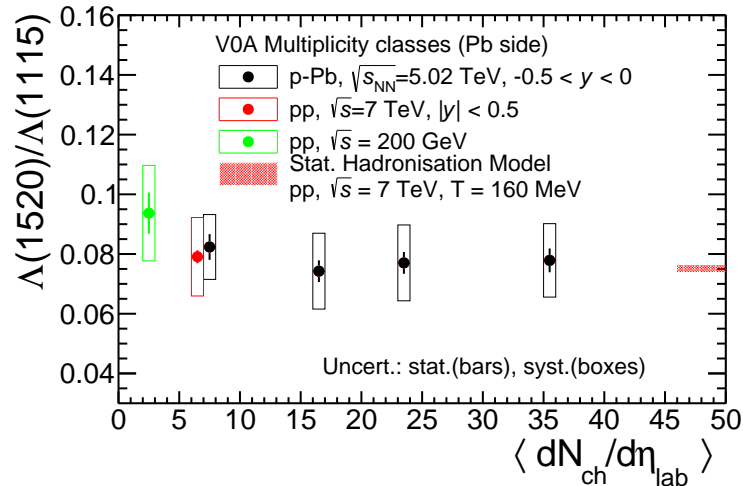


Figure 3.29: (Color online) The figure shows the ratio of $\Lambda(1520)$ yield over $\Lambda(1115)$ yield in p-Pb collisions at $\sqrt{s_{NN}} = 5.02$ TeV by black solid markers and same in pp collisions at $\sqrt{s} = 200$ GeV and 7 TeV by green and red markers, respectively. Red band shows the prediction of statistical hadronization model.

3 Measurement of $\Lambda(1520)$ resonance production in pp and p-Pb collisions

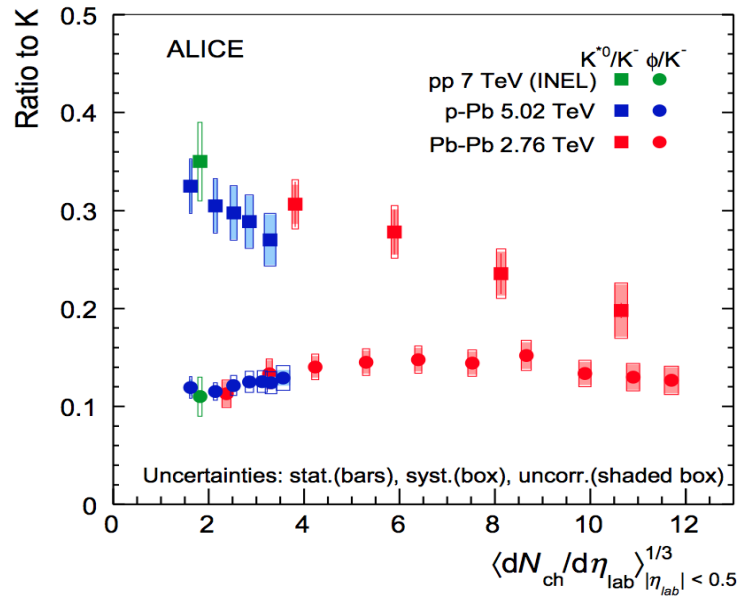


Figure 3.30: (Color online) Ratio of K^{*0} and ϕ to charged K measured in the three collision systems, as a function of the cube root of the average charged particle density ($\langle dN_{ch}/d\eta_{lab} \rangle^{1/3}$) measured at mid-rapidity, used as a proxy for the system size. Squares represent K^{*0}/K , circles refer to ϕ/K . Statistical uncertainties (bars) are shown together with total (hollow boxes) and multiplicity-uncorrelated (shaded boxes) systematic uncertainties. Measurements in pp at $\sqrt{s} = 7$ TeV and Pb-Pb collisions at $\sqrt{s_{NN}} = 2.76$ TeV are taken from [114] and [115], respectively.

3.9 Summary

We have extracted the yield, measured the mass, decay width, $\langle p_T \rangle$ of Λ^* in pp and p-Pb collisions at the LHC energies. Mass of Λ^* drops by half a % from the PDG value and the decay width is in agreement with the PDG value within statistical uncertainty in pp collisions at $\sqrt{s} = 7$ TeV. The p_T -spectra from minimum bias pp and p-Pb collisions and from 4 multiplicity bins from p-Pb collisions are fitted with 4 different function. Out of which Tsallis-Levy and BG blastwave are able to explain the spectra for whole p_T range. The measured dN/dy and $\langle p_T \rangle$ values of Λ^* are compared with the same measured values at different energies and with different particles. The yield ratios of Λ^* over $\Lambda(1115)$ are obtained in different multiplicity classes in p-Pb collisions and minimum bias pp collisions. The ratios from multiplicity bins in p-Pb collisions is similar as that in pp collisions, showing no significant effect of hadronic rescattering on Λ^* yield in p-Pb collisions. Where as, K^{*0}/K ratios showing a suppression from lower to higher multiplicity bins, hence suggesting a hadronic scattering medium in p-Pb collisions at $\sqrt{s_{NN}} = 5.02$ TeV.

4 Production of D mesons in pp and p-Pb collisions at the LHC energies

4.1 Introduction

Relativistic heavy ion collisions at the RHIC [21] and the LHC [22] have given rise to a new phase of matter. When two heavy ions collide, a system of deconfined gluons and quarks within a very small volume is created. The initial energy density within this volume is found to be much larger than nuclear ground state energy density. This state of matter as we know today is called Quark Gluon Plasma (QGP) [117, 118]. The study of QGP is particularly important as it aims to produce a condition, which resembles the period when universe was only a few microseconds old. However, since this exotic system created in the experiments exists only for a very short period of time and is not directly observable, only signals originating from the matter itself that survive and are measured after the collisions can provide a window into the nature of the QGP [119, 120]. With high statistics data already accumulated at the Large Hadron Collider at CERN, the scientific community has an enormous task to analyse, and explain these observations and extract information about the properties of the QGP. These analyses are also leading the way for

additional measurements and will become available for studies with all the major experiments, like STAR [121], ALICE [122] and proposed CBM at FAIR [123].

One of the prominent signatures coming out of the QGP phase is jet quenching. High momentum hadron spectra are observed to be highly suppressed relative to those in pp collisions [124, 125], suggesting a quenching effect due to deconfined matter. A similar effect is observed for high p_T charm or beauty quarks with most recent results showing suppression of D or B mesons to same order as that of light hadrons [126]. However before going into hot and dense matter effects, it is absolute necessary to fix the baseline for such observations. In heavy ion scenario, pp collisions serve as the baseline for such observations, assuming that no nuclear effects are present when pp is scaled to p-Pb or Pb-Pb data only by a factor. On the other hand, it has been suggested that the modification in spectra of the observed particles in the heavy ion collision have effects of cold nuclear matter [127] before formation of QGP, which are often masked by hot and dense matter effects. So it is important to discern the contributions of the cold nuclear effects from all other effects due to QGP on the final particle spectra. p-Pb collisions give us a unique opportunity to study these initial nuclear effects. The so called effect due to shadowing has been playing a role in the particle production scenario for a very long time. With the assumption that any nucleus is not just any conglomeration of protons is the very essence of this phenomenon. With LHC achieving it's top collider energy, it may not be possible to overlook the shadowing features affecting the high gluon density within the nucleus. This phenomenon is also represented mathematically as shadowing ratio, $R_s = F_A(x, Q^2)/(A * F_p(x, Q^2))$, and has been found to deviate from unity as explained in these early literatures [128], which makes this phenomenon as one of the most prominent feature of cold nuclear

effects. On the other hand, another phenomenon that may affect the final particle spectra is multiple rescattering of the colliding nucleons or their partons. This effect is known as Cronin effect [129]. This particular feature had been observed in the RHIC energy for non-photonic electrons nuclear modification data, which shows an enhancement in the charm spectrum below $p_T < 4.0$ GeV [130]. The results suggest that this particular effect may be observed in the low and mid- p_T region and may not be much effective in higher side of the momentum. We will come back to these two points later in our work.

Now let us move over to heavy quarks. Heavy quark owing to its large mass is produced much before the formation of quark gluon plasma [131]. It is also believed that heavy quarks remain free to probe thermalized medium without carrying any prior effects due to nucleus. From the recent result of p-Pb data and earlier d+Au data [132] on particle production, the value of R_{pPb} deviates from unity by almost 15% mostly in low and mid- p_T region, which shows a considerable cold nuclear matter effects on heavy quark production [133]. The current work aims to highlight some of these initial nuclear effects on measured heavy meson spectra.

4.2 Models used

4.2.1 The HIJING model

HIJING (Heavy-Ion Jet INteraction Generator)[134] is a Monte Carlo model designed mainly to explore the range of possible initial conditions that may occur in nuclear collisions at collider energies and to produce output that can be compared directly with a wide variety of nuclear collider experimental observables. The main features included in HIJING are as follows.

The formulation of HIJING is guided by Lund FRITIOF [135] and Dual Parton Model [136] for soft nuclear reaction at intermediate energy ($\sqrt{s_{NN}} \leq 20$ GeV). Multiple low p_T exchanges among the end point constituents are included to model initial state interactions. The PYTHIA [137] guides the pQCD processes where multiple minijet production with initial final state radiation are involved. To reproduce p+A or A+A results, the Eikonal formalism is used to calculate the number of minijets per inelastic pp collision. The model uses three-parameter Woods-Saxon nuclear density determined by electron scattering data [138]. A diffuse nuclear geometry decides the impact parameter dependence of the number of binary collisions [139].

The cross section for charm production formalism at the leading order is written as [140]

$$\frac{d\sigma_{cc}^{pp}}{dp_T^2 dy_1 dy_2} = K \sum_{a,b} x_1 f_a(x_1, p_T^2) x_2 f_b(x_2, p_T^2) \times \frac{d\sigma_{ab}}{d\hat{t}}, \quad (4.1)$$

here a, b are the parton species, y_1, y_2 are the rapidities of the scattered partons and x_1, x_2 are the fraction of momentum carried by the initial partons.

A factor K , of value 2.0 has been used used to account roughly for the higher order corrections. In HIJING, the parton structure functions, $f_a(x_1, p_T^2)$ are the

Duke-Owens [141] structure function set 1 and this is also implemented in PYTHIA. For the nuclear effect in A+A and p+A collisions, model follows the A dependence of the shadowing proposed in Ref.[142, 143] and uses its parameterization as

$$R_A(x) \equiv \frac{f_{a/A}(x)}{A f_{a/N}(x)} = 1 + 1.19 \ln^{1/6} A [x^3 - 1.5(x_0 + x_L)x^2 + 3x_0x_Lx] - \left[\alpha_A(r) - \frac{1.08(A^{1/3} - 1)}{\ln(A + 1)} \sqrt{x} \right] e^{-x^2/x_0^2}, \quad (4.2)$$

$$\text{where } \alpha_A(r) = 0.1(A^{1/3} - 1) \frac{4}{3} \sqrt{1 - r^2/R_A^2}.$$

Here r is the transverse distance of the interacting nucleon from its nucleus centre and R_A is the radius of the nucleus, and $x_0 = 0.1$ and $x_L = 0.7$. The most important nuclear dependence term is proportional to $\alpha_A(r)$ in Eq.4.2, which determines the shadowing for $x < x_0$, and the rest gives the overall very slow A dependence nuclear effect on the structure function in $x > x_L$.

We have used version 1.41

4.2.2 The AMPT model

A Multiphase Transport Model (AMPT) [144] is a hybrid transport model, which was developed to address non-equilibrium many body dynamics. Initially it was designed to describe physics in p+A and A+A from 5 GeV to 5.5 TeV. Outline of this model are as follows.

Initial distribution of nucleons inside nuclei taken from HIJING and is wood saxon in nature. Scattering among them are treated with Eikonal formalism. If momentum transfer (Q^2) $>$ cut off momentum (p_0), then these process produce minijet partons and treated with PYTHIA model. Reverse ($Q^2 < p_0$) leads to production of strings. Depending on spin and flavor of excited strings, they get

converted into partons without any further interaction. If those strings/partons satisfy minimum distance conditions [$\leq \sqrt{(\sigma/\pi)}$, σ being cross section for partonic two-body scattering], then they undergo scattering, which is dealt by Zhang's Parton Cascade (ZPC) [145]. Once these partons stop interacting, nearest two partons form a mesons or that of three forms a baryons using a quark coalescence model. Cascade of resultant hadrons is dealt by A Relativistic Transport (ART) model [146, 147], which includes baryon-baryon, baryon-meson and meson-meson elastic and inelastic scatterings.

This version of AMPT, known as string melting has been used for the current study (version 26t5). There is another version referred as default AMPT model, where instead of quark coalescence, string fragmentation method is adopted.

4.2.3 The NLO model

The next-to-leading order, NLO-pQCD(MNR)[148] model used in the present work has been successfully used before to produce $c\bar{c}$ pair cross-sections in pp collisions at most of the available collider energies [149]. Consequently the model can be used to produce various heavy quark spectra and be utilised further to study the various hot and dense nuclear matter effects (as in Pb-Pb and $Au + Au$ collisions) and cold nuclear matter effects (as in p-Pb and d+Au collisions). In the present work, we have used the calculations to produce D-meson spectra for pp collisions at $\sqrt{s_{NN}} = 7$ TeV in order to check the consistencies of our calculations. In the next step, the calculations have been repeated for p-Pb at $\sqrt{s_{NN}} = 5.02$ TeV including shadowing effects as one of the initial cold nuclear effects [150, 151]. Let us now move to a brief description of the calculations:

The p_T differential spectrum of heavy quarks produced in pp collisions is

defined in general as [149, 152]:

$$\frac{d\sigma}{d^3 p_1 d^3 p_2} = \frac{d\sigma}{dy_1 dy_2 d^2 p_{T1} d^2 p_{T2}}, \quad (4.3)$$

where y_1 and y_2 are the rapidities of heavy quark and anti-quark and \mathbf{p}_{T_i} are their transverse momenta.

In the above

$$\begin{aligned} \frac{d\sigma}{dy_1 dy_2 d^2 p_T} = & 2x_a x_b p_T \sum_{ij} \left[f_i^{(a)}(x_a, Q^2) f_j^{(b)}(x_b, Q^2) \frac{d\hat{\sigma}_{ij}(\hat{s}, \hat{t}, \hat{u})}{d\hat{t}} \right. \\ & \left. + f_j^{(a)}(x_a, Q^2) f_i^{(b)}(x_b, Q^2) \frac{d\hat{\sigma}_{ij}(\hat{s}, \hat{u}, \hat{t})}{d\hat{t}} \right] / (1 + \delta_{ij}), \end{aligned} \quad (4.4)$$

where x_a and x_b are the fractions of the momenta carried by the partons from their interacting parent hadrons.

We have used CTEQ6.6 structure function [153] as obtained using LHAPDF library for pp system and added EPS09 [154] shadowing parameterization, to incorporate the initial nuclear effects on the parton densities for p-Pb system.

The differential cross-section for partonic interactions, $d\hat{\sigma}_{ij}/d\hat{t}$ is given by

$$\frac{d\hat{\sigma}_{ij}(\hat{s}, \hat{t}, \hat{u})}{d\hat{t}} = \frac{|M|^2}{16\pi\hat{s}^2}, \quad (4.5)$$

where $|M|^2$ (See Ref. [155]) is the invariant amplitude for various partonic sub-processes both for leading order (LO) and next-to-leading order (NLO) processes as follows:

The physical sub-processes included for the leading order, $\mathcal{O}(\alpha_s^2)$ production

of heavy quarks are:

$$\begin{aligned} g + g &\rightarrow Q + \bar{Q} \text{ and} \\ q + \bar{q} &\rightarrow Q + \bar{Q}. \end{aligned} \tag{4.6}$$

At next-to-leading order, $\mathcal{O}(\alpha_s^3)$ subprocesses included are as follows

$$\begin{aligned} g + g &\rightarrow Q + \bar{Q} + g, \\ q + \bar{q} &\rightarrow Q + \bar{Q} + g \text{ and} \\ g + q(\bar{q}) &\rightarrow Q + \bar{Q} + q(\bar{q}). \end{aligned} \tag{4.7}$$

Next we discuss rescattering processes within the nucleus. A parton may also undergo multiple hard scattering or a nucleon instead undergo multiple soft rescattering within the cold nucleus in cases of p+A or A+A collisions. This is commonly referred as Cronin effects [129, 156]. These rescatterings may lead to momentum broadening of the interacting parton and change the final heavy quark spectrum. This would also give rise to deviations of R_{pPb} from unity and is considered as another form of cold nuclear matter effect. We feel that its contribution apart from shadowing to the heavy meson spectra, when compared to pp collisions, can be discerned with the precise state-of-the-art experiments designed at LHC-CERN and RHIC-BNL. However, it was suggested that this effect may vanish at large transverse momentum region or high collider energies [157, 158, 159], but may be visible in the low and mid p_T region and is slowly emerging as a subject of contemporary interests in heavy ion collisions. The details of our implementations of the calculations are taken from Ref. [156, 160].

We can now discuss briefly about one of the mechanisms used from the above references. Starting with parton density functions, which can be defined

as

$$f_i^{(a)}(x_a, Q^2, k_T^2) = f_i^{(a)}(x_a, Q^2) \cdot g_{p/A}(k_T^2), \quad (4.8)$$

where $g_{p/A}(k_T^2) \propto \exp[-k_T^2/\pi \cdot \langle k_T^2 \rangle_{pp/pA}]$ and $\langle k_T^2 \rangle_{pA} = \langle k_T^2 \rangle_{pp} + \langle k_T^2 \rangle_A$

The effective transverse momentum kick, $\langle k_T^2 \rangle_{pA}$, obtained after a series of rescattering can be written as

$$\langle k_T^2 \rangle_A = \delta^2 \cdot n \cdot \ln \left(1 + \frac{p_T^2}{\delta^2/c} \right) \quad (4.9)$$

where the parameters δ^2/c , average squared momentum kick per scattering and $n = 2L_A/\lambda$, $L_A = 4R_A/3$, average number of rescattering, are used from [158, 160].

With the implementation of the above features, we can next fragment the charm momentum both from p+A and pp collisions into D-mesons, as D-mesons data are readily verifiable from experiments. Schematically, this can be shown as,

$$E \frac{d^3\sigma}{d^3p} = E_Q \frac{d^3\sigma}{d^3p_Q} \otimes D(Q \rightarrow H_M), \quad (4.10)$$

where the fragmentation of the heavy quark Q into the heavy-meson H_Q is described by the function $D(z)$. We have assumed that distribution of $D(z)$, w.r.t. z , where $z = p_D/p_c$, is used to calculate total D-mesons and is given by;

$$D_D^{(c)}(z) = \frac{n_D}{z[1 - 1/z - \epsilon_p/(1 - z)]^2}, \quad (4.11)$$

ϵ_p is the Peterson parameter $\simeq 0.12$ and is taken from [161]. The normalization condition satisfied by the fragmentation function is;

$$\int_0^1 dz D(z) = 1. \quad (4.12)$$

4.2.4 The FONLL model

As mentioned in the literatures, FONLL [162] has been used to calculate D -mesons spectra for LHC energies and earlier estimations have shown that FONLL calculation is able to explain the various heavy quark observables particularly transverse momentum spectra of heavy mesons with remarkable accuracies. The p_T spectra of heavy quarks produced in pp collisions as in Eq. 4.3 can be written as:

$$E_c \frac{d\sigma}{d^3 p_c dy_c} = \int d^3 p_c dy_{\bar{c}} \frac{d\sigma^{pp \rightarrow c\bar{c}}}{d^3 p_c d^3 p_{\bar{c}} dy_c dy_{\bar{c}}}, \quad (4.13)$$

where y_1 and y_2 are the rapidities of heavy quark and anti-quark and \mathbf{p}_{T_i} are their transverse momenta.

The above distribution is evaluated at the Fixed-Order plus Next-to-Leading-Logarithmic (FONLL) level, implemented in Ref [162]. In addition to the full fixed-order NLO result, the FONLL calculation also resums large perturbative terms proportional to $\alpha_s^n = \log^k(p_T/m_c)$ at all orders with next-to-leading-logarithmic (NLL) accuracy, where $m_c (= 1.5 \text{ GeV})$ is the heavy quark mass. Here too, we have used CTEQ6.6 parton structure function and EPS09 shadowing parametrization for our calculations.

The charm fragmentation function developed by Cacciari et al. [163] is used in the present work. This depends on the parameter r (See Ref. [164]) with the values of the parameters defined in the above references and fitted with $e+e-$ spectra data. Bottom fragmentation instead depends on the parameter α_B in a functional form given by Kartvelishvili et al. [165]. It is worth noting that using the Peterson et al. fragmentation function, gives a different result than that of fragmentation in FONLL [162].

4.3 Results and discussion

ALICE has recently published results on D-meson in pp [166] and p-Pb [167] collisions. Keeping a view of that, events are generated at $\sqrt{s} = 7$ TeV and $\sqrt{s_{NN}} = 5.02$ TeV using all the above models, i.e., HIJING, AMPT, NLO and FONLL. For pp system, the study is based on the mid rapidity region, i.e., $|y_{cms}| < 0.5$, where as for p-Pb it is in the rapidity range $-0.96 < y_{cms} < 0.04$. We have ensured that no D-meson is coming from B-meson.

Normalised pp yield was divided by $T_{pp} = 1.39 \times 10^{-5} \mu b^{-1}$ to obtain cross-section, while that for p-Pb, T_{pPb} is $9.8334 \times 10^{-05} \mu b^{-1}$ (See Ref. [168]).

From calculated cross-section, Nuclear modification factor (R_{pPb}) can be defined as follows:

$$R_{pPb} = \frac{\left(\frac{d\sigma}{dp_T}\right)_{pPb}}{A \times \left(\frac{d\sigma}{dp_T}\right)_{pp}}, \quad (4.14)$$

where A is the mass number of a nucleus (e.g., for Pb it is 208). Here we have used pp collisions as baseline at $\sqrt{s_{NN}} = 5.02$ TeV. We will discuss these various cold nuclear matter effects on our results in this section.

Figure 4.1 shows transverse momentum (p_T) differential production cross-section of D^0 , D^+ and D^{*+} mesons in pp collisions at $\sqrt{s} = 7$ TeV. Except for few low p_T bins, HIJING explains data within the uncertainties. Similar trend is followed by AMPT for D^0 and D^+ , but it poorly explains cross section of D^{*+} for $p_T < 10$ GeV/c. Apart from the direct production of D^0 and D^+ , we have incorporated contributions from other resonance decays. However, there is no decay contribution of other particles for the production of D^{*+} . From figure 4.1, we may say that both String Fragmentation and quark coalescence based simulation models (HIJING and AMPT, respectively) are able to explain

4 Production of D mesons in pp and p-Pb collisions at the LHC energies

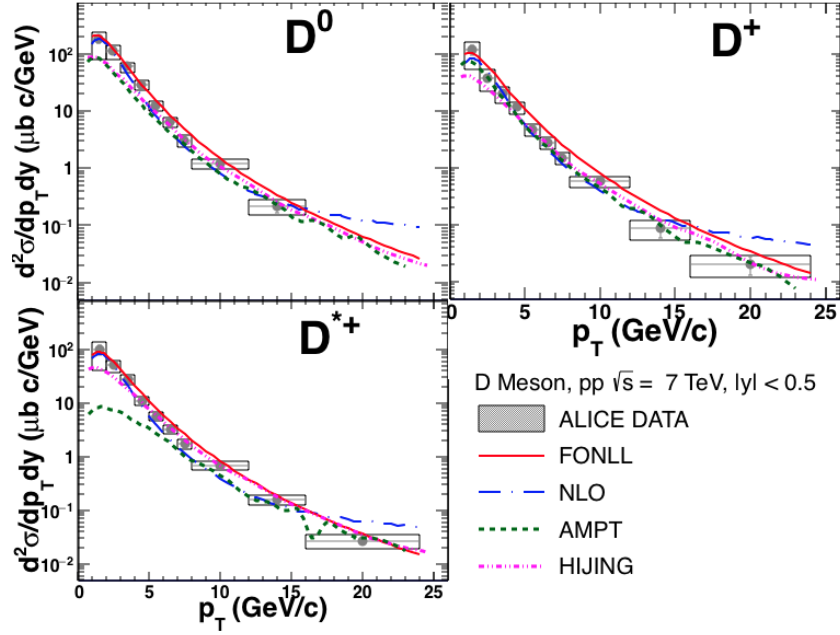


Figure 4.1: (Color online) p_T differential inclusive production cross-section of D -meson in pp collisions at $\sqrt{s} = 7$ TeV. Solid markers represent the ALICE data points [166]. Statistical errors are in bars while systematic errors are in boxes. Small dash-dotted magenta line, dashed green line, long dash-dotted blue line and solid red line represent HIJING, AMPT, NLO and FONLL results, respectively.

results from pp collision data. In addition to that, there might be some additional production mechanism is needed for AMPT especially at low p_T , which might add up to the D^{*+} cross-section. NLO results explain the data within error bars up to $p_T < 15$ GeV/c, but over estimates the results at higher p_T region. This may be due to the large NLO contributions adopted in the model formalism. Its shape is different from other simulations, which might be due to its dependence on renormalisation and fragmentation scale factors. FONLL at its next-to-leading calculations explains data very well for all p_T regions. Figure 4.2 is same as that of Figure 4.1, but for p-Pb system at $\sqrt{s_{NN}} = 5.02$ TeV. Here both HIJING and AMPT under-predict data over a wide range of p_T values. So we may think that cold nuclear shadowing effect of Pb as implemented in these models might have suppressed the yield to a large extent. AMPT under-predicts the data for all p_T region for D^0 and D^+ , but have same

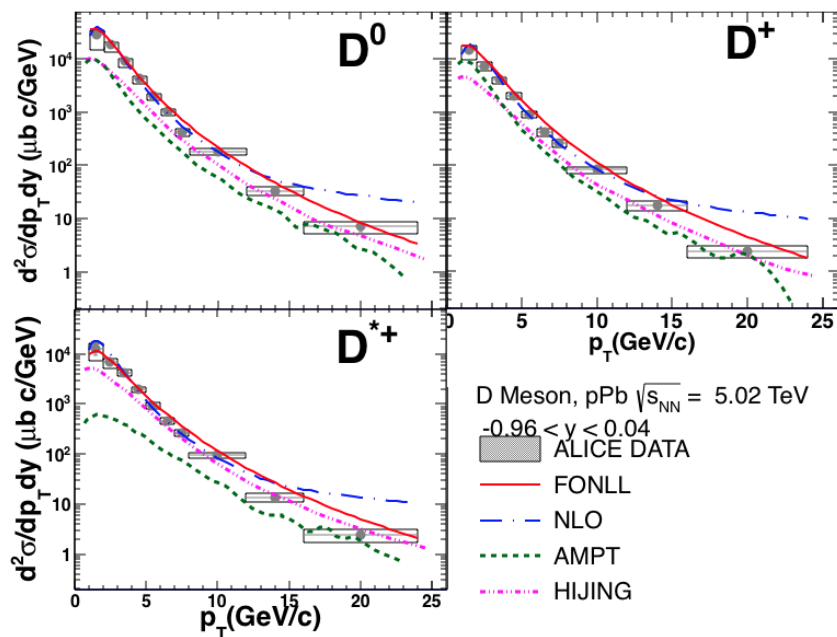


Figure 4.2: (Color online) p_T differential inclusive production cross-section of D mesons in p-Pb data at $\sqrt{s_{NN}} = 5.02$ TeV. Solid markers represent the ALICE data points[167]. Statistical errors are in bars while systematic errors are in boxes. Small dash-dotted magenta line, green dashed line, blue long dash-dotted line and red solid line represent HIJING, AMPT, NLO and FONLL results, respectively.

miss-match as that of pp for the case of D^{*0} . On contrary to HIJING, AMPT shows a smaller production cross-section for D^0 and D^+ in p-Pb system in its mechanism irrespective of nuclear shadowing effect. NLO in p-Pb likewise over estimates the cross-section for $p_T > 15$ GeV/c. FONLL explains data for all p_T to very good extent.

Figure 4.3 shows p_T -dependence of average R_{pPb} of D^0 , D^+ and D^{*+} mesons in p-Pb data at $\sqrt{s_{NN}} = 5.02$ TeV. The calculations from HIJING and AMPT are showing prominent cold nuclear matter (CNM) effects such as shadowing, EMC [72], and multi-parton scattering effects, for the entire p_T range. The results under-estimate the magnitude and trend of experimental data. The reasons behind such large CNM effects implemented in these calculations are being investigated and will be reported in our future publications. Besides having quark coalescence as hadron production mechanisms in AMPT than that of

4 Production of D mesons in pp and p-Pb collisions at the LHC energies

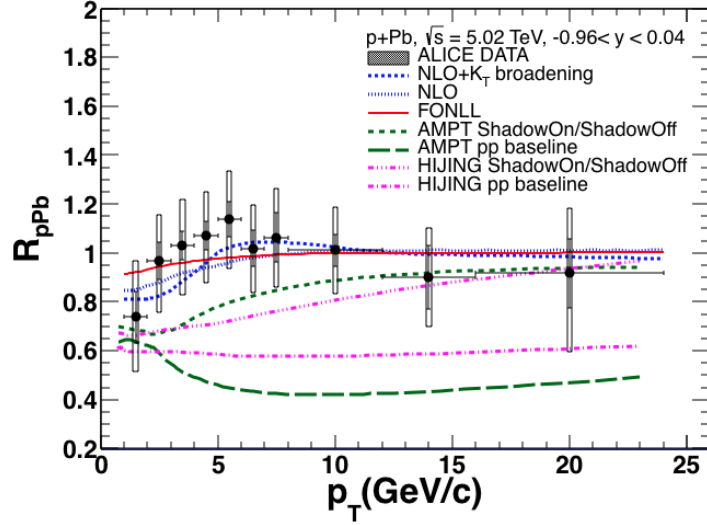


Figure 4.3: (Color online) Nuclear modification factor for D -meson in p-Pb $\sqrt{s_{NN}} = 5.02$ TeV. Solid markers represent the ALICE data points [167]. Statistical errors are in bars while systematic errors are in boxes. Magenta dotted line, green dashed line, red dash-dotted line, cyan solid line and blue solid line represent HIJING, AMPT, FONLL, NLO and NLO with Cronin K_T broadening results, respectively.

string fragmentation in HIJING, AMPT has additional partonic and hadronic transport parts which have both elastic and inelastic scatterings. This may also be the reason that R_{pPb} from AMPT is lower than that of HIJING. Next, in case of NLO, which has its nuclear shadowing feature, and in addition, it has momentum broadening effect (Cronin) due to re-scattering. Both the results with and without the momentum broadening effects are shown in the plot. The corresponding result with additional momentum broadening are closer to the trend of the data within its error bars. The result using NLO without broadening is closer to unity with suppression at the low p_T region due to shadowing and shows a difference in the shape of the curve from the one including the broadening effect. We may recall that a similar enhancement in trend of R_{dAu} for π_0 meson has also been reported for $d+Au$ collisions at $\sqrt{s_{NN}} = 200$ GeV by M. Gyulassy *et. al.*[160]. FONLL with shadowing features gives only very small shadowing effect for $p_T < 10$ GeV/c and remains close to unity.

Using AMPT and HIJING, to show the effects of shadowing exclusively on nuclear modification factor and also difference between pp and p-Pb (shadow-off) as baselines, we further calculated R_{pPb} as following:

$$R_{pPb} = \frac{\left(\frac{d\sigma}{dp_T}\right)_{pPb}^{ShadowOn}}{\left(\frac{d\sigma}{dp_T}\right)_{pPb}^{ShadowOff}} \quad (4.15)$$

Here we have turned on shadowing effect in numerator and turned it off in denominator (while other nuclear effects like multi-parton scattering etc. are present in both) in the same system, i.e. p-Pb at $\sqrt{s_{NN}} = 5.02$ TeV. As we can see from Figure 4.3 that taking p-Pb (shadow-off) as the baseline we see considerable nuclear effects such as shadowing particularly at the low and intermediate p_T regions, while any other effects due to Pb nucleus is cancelled both from numerator and denominator of the ratio. The results however differ much from calculations using pp baseline (AMPT and HIJING), suggesting greater effects of multi-parton scattering than shadowing etc. on the final D meson spectra.

4.4 Summary

We have carried out D-meson study in simulation models like HIJING and AMPT and compared our results with published ALICE data for pp collisions at $\sqrt{s} = 7$ TeV [166] and p-Pb collisions $\sqrt{s_{NN}} = 5.02$ TeV [167]. We have also compared with results from next-to-leading order calculations from FONLL and NLO.

Irrespective of shadowing effect included in both the models, AMPT shows lower value R_{pPb} compared to HIJING above $p_T = 2.5$ GeV/c. So we may conclude that magnitude of R_{pPb} in AMPT due to its additional partonic and hadronic transport parts differs from the same in HIJING. And for resonance

particle D^{*+} , additional mechanism is needed in AMPT to explain its production cross-section. More details in this direction will be reported in our future study.

Since R_{pPb} in all our calculations deviates from unity, thus there is initial cold nuclear matter effect playing an important role in all models. K_T broadening can predict the shape of the data. Also taking p-Pb (shadow off) as baseline in AMPT and HIJING highlights shadowing effect exclusively, other nuclear effects like multi-parton scattering phenomenon has considerable effects and can be viewed only with pp as baseline. To end with, further improvements are required in our parameter dependent models, to explain the experimental data properly. If results from high statistics data with improved uncertainty be available in future, we will improve these parameter dependent models to fit with data.

5 Phase transition in magnetized compact stars

5.1 Introduction

When the central density of neutron stars exceed the nuclear matter saturation density ($n_0 \sim 0.15 \text{ fm}^{-3}$), then the compact stars might contain different phases of matter. There are three possible phases: hadronic, quark and mixed between hadron and quark phases inside the neutron stars. Accordingly, there are three classes of compact stars. The first is purely consisted of hadronic matter is called neutron star (NS), the second is called quark stars (QS) of absolutely stable strange quark matter. The third one is called hybrid star (HS), where the matter has hadronic matter along with quark matter in the interior and the mixed matter exists in between quark and hadronic matter. The size of the core depends on the critical density of the quark-hadron phase transition and the equation of state (EOS) describing the different matters. The maximum masses of compact stars depend on the EOS of the constituent of matter.

The recent mass measurement of millisecond pulsar PSR J1614-2230 [169], pulsar J0348+0432 [170] and pulsar J1903+0327 [171] have put constraint on new mass limit to be $M = 1.97 \pm 0.04 M_\odot$, $M = 2.01 \pm 0.04 M_\odot$ and $M = 1.667 \pm 0.021 M_\odot$, for the compact stars, respectively. These measurements

have put a very strong restriction on the parameters of the EOS of matter under extreme conditions [172, 173] for the first time.

Also the new observations suggest that in some pulsars, the surface magnetic field can be as high as $10^{14} - 10^{15}$ G. It has been noticed that the observed giant flares, SGR 0526-66, SGR 1900+14 and SGR 1806-20 [174], are the manifestation of such strong surface magnetic field in those stars. Such stars are separately assigned as magnetars. If we assume flux conservation from a progenitor star, we can expect the central magnetic field of such stars are more than $10^{17} - 10^{18}$ G [175]. Such a huge strong fields are expected to affect the compact stars properties. It can modify either the metric describing the stars [176, 177] or it can modify the EOS of matter of the stars. The effect of strong magnetic field on EOS, both for nuclear matter [178, 179, 180, 181, 182] and quark matter [186, 185, 187, 183, 184] have been studied earlier and the significant changes in the gross structural properties of compact stars have been discussed in detail.

From the simple dimensional analysis and the several investigations of vibrating neutron stars, it is suggested that the period of fundamental mode would be of the order of milliseconds [188]. The value of period of oscillations depends of the constituents of matter and interaction between them, that is, the equation of state of the matter. The period of oscillation is different for hadronic matter to that of quark matter. Also it deviates from the either normal hadronic matter or quark matter significantly, when the matter is mixed with both hadron and quark matter in the presence of strong magnetic field. In the present calculation, we have calculated hadronic matter EOS using relativistic mean field theory, quark matter EOS using MIT bag model and then constructed mixed phase EOS by using Glendennings conjecture in presence

of strong magnetic field. Using all these EOS in different matter, we have calculated the maximum mass and other gross structural properties as well as the period of oscillation of NS, QS and HS.

5.2 Radial pulsation of non-rotating star

The equation for infinitesimal radial pulsation of a non-rotating star in general relativistic formalism was given by Chandrasekhar [189] and has the following form

$$X \frac{d^2 \xi}{dr^2} + Y \frac{d\xi}{dr} + Z\xi = \tilde{\sigma}^2 \xi. \quad (5.1)$$

Here $\xi(r)$ is the Lagrangian fluid displacement and $c\tilde{\sigma}$ is the characteristic eigenfrequency (c is the speed of light). The quantities X , Y and Z depend on the equilibrium profiles of the pressure p and density ρ of the star and are represented by:

$$X = \frac{-e^{-\lambda} e^\nu}{p + \rho c^2} \Gamma p, \quad (5.2)$$

$$Y = \frac{-e^\lambda e^\nu}{p + \rho c^2} \left\{ \Gamma p \left(\frac{1}{2} \frac{d\nu}{dr} + \frac{1}{2} \frac{d\lambda}{dr} + \frac{2}{r} \right) + p \frac{d\Gamma}{dr} + \Gamma \frac{dp}{dr} \right\}, \quad (5.3)$$

$$Z = \frac{-e^\lambda e^\nu}{p + \rho c^2} \left\{ \frac{4}{r} \frac{dp}{dr} - \frac{(dp/dr)^2}{p + \rho c^2} - A \right\} + \frac{8\pi G}{c^4} e^\nu p. \quad (5.4)$$

Γ is the adiabatic index defined as

$$\Gamma = \left(1 + \rho c^2 / p \right) \frac{dp}{d(\rho c^2)} \quad (5.5)$$

and

$$\begin{aligned}
 A = & \frac{d\lambda}{dr} \frac{\Gamma p}{r} + \frac{2p}{r} \frac{d\Gamma}{dr} + \frac{2\Gamma}{r} \frac{dp}{dr} - \frac{2\Gamma p}{r^2} - \frac{1}{4} \frac{d\nu}{dr} \left(\frac{d\lambda}{dr} \Gamma p + 2p \frac{d\Gamma}{dr} + 2\Gamma \frac{dp}{dr} - \frac{8\Gamma p}{r} \right) \\
 & - \frac{1}{2} \Gamma p \left(\frac{d\nu}{dr} \right)^2 - \frac{1}{2} \Gamma p \frac{d^2\nu}{dr^2}
 \end{aligned} \tag{5.6}$$

To solve the pulsation equation (5.1), the boundary conditions are

$$\xi(r=0) = 0, \tag{5.7}$$

$$\begin{aligned}
 \delta p(r=R) &= -\xi \frac{dp}{dr} - \Gamma p \frac{e^{\nu/2}}{r^2} \frac{\partial}{\partial r} \left(r^2 e^{-\nu/2} \xi \right) \Big|_{r=R} \\
 &= 0.
 \end{aligned} \tag{5.8}$$

It is important to note that ξ is finite when p vanishes at $r = R$. The pulsation Eq. 5.1 is a Sturm-Liouville eigenvalue equation for $\tilde{\sigma}^2$, subject to the boundary conditions Eq. 5.7 and 5.8. As a consequence the eigenvalues $\tilde{\sigma}^2$ are all real and form an infinite discrete sequence $\tilde{\sigma}_0^2 < \tilde{\sigma}_1^2 < \dots \tilde{\sigma}_n^2 < \dots$, with the corresponding eigenfunction $\xi_0(r), \xi_1(r), \dots, \xi_n(r)$, where $\xi_n(r)$ has n nodes. It immediately follows that if fundamental radial mode of a star is stable ($\tilde{\sigma}_0 > 0$), then all the radial modes are stable. We note that Eqs.(5.1-5.6) depend on the pressure and energy density profiles, as well as on the metric functions $\lambda(r), \nu(r)$ of the non-rotating star configuration. Those profiles are obtained by solving the Oppenheimer-Volkof equation of hydrostatic equilibrium [190].

$$\frac{dp}{dr} = -\frac{G(\rho + p/c^2)(m + 4\pi r^3 p/c^2)}{r^2(1 - 2Gm/rc^2)}, \tag{5.9}$$

$$\frac{dm}{dr} = 4\pi r^2 \rho, \quad (5.10)$$

$$\frac{dv}{dr} = \frac{2G(m + 4\pi r^3 p/c^2)}{r^2 c^2 (1 - 2Gm/rc^2)} \quad (5.11)$$

$$\lambda = -\ln(1 - 2Gm/rc^2). \quad (5.12)$$

Eqs (5.9 – 5.12) can be numerically integrated for a given equation of state $p(\rho)$ and given central density to obtain the radius R and mass $M = m(R)$ of the star. Therefore, the basic input is the EOS, $p = p(\rho)$ to solve the structure and pulsation equations. It has been noticed [191] that gross structure parameters such as mass, radius etc. of neutron stars are mainly dominated by the EOS at high densities, specifically around the composition of matter in the core. Since the oscillation features are governed by the structure profiles of neutron stars, it is expected to possess marked sensitivity on the high density EOS as well. We have employed the EOS of hadronic phase, quark phase and constructed mixed phase regions in presence as well as absence of magnetic field to calculate the period of oscillation $P (= 2\pi/c\tilde{\sigma})$ of NS, QS and HS, respectively.

5.3 Magnetic field in hadronic phase

Hadrons are the degrees of freedom for the EOS at normal nuclear density. Above the nuclear matter density, we consider strange degrees of hadrons as well. For the description of the hadronic phase, we use a non-linear version of the relativistic mean field (RMF) model with hyperons (TM1 parametrization) which is widely used to construct EOS for NS. In this model, the baryons interact with mean meson fields [193, 194, 195, 196, 197, 192]. The relativistic

model is given as below.

The Lagrangian density including nucleons, baryon octet and leptons is given by

$$\begin{aligned}
 \mathcal{L}_H = & \sum_b \bar{\psi}_b [\gamma_\mu (i\partial^\mu - g_{\omega b} \omega^\mu - \frac{1}{2} g_{\rho b} \vec{\tau} \cdot \vec{\rho}^\mu) \\
 & - (m_b - g_{\sigma b} \sigma)] \psi_b + \frac{1}{2} (\partial_\mu \sigma \partial^\mu \sigma - m_\sigma^2 \sigma^2) \\
 & - \frac{1}{4} \omega_{\mu\nu} \omega^{\mu\nu} + \frac{1}{2} m_\omega^2 \omega_\mu \omega^\mu - \frac{1}{4} \vec{\rho}_{\mu\nu} \cdot \vec{\rho}^{\mu\nu} \\
 & + \frac{1}{2} m_\rho^2 \vec{\rho}_\mu \cdot \vec{\rho}^\mu - \frac{1}{3} b m_n (g_\sigma \sigma)^3 - \frac{1}{4} c (g_\sigma \sigma)^4 + \frac{1}{4} d (\omega_\mu \omega^\mu)^2 \\
 & + \sum_L \bar{\psi}_L [i\gamma_\mu \partial^\mu - m_L] \psi_L.
 \end{aligned} \tag{5.13}$$

Leptons in \mathcal{L}_H are treated as non-interacting and baryons b are coupled to the scalar meson σ , the isoscalar-vector meson ω_μ and the isovector-vector meson ρ_μ . There are five constants in the model that are fitted to the bulk properties of nuclear matter at saturation point. This model is good enough to describe nuclear matter at the nuclear saturation point. However, for hyperonic matter the model does not reproduce the observed strong $\Lambda\Lambda$ attraction[198]. So, the interactions are not enough to take care hyperonic matter. Therefore, by adding two new meson fields with hidden strangeness can resolve this deficit at large extent. These are the iso-scalar scalar σ^* and the iso-vector vector ϕ fields which couple to hyperons only[197]. The effective baryon mass is given by

$$m_b^* = m_b - g_\sigma \sigma - g_{\sigma^*} \sigma^*. \tag{5.14}$$

For the chemical beta equilibrated matter the conditions is

$$\mu_i = b_i \mu_B + q_i \mu_e, \tag{5.15}$$

where b_i and q_i are the baryon number and charge (in terms of electron charge) of species i , respectively. μ_B is the baryon chemical potential and μ_e is the electron chemical potential. For charge neutrality, the condition is

$$\rho_c = \sum_i q_i n_i = 0, \quad (5.16)$$

where n_i is the number density of species i .

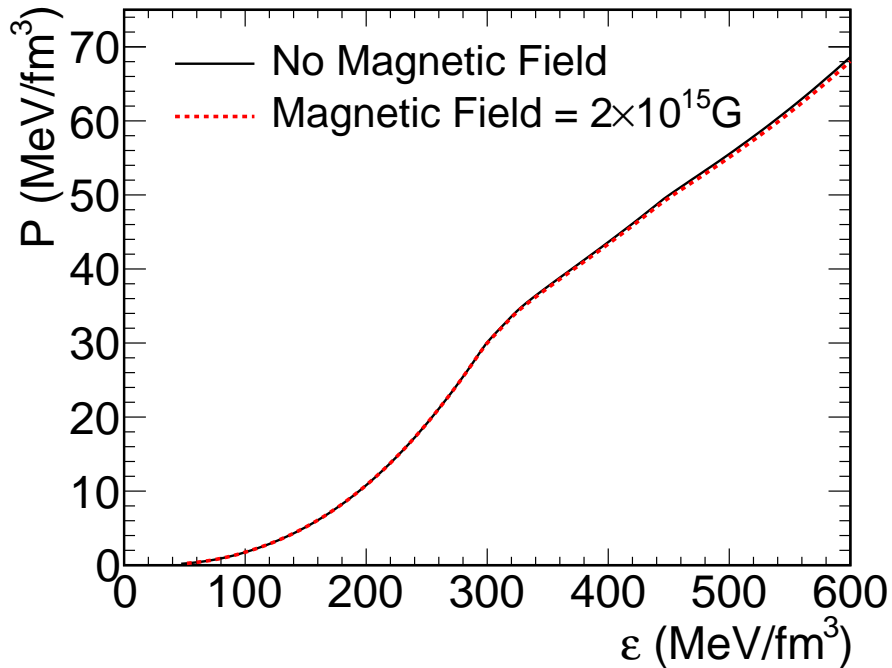


Figure 5.1: pressure against energy density for zero and non zero value of magnetic field. $B=0$ (solid line) and $B=2 \times 10^{15}G$ with $\alpha = 0.005$ (dotted line).

We have chosen the gauge for the magnetic field to be, $A^\mu \equiv (0, -yB, 0, 0)$, B being the magnitude of magnetic field. For this particular gauge choice we can write $\vec{B} = B\hat{z}$. Due to the magnetic field, the motion of the charged particles are Landau quantized in the perpendicular direction to the magnetic field. The momentum in the x - y plane is quantized and hence the energy of the n th Landau level is [199] given by

$$E_i = \sqrt{p_i^2 + m_i^2 + |q_i|B(2n + s + 1)}, \quad (5.17)$$

5 Phase transition in magnetized compact stars

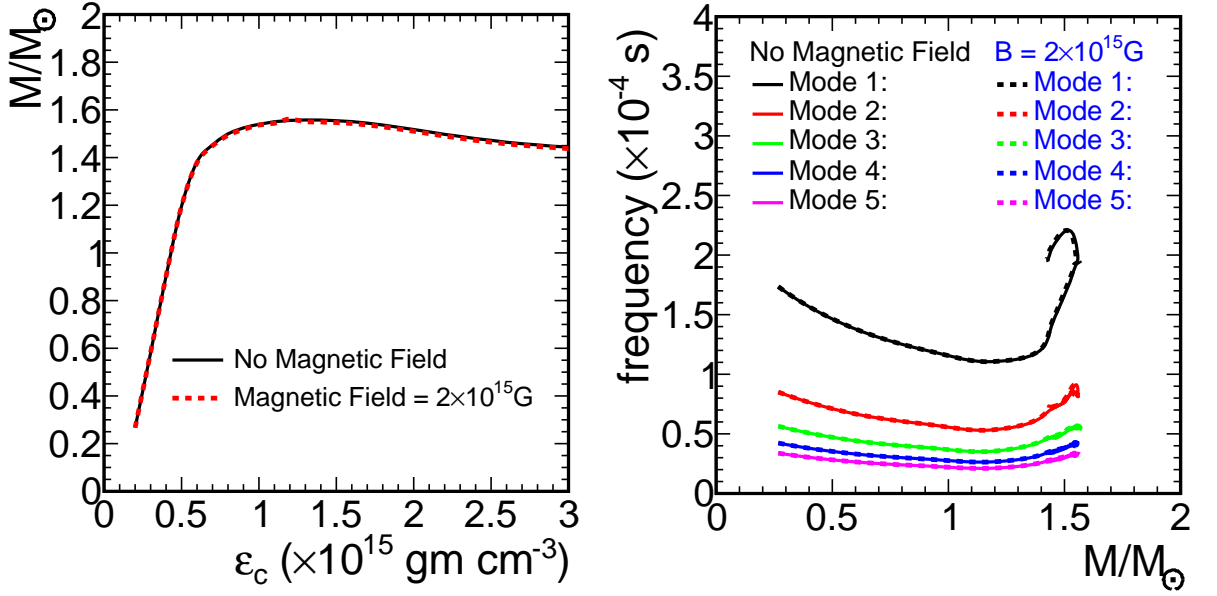


Figure 5.2: Top figure is the maximum gravitational mass against central energy density for both zero and non zero magnetic field. $B=0$ (solid line) and $B=2 \times 10^{15} \text{ G}$ (dotted line). Bottom figure is the period of oscillation in seconds against gravitational mass in solar mass for zero and non zero value of magnetic field. $B=0$ (solid line) and $B=2 \times 10^{15} \text{ G}$ with $\alpha = 0.005$ (dotted line) for fundamental mode (1) and higher harmonics (2-5).

where $n=0, 1, 2, \dots$, are the principal quantum numbers for allowed Landau levels, $s = \pm 1$ refers to spin up(+) and down(-) and p_i is the component of particle (species i) momentum along the field direction. Setting $2n + s + 1 = 2\tilde{\nu}$, where $\tilde{\nu} = 0, 1, 2, \dots$, we can rewrite the single particle energy eigenvalue in the following form

$$E_i = \sqrt{p_i^2 + m_i^2 + 2\tilde{\nu}|q_i|B} = \sqrt{p_i^2 + \tilde{m}_{i,\tilde{\nu}}^2} \quad (5.18)$$

where the $\tilde{\nu} = 0$ state is singly degenerate and m_b^* is the baryon mass.

The total energy density of the system can be written as[192]

$$\begin{aligned} \varepsilon = & \frac{1}{2}m_\omega^2\omega_0^2 + \frac{1}{2}m_\rho^2\rho_0^2 + \frac{1}{2}m_\sigma^2\sigma^2 + \frac{1}{2}m_{\sigma^*}^2\sigma^{*2} + \frac{1}{2}m_\phi^2\phi_0^2 + \frac{3}{4}d\omega_0^4 + U(\sigma) \\ & + \sum_b \varepsilon_b + \sum_l \varepsilon_l + \frac{B^2}{8\pi^2}, \end{aligned} \quad (5.19)$$

where the last term is the contribution from the magnetic field. The general expression for the pressure is given by

$$p = \sum_i \mu_i n_i - \varepsilon. \quad (5.20)$$

We have assumed that the parametrization of the magnetic field strength depends on the baryon number density. Therefore we have assumed a simple density dependence, as given by [179]

$$B(n_b/n_0) = B_s + B_0 \left\{ 1 - e^{-\alpha(n_b/n_0)^\gamma} \right\}, \quad (5.21)$$

where α and γ are two parameters determining the magnetic field profile with given B_s and B_0 , n_b being the baryon number density. The value of B mainly depends on B_0 , and is quite independent of B_s . Therefore, we have varied the field at the center, whereas surface field strength is taken to be $B_s = 10^{14}\text{G}$. We keep γ fixed at 2, and vary α to have the field variation. In the present calculation, we have assumed $\alpha = 0.005$. In the above parametrization, the magnetic field strength depends on the baryon number density. However, at each density the field is uniform and constant.

We have displayed the pressure versus energy density in Fig. 5.1, where the dashed line represents the EOS with magnetic field of strength $2 \times 10^{15}\text{G}$ with $\alpha = 0.005$ and the solid line represents the same in absence of magnetic field. We have noticed in this figure that the dashed line (with presence of magnetic field) is slightly below the solid line (with absence of magnetic field) at high energy density region. This implies that the EOS is softer in presence of magnetic field, but this effect is not very significant.

In Fig. 5.2, the left panel is for gravitational mass of NS against central energy density. The maximum mass is $1.55M_\odot$ at central density of 5 times the

nuclear saturation density in presence of magnetic field, whereas, the maximum mass is $1.56M_{\odot}$ for zero magnetic field at the same central energy density as that of with magnetic field. Though the change of maximum mass is not very much significant, but reduces in presence of magnetic field.

We have plotted the period of oscillation in seconds against gravitational mass in the unit of solar mass for zero and non zero value of magnetic field in the right panel of Fig. 5.2. Solid lines are for $B=0$ and dashed lines are for $B=2 \times 10^{15}\text{G}$ with $\alpha = 0.005$ and are representations for fundamental mode (1) and higher harmonics (2-5). The period of oscillation is 0.2 ms at the maximum gravitational mass limit for fundamental mode for both zero and non-zero magnetic fields. However, for higher harmonics, the period of oscillations are 0.08, 0.06, 0.04 and 0.03 ms, respectively, for both zero and non-zero magnetic fields at the maximum gravitational mass limit.

5.4 Magnetic field in quark phase

Considering the simple MIT bag model for the quark matter in presence of magnetic field, we have assumed that the quarks are non-interacting. The current masses of u and d quarks are extremely small, e.g., 5 and 10 MeV respectively, where as, for s-quarks the current quark mass has been taken to be 150 MeV.

The thermodynamic potential in presence of strong magnetic field $B (> B^{(c)}$, critical value) is given by [186, 185, 200, 201]

$$\Omega_i = -\frac{g_i|q_i|BT}{4\pi^2} \int dE_i \sum_{\tilde{\nu}} \frac{dp_i}{dE_i} \ln[1 + \exp(\mu_i - E_i)/T]. \quad (5.22)$$

For the zero temperature, the Fermi distribution is approximated by a step function. By interchanging the order of the summation over $\tilde{\nu}$ and integration

over E one gets,

$$\Omega_i = -\frac{2g_i|q_i|B}{4\pi^2} \sum_{\tilde{\nu}} \int_{\sqrt{m_i^2+2\tilde{\nu}|q_i|B}}^{\mu} dE_i \sqrt{E_i^2 - m_i^2 - 2\tilde{\nu}|q_i|B}. \quad (5.23)$$

The total energy density and pressure of the strange quark matter is given by [192]

$$\begin{aligned} \varepsilon &= \sum_i \Omega_i + B_G + \sum_i n_i \mu_i \\ p &= -\sum_i \Omega_i - B_G, \end{aligned} \quad (5.24)$$

where B_G is the bag constant.

The bag constant is parametrized in such a way that it attains a value B_∞ , asymptotically at very high densities. The experimental range of B_∞ is given in Ref.[202], and therefor, we have choosen the value $B_\infty = 130\text{MeV}/\text{fm}^3$. Following the same assumptions, we have then constructed a Gaussian parametrization of bag constant as given by [202],

$$B_G(n_b) = B_\infty + (B_g - B_\infty) \exp\left[-\beta\left(\frac{n_b}{n_0}\right)^2\right]. \quad (5.25)$$

The value B_∞ , is the lowest value B_G can attain at asymptotic high density in quark matter, and is fixed at $130\text{MeV}/\text{fm}^3$. The quoted value of bag pressure at the hadron and mixed phase intersection point is denoted by B_g in the equation. The value of B_G decreases with increase in density and attains $B_\infty = 130\text{MeV}/\text{fm}^3$ asymptotically, the rate of decrease of the bag pressure being governed by parameter β . In the present calculation we have taken $\beta = 2$.

We have displayed the energy density versus pressure in Fig.5.3, where the solid black and green lines represent the relation in absence of magnetic field with density dependent bag pressure $B_G = 170 \text{ MeV}/\text{fm}^3$ and $B_G = 160$

5 Phase transition in magnetized compact stars

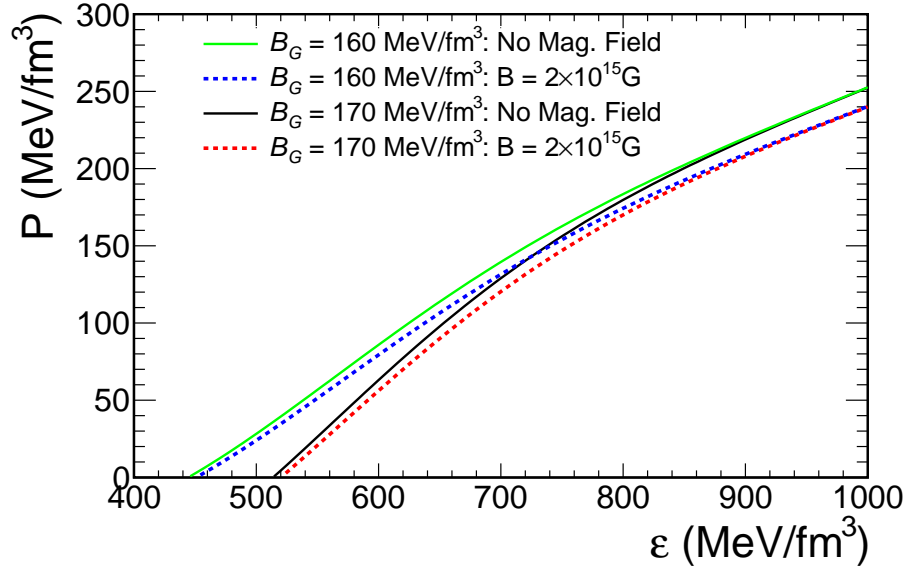


Figure 5.3: Figure shows the pressure against energy density for zero and non zero value of magnetic field. Solid green and black lines ($B=0$) and dashed blue and red lines ($B=2 \times 10^{15} \text{ G}$ with $\alpha = 0.005$) are for density dependent bag pressure $B_G = 160 \text{ MeV}/\text{fm}^3$ and $B_G = 170 \text{ MeV}/\text{fm}^3$, respectively, for fixed value of $\beta = 2$.

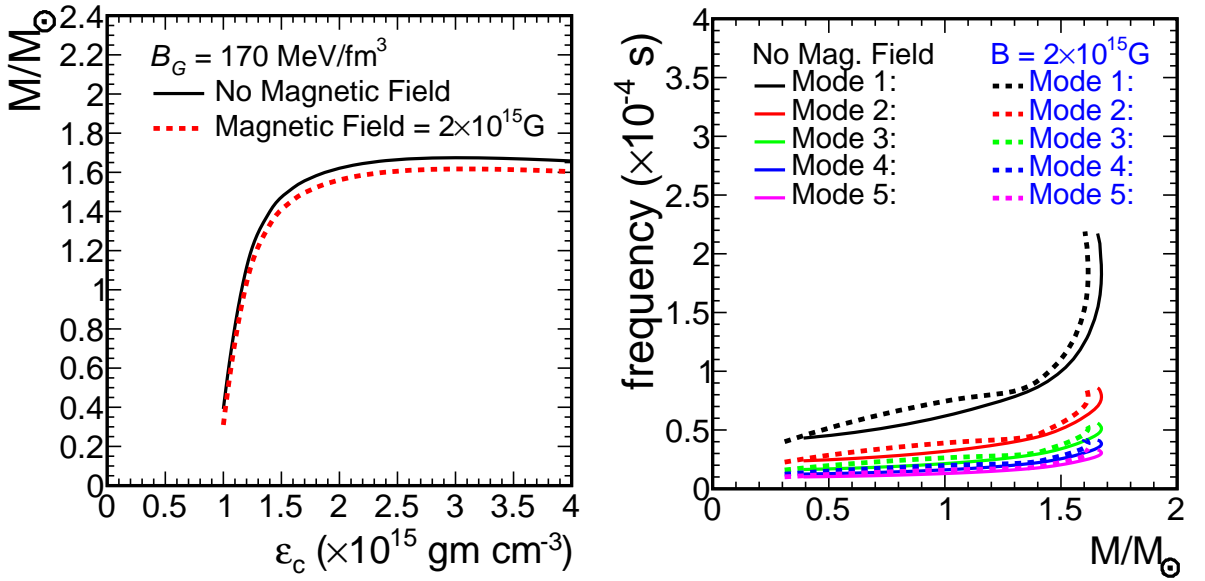


Figure 5.4: Left figure is the maximum gravitational mass against central energy density for both zero and non zero magnetic field for density dependent bag pressure $B_G = 170 \text{ MeV}/\text{fm}^3$. Solid lines and dashed lines are the representations in absence and presence of magnetic field, respectively. Right figure shows the period of oscillation in seconds against gravitational mass in solar mass unit for zero and non zero value of magnetic field ($B=2 \times 10^{15} \text{ G}$ with $\alpha = 0.005$), for density dependent bag pressure $B_G = 170 \text{ MeV}/\text{fm}^3$. Solid lines and dashed lines correspond to the absence and presence of magnetic field, respectively and are representing fundamental mode (1) and higher harmonics (2-5).

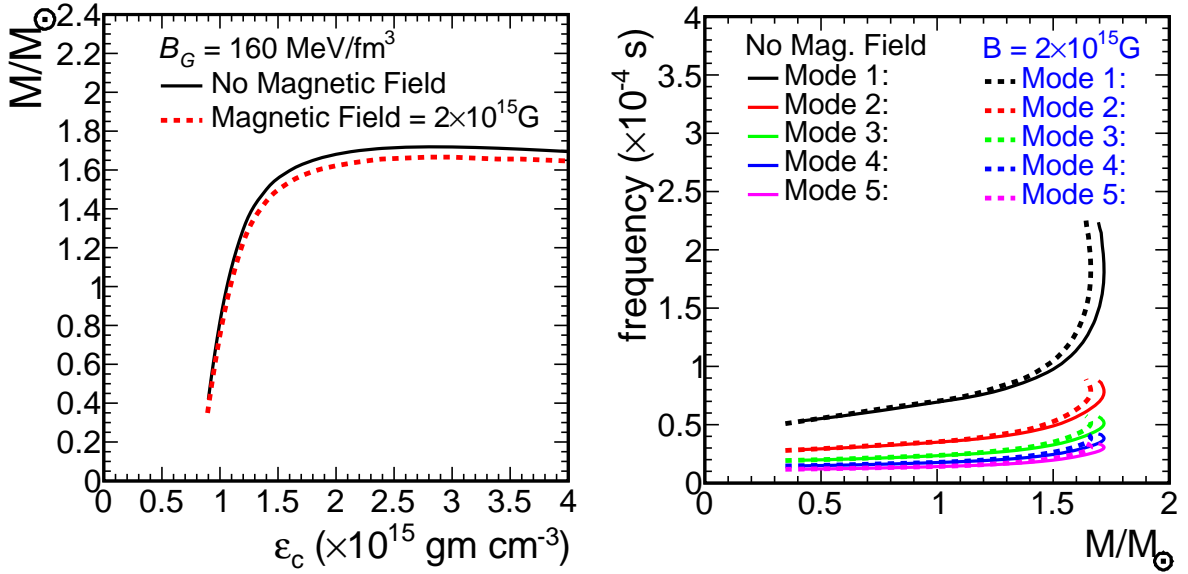


Figure 5.5: Same as figure 5.4, but for density dependent bag pressure $B_G = 160 \text{ MeV/fm}^3$.

MeV/fm^3 , respectively. However, the dashed red and blue lines represent the relation in presence of magnetic field of strength $2 \times 10^{15} \text{G}$ with $\alpha = 0.005$ for density dependent bag pressure $B_G = 170 \text{ MeV/fm}^3$ and $B_G = 160 \text{ MeV/fm}^3$, respectively. We have noticed that EOSs are softer in presence of magnetic field. The slope increases with decreasing density dependent bag pressure, e.g., for $B_G = 160 \text{ MeV/fm}^3$, the dashed blue and solid green lines are stiffer than the dashed red and solid black lines for density dependent bag pressure $B_G = 170 \text{ MeV/fm}^3$. We have noticed a very interesting nature that at very high energy density both the density dependent bag pressure $B_G = 160 \text{ MeV/fm}^3$ and 170 MeV/fm^3 are very similar to each other.

In Fig. 5.4, the left panel is for gravitational mass of QS against central energy density. In presence of magnetic field, the maximum mass is $1.62M_\odot$ at central density around 10 times the nuclear saturation density, whereas, the maximum mass is $1.67M_\odot$ for zero magnetic field at the almost similar central energy density as that of with magnetic field at $B_G = 170 \text{ MeV/fm}^3$. Though the change of maximum mass is not very much significant, but reduces in

presence of magnetic field.

We have plotted the period of oscillation in seconds against gravitational mass in the units of solar mass for zero and non zero value of magnetic field in the right panel of Fig.5.4 for density dependent bag pressure $B_G = 170 \text{ MeV/fm}^3$. Solid lines for $B=0$ and dashed lines for $B=2 \times 10^{15} \text{ G}$ with $\alpha = 0.005$ are shown for fundamental mode (1) and for higher harmonics (2-5) (from top to bottom). The fundamental period of oscillations are 0.17 ms and 0.18 ms at the maximum gravitational mass limit at zero and non-zero magnetic fields, respectively. However, for higher harmonics, the period of oscillations are 0.08, 0.05, 0.04 and 0.03 ms, respectively, for both zero and non-zero magnetic field at the maximum gravitational mass limit. The period of oscillation increases with inclusion of magnetic field in the EOS at $B_G = 170 \text{ MeV/fm}^3$.

In Fig. 5.5, the left panel is for gravitational mass of QS against central energy density same as Fig.5.4 but for density dependent bag pressure $B_G = 160 \text{ MeV/fm}^3$. In absence of magnetic field, the maximum mass is $1.72M_\odot$ at central density around 10 times the nuclear saturation density, whereas, the maximum mass is $1.66M_\odot$ for $2 \times 10^{15} \text{ G}$ magnetic field at similar central energy density as that of zero magnetic field. We have observed here that the change in the maximum mass is less by 3% in presence of the magnetic field.

We have plotted the period of oscillation in seconds against gravitational mass in units of solar mass in the right panel of Fig.5.5, same as Fig.5.4 but for $B_G = 160 \text{ MeV/fm}^3$. The fundamental period of oscillations are 0.22 ms and 0.18 ms at the maximum gravitational mass limit at zero and non-zero magnetic field, respectively. However, for higher harmonics, the period of oscillations are 0.1, 0.07, 0.05 and 0.04 ms, respectively, for non-zero magnetic field and 0.08, 0.05, 0.04 and 0.03, respectively, zero magnetic field at the maximum gravitational mass limit. The period of oscillations in presence of

magnetic field are higher as compared to those in zero magnetic field both for density dependent bag pressure $B_G = 160 \text{ MeV/fm}^3$ and $B_G = 170 \text{ MeV/fm}^3$. So the period of oscillation decreases with inclusion of magnetic field in the EOS at $B_G = 160 \text{ MeV/fm}^3$. This effect is opposite for $B_G = 170 \text{ MeV/fm}^3$.

5.5 Phase transition and mixed phase

Considering the given hadronic and quark EOS as discussed above, we have now performed the Glendenning construction [203] for the mixed phase, which determines the range of baryon density where both phases coexist. Here we have allowed both the hadron and quark phases to be separately charged, preserving the total charge neutrality as a whole in the mixed phase. Thus the matter has been treated as a two-component system, and have been parametrized by two chemical potentials, usually the pair (μ_e, μ_n) , i.e., electron and baryon chemical potentials. To maintain mechanical equilibrium, the pressure of the two phases have to be equal. Satisfying the chemical and beta equilibrium, the chemical potential of different species are connected to each other. The Gibbs condition for mechanical and chemical equilibrium at zero temperature between both phases is given by

$$p_{\text{HP}}(\mu_e, \mu_n) = p_{\text{QP}}(\mu_e, \mu_n) = p_{\text{MP}}. \quad (5.26)$$

This equation gives the equilibrium chemical potentials of the mixed phase corresponding to the intersection of the two phases. At lower densities below the mixed phase, the system is in the charge neutral hadronic phase, and for higher densities above the mixed phase the system is in the charge neutral quark phase. When the two surfaces intersect, we have calculated the charge

5 Phase transition in magnetized compact stars

densities ρ_c^{HP} and ρ_c^{QP} , separately, in the mixed phase. If χ is the volume fraction occupied by quark matter in the mixed phase, we have

$$\chi\rho_c^{\text{QP}} + (1 - \chi)\rho_c^{\text{HP}} = 0. \quad (5.27)$$

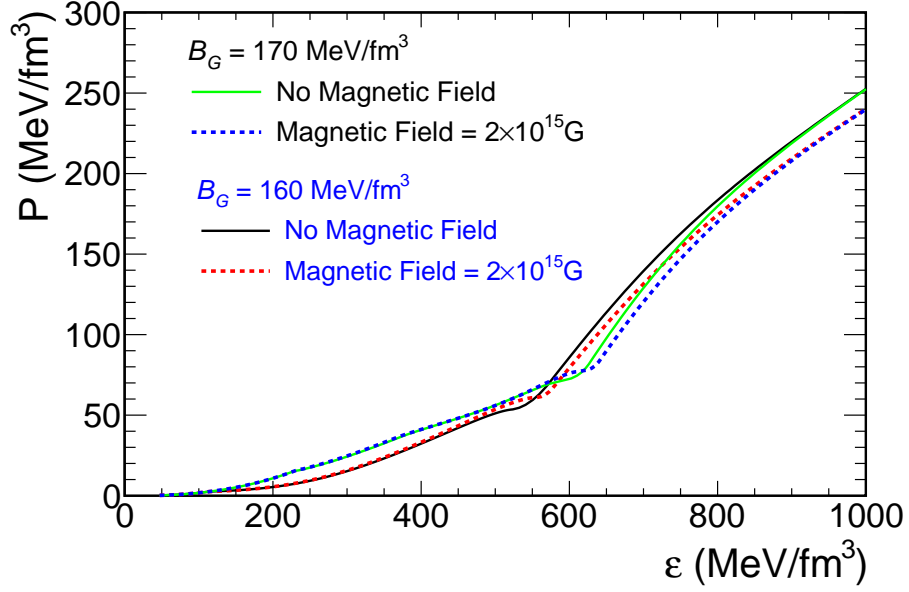


Figure 5.6: Figure shows pressure against energy density for zero (green and black solid lines are for $B_G = 170 \text{ MeV/fm}^3$ and $B_G = 160 \text{ MeV/fm}^3$, respectively) and non zero (blue and red dashed lines are for $B_G = 170 \text{ MeV/fm}^3$ and $B_G = 160 \text{ MeV/fm}^3$, respectively) values of magnetic field. $B = 2 \times 10^{15} \text{ G}$ with $\alpha = 0.005$.

Therefore the energy density ϵ_{MP} and the baryon density n_{MP} of the mixed phase can be obtained as

$$\epsilon_{\text{MP}} = \chi\epsilon_{\text{QP}} + (1 - \chi)\epsilon_{\text{HP}}, \quad (5.28)$$

$$n_{\text{MP}} = \chi n_{\text{QP}} + (1 - \chi)n_{\text{HP}}. \quad (5.29)$$

In the present calculation, we have assumed the first order phase transition from hadron matter to quark matter. The mixed phase has been constructed by adopting the Gibbs criteria based on the Glendenning conjecture. There is

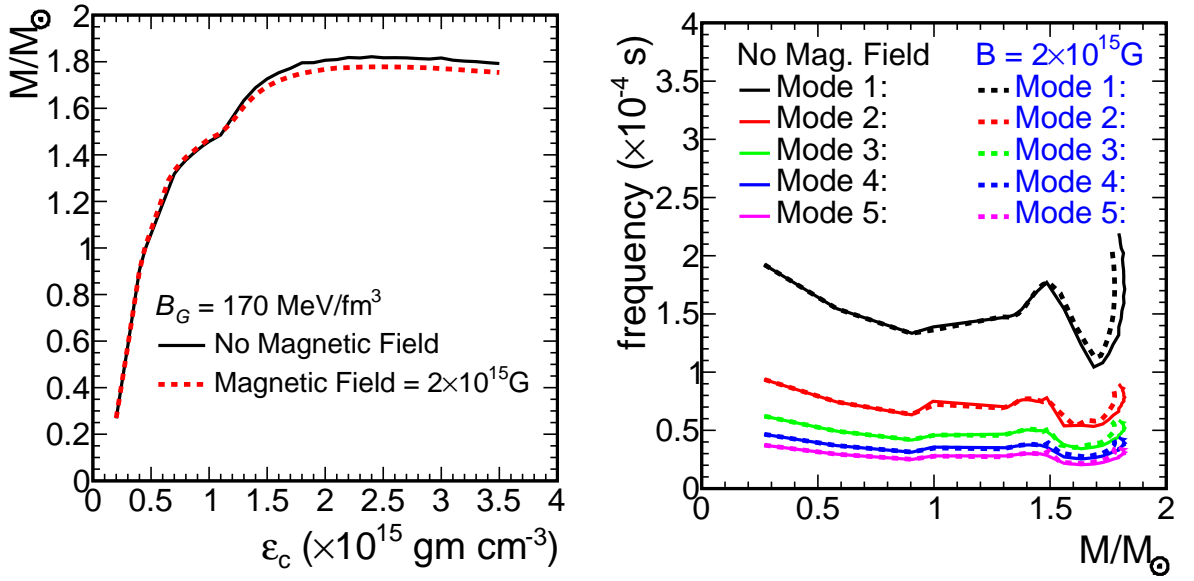


Figure 5.7: Left panel of figure shows gravitational mass in solar mass unit against central energy density for zero (solid line) and non zero (dashed line) value of magnetic field $B = 2 \times 10^{15} \text{ G}$ with $\alpha = 0.005$. Here the density dependent bag pressure B_G is 170 MeV/fm^3 . Right panel of figure shows period of oscillation in seconds against gravitational mass in solar mass unit for zero and non zero values of magnetic field. $B=0$ (solid lines) and $B = 2 \times 10^{15} \text{ G}$ (dashed lines) for fundamental mode (1) and higher harmonics (2-5) with density dependent bag pressure B_G is 170 MeV/fm^3 .

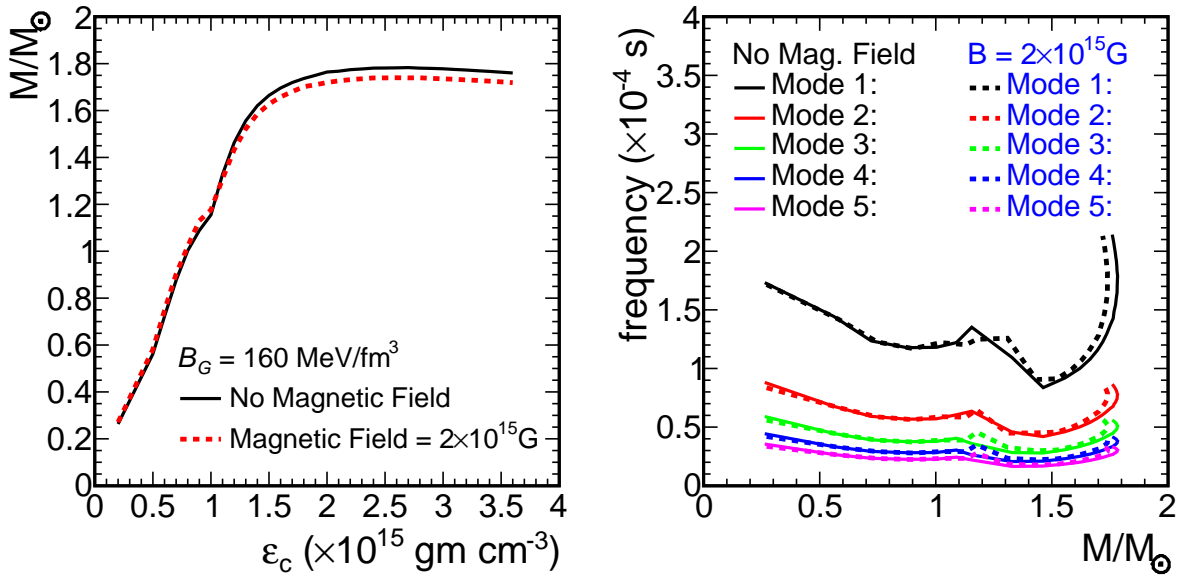


Figure 5.8: Same as Fig 5.7, but for the density dependent bag pressure B_G is 160 MeV/fm^3 .

an uncertainty in hadron-quark phase transition, when one consider the effects

of finite size[204]. For example, it has been shown that with the strong surface tensions, the phase transition looks the one under the Maxwell construction even if we impose the Gibbs condition. The detail discussion is given in Ref.[204]. In our calculation, we have not considered the finite size effects at the quark-hadron phase transition.

The magnetic field in HS changes the EOS of the matter. The single particle energy is Landau quantized, and thereby it changes all the other thermodynamic variable of the EOS, namely the number density, pressure and energy density.

We have displayed the pressure versus energy density in Fig.5.6, where the green and black solid lines represent the relation without the presence of magnetic field with density dependent bag pressure $B_G = 170 \text{ MeV/fm}^3$ and $B_G = 160 \text{ MeV/fm}^3$, respectively. The blue and red dashed lines represent for the magnetic field of strength $2 \times 10^{15} \text{ G}$ with $\alpha = 0.005$ with density dependent bag pressure $B_G = 170 \text{ MeV/fm}^3$ and $B_G = 160 \text{ MeV/fm}^3$, respectively. We have noticed that the EOSs shown by dashed lines (with presence of magnetic field) are softer than the EOSs shown by the solid lines (without magnetic field) at high energy density region in both the figures. From the Fig.5.6, we observed that the EOS is slightly stiffer for density dependent bag pressure $B_G = 160 \text{ MeV/fm}^3$.

In Fig. 5.7, the left panel is for gravitational mass of HS against central energy density. In presence of magnetic field, the maximum mass is $1.76M_\odot$ at central density which is more than 10 times the nuclear saturation density, whereas, the maximum mass is $1.82M_\odot$ for zero magnetic field at same central energy density for $B_G = 170 \text{ MeV/fm}^3$. The maximum mass reduces around 4% in presence of magnetic field.

We have plotted the period of oscillation in seconds against gravitational

mass in solar mass unit for zero and non zero value of magnetic field in the right panel of Fig.5.7 for density dependent bag pressure $B_G = 170 \text{ MeV/fm}^3$. Solid and dashed lines are for $B=0$ and $B=2 \times 10^{15} \text{ G}$ with $\alpha = 0.005$ and are shown for fundamental mode (1) and for higher harmonics (2-5), respectively. The fundamental period of oscillations are 0.16 ms and 0.17 ms at the maximum gravitational mass limit at zero and non-zero magnetic field, respectively. However, for higher harmonics, the period of oscillations are 0.07, 0.05, 0.04 and 0.03 ms, respectively, for both zero and non-zero magnetic fields at the maximum gravitational mass limit.

In Fig. 5.8, the left panel is for gravitational mass of HS against central energy density same as Fig.5.7, but for density dependent bag pressure $B_G = 160 \text{ MeV/fm}^3$. Without magnetic field, the maximum mass is $1.78M_\odot$ at central density more than ten times the nuclear saturation density, whereas, the maximum mass is $1.74M_\odot$ for $2 \times 10^{15} \text{ G}$ magnetic field at similar central energy density as that of zero magnetic field. We have observed here that the change in the maximum mass is insignificant in presence of the magnetic field.

We have plotted the period of oscillation in seconds against gravitational mass in solar mass unit in the right panel of Fig.5.8, same as Fig.5.7 but for $B_G = 160 \text{ MeV/fm}^3$. The fundamental period of oscillations are 0.22 ms and 0.18 ms at the maximum gravitational mass limit at zero and non-zero magnetic fields, respectively. However, for higher harmonics, the period of oscillations are 0.08, 0.05, 0.04 and 0.03 ms, respectively, for both zero and non-zero magnetic fields at the maximum gravitational mass limit. The period of oscillations are higher for density dependent bag pressure $B_G = 160 \text{ MeV/fm}^3$ than $B_G = 170 \text{ MeV/fm}^3$ for both zero and non-zero magnetic fields. Also, we have noticed that the period of oscillation is less in presence of magnetic field in EOS of HS as compare to that of zero magnetic field for $B_G = 160 \text{ MeV}$,

however, the period of oscillation is more in case of non-zero magnetic field for $B_G = 170 \text{ MeV/fm}^3$.

Here, we have observed one interesting point that at just before the maximum gravitational mass limit for both right panels of figures 5.7 and 5.8, there are dips in period of oscillations. These dips are due to the presence of end point of mixed phase region where quark phase dominates. These dips are basically the signature of quark phase, that means the mixed phase ends and quark phase starts.

5.6 Summary

In figures 5.1, 5.3 and 5.6, we have plotted pressure against energy density for hadron, quark and mixed phase regions. For quark and mixed phase regions, we have considered the density dependent bag pressure $B_G = 160$ and 170 MeV/fm^3 . In all cases, we have considered without magnetic field and with magnetic field of strength $2 \times 10^{15} G$ with $\alpha = 0.005$. It is clear that magnetic field softens the EOS for all cases as well as broadens the mixed phase region in hybrid phase in HS.

We have presented a calculation of the period of oscillations of neutron stars by using the radial pulsation equations of non rotating neutron stars, as given by Chandrasekhar [189] in the general relativistic formalism. To solve the radial pulsation equations, one needs a structure profile of non rotating neutron stars, obtained by employing realistic equations of state. The equations of state for hadron matter used here were derived from the relativistic formalisms with quark phases at higher densities. Then, the equations of state were constructed by using the Glendenning's condition for mechanical and chemical equilibrium as a function of baryon and electron density at the mixed phase,

comprising hadron as well as quark phases. In left panels of figures 5.2, 5.4, 5.5, 5.7 and 5.8, we have plotted Gravitational mass (in solar mass unit) against energy density for zero and non zero value of magnetic field. The maximum gravitational masses are more than $1.5M_{\odot}$ for NS, more than $1.6M_{\odot}$ for QS and more than $1.7M_{\odot}$ for HS for both magnetic and zero magnetic fields, respectively. These values are less than the recent measured values[169, 170], but close to the measured value as is given in Ref.[171]. According to recent observations[169, 170], one should have the NS more than $2M_{\odot}$, which is possible by considering the stiff EOS. However, considering phase transition from hadronic matter to quark matter leads to stiffening or softening the EOS for HS and hence the increase and decrease in maximum gravitational masses, respectively. In the present calculation, our main purpose is to show the signature of phase transition in the period of oscillations. In right panel of these figures, we have plotted the period of oscillations (in seconds) against gravitational mass for zero and non zero value of magnetic fields. We have noticed that there is a sudden dip in HS for both magnetic and non magnetic cases which corresponds to phase transition from hadron phase to quark phase. Dip is prominent for primary mode. These dips are present only HS not in NS and QS. Presence of magnetic field also slightly decrease the period of oscillation and shifting in higher mass region for $B_G = 160 \text{ MeV/fm}^3$ than the case of $B_G = 170 \text{ MeV/fm}^3$.

The main conclusion of our work is that the presence of magnetic field broadens the mixed phase region, the period of oscillation shows a dip around the point where mixed phase ends, in primary as well as in the higher modes, which is the distinct signature of quark matter onset in hybrid star. The presence of magnetic field decreases period of oscillation of fundamental as well as in higher modes at maximum mass limit for $B_G = 160 \text{ MeV/fm}^3$ than

5 Phase transition in magnetized compact stars

$B_G = 170$ MeV, but the effect is significant in fundamental mode.

6 Summary and Outlook

6.1 Summary

In this thesis we have investigated the hadronic scattering medium in p-Pb collisions through Λ^* baryonic resonance study and the cold nuclear medium effect through simulation study on D mesons at LHC energy. In the next part we have studied the QCD phase transition in magnetized compact stars. There we have shown how period of oscillation can be a signature of phase transition.

In the first part of the thesis, the Λ^* production in pp collisions at the mid-rapidity and in p-Pb collisions at the rapidity $-0.5 < y < 0$ has been studied through its hadronic decay channel, pK. The decayed particles are detected in the ALICE Time Projection Chamber (TPC) and Time Of Flight (TOF) detectors. We have obtained the transverse momentum (p_T) spectra of Λ^* in various multiplicity bins in p-Pb and minimum bias pp collisions. The p_T spectra of Λ^* are fitted with Boltzmann Gibbs Blast-Wave, Tsallis-Levy, m_T exponential and Boltzmann functions. Only Boltzmann Gibbs Blast-Wave and Tsallis-Levy functions have good fitting performance on all the spectra over whole p_T range. We have calculated yield and mean transverse momentum of Λ^* in pp and p-Pb collisions (in 4 multiplicity bins) at $\sqrt{s} = 7$ TeV and $\sqrt{s_{NN}} = 5.02$ TeV, respectively. These measurements may be used to tune event generators

inspired by pQCD. The $\langle p_T \rangle$ is studied as a function of mass of hadrons in pp collisions and it is found to increase with increase in mass. The $\langle p_T \rangle$ of Λ^* is found to follow the same trend like all the other hadrons in pp collisions. We have compared the yield of Λ^*/Λ ratio with K^{*0}/K and ϕ/K ratios in p-Pb collisions over all multiplicity bins. Due to short decay length of K^{*0} (~ 4 fm), it suffers a hadronic scattering medium, whereas the ϕ meson has a lifetime about 10 times more than that of K^{*0} shows no effect of the scattering medium on its yield. The Λ^* which decay length is in between above two particles (~ 12.6 fm) also shows no significant medium effect on its yield.

We have carried out D-meson production studies in simulation models with event generators like HIJING and AMPT and compared our results with published ALICE data in p-Pb collisions at $\sqrt{s} = 7$ TeV and p-Pb collisions at $\sqrt{s_{NN}} = 5.02$ TeV. We have also compared with the results from next-to-leading order calculations from FONLL and NLO. Here HIJING under-predicts data for $p_T < 7$ GeV/c in p-Pb collisions. So we may think that cold nuclear shadowing effect of Pb as implemented in this model might have suppressed the yield to a large extent. AMPT explains data for all p_T region for D^0 and D^+ within error bars. On contrary to HIJING, AMPT shows a larger production cross-section for D^0 and D^+ in p+Pb system in its mechanism irrespective of nuclear shadowing effect. NLO in p+Pb likewise over estimates the cross-section for $p_T > 15$ GeV/c. FONLL explains data for all p_T to very good extent. Since R_{pPb} in all our calculations deviates from unity, thus there is initial cold nuclear matter effect playing an important role in all models. K_T broadening can predict the shape of the data. The corresponding result predicts the trend of the data well within its error bars. A similar enhancement in trend of R_{dAu} for π_0 meson has also been reported for d+Au collisions at $\sqrt{s_{NN}}$

= 5.5 TeV by M. Gyulassy *et al.* (see Ref. [160]). FONLL gives very small shadowing effect for $p_T < 10$ GeV/c. To explain the experimental data, further improvements are needed in our parameter dependent models. If results from high statistics data with improved uncertainty will be available in future, we will improve these parameter dependent model to fit with data.

In the next part, we have studied the effects of such huge magnetic field on the matter inside the compact objects basically the equation of state (EOS) of the matters. Since matter inside the star are very dense both hadronic and quark matter, we have considered relativistic mean field theory in the hadronic matter and simple MIT bag model in the quark matter in the presence of strong magnetic field. We have calculated the phase transition between hadronic and quark phases, maximum mass and eigenfrequencies of radial pulsation of NS, HS and QS in the presence of such a huge magnetic field. The mixed phase is constructed by using Glendenning conjecture in between hadron and quark phases. We find in the presence of magnetic field, the EOS in both matter becomes soft. As a result, the maximum mass is reduced and the period of oscillation is changed significantly and there is a sudden dip in the period of oscillations in the HS, which signifies the transition from one to another matter.

6.2 Future Prospective

From 2015 LHC is producing data in pp collisions and in Pb-Pb collisions at $\sqrt{s_{NN}} = 5.02$ TeV. Since we have studied the Λ^* resonances in p-Pb collision at $\sqrt{s_{NN}} = 5.02$ TeV, the measurements from new pp collision data can be used to study the cold nuclear matter effect (R_{pPb}) in p-Pb collisions. From the study in Pb-Pb collisions at $\sqrt{s_{NN}} = 5.02$ TeV, one can measure the time span between chemical and kinetic freeze-outs and the effect of hot nuclear medium on Λ^*

6 *Summary and Outlook*

production.

References

- [1] David Griffiths, Introduction to Elementary Particles, Wiley-Vch.
- [2] S. L. Glashow, Nucl. Phys. 22, 579 (1961).
- [3] A. Salam and J.C. Ward, Phys. Lett. 13, 168 (1964).
- [4] S. Weinberg, Phys. Rev. Lett. 19, 1264 (1967).
- [5] H. Fritzsch, M. Gell-Mann, and H. Leutwyler, Phys. Lett. B47 (1973) 365-368.
- [6] D. J. Gross and F. Wilczek, Phys. Rev. Lett. 30 (1973) 1343-1346.
- [7] H. D. Politzer, Phys. Rev. Lett. 30 (1973) 1346-1349.
- [8] D. J. Gross and F. Wilczek, Phys. Rev. D8 (1973) 3633-3652.
- [9] CERN document server: cds.cern.ch.
- [10] P. W. Higgs, Phys. Lett. 12, 132 (1964); P. W. Higgs, Phys. Rev. Lett. 13, 508 (1964).
- [11] F. Englert and R. Brout, Phys. Rev. Lett. 13, 321 (1964).
- [12] G. Aad et al. (ATLAS Collaboration), Phys. Lett B 716, 1 (2012).
- [13] W. Adam et al. (CMS Collaboration), Phys. Lett B 716, 30 (2012).
- [14] S. Bethke, Prog. Part. Nucl. Phys. 58, (2007) 351-386.

References

- [15] K. Rajagopal and F. Wilczek, arXiv:hep-ph/0011333v2.
- [16] T. Kahara and K. Tuominen, Phys. Rev. D82, 114026, (2010)
- [17] <http://home.cern/about/accelerators/intersecting-storage-rings>
- [18] <http://ab-dep-op-sps.web.cern.ch/ab-dep-op-sps/>
- [19] <http://home.web.cern.ch/about/accelerators/super-proton-synchrotron>
- [20] <http://www.fnal.gov/pub/tevatron/tevatron-accelerator.html>
- [21] <http://www.bnl.gov/rhic/>
- [22] <http://home.cern/topics/large-hadron-collider>
- [23] J. W. Harris and B. Müller, Ann. Rev. Nucl. Part. Sci. 46 (1996) 71-107.
- [24] S. A. Bass, M. Gyulassy, H. Stöcker, and W. Greiner, J. Phys. G25 (1999) R1-R57.
- [25] T. Matsui and H. Satz, Phys. Lett. B178 (1986) 416.
- [26] J. Rafelski, Phys. Rept. 88 (1982) 331.
- [27] R. D. Pisarski, Phys. Lett. B110 (1982) 155.
- [28] J. Cleymans and K. Redlich, Phys. Rev. C60 (1999) 054908.
- [29] P. Braun-Munzinger, D. Magestro, K. Redlich, and J. Stachel, Phys. Lett. B518 (2001) 41-46.
- [30] N. Xu and M. Kaneta, Nucl. Phys. A698 (2002) 306-313.
- [31] J. Adams et al., STAR Collaboration, Nucl. Phys. A757 (2005) 102-183.

- [32] B. Abelev et al., ALICE Collaboration, Phys. Rev. Lett. 109, 252301 (2012).
- [33] O. Y. Barannikova, STAR Collaboration, nucl-ex/0403014.
- [34] J. Cleymans, B. Kämpfer, M. Kaneta, S. Wheaton, and N. Xu, Phys. Rev. C71 (2005) 054901
- [35] P. Braun-Munzinger, K. Redlich, and J. Stachel, nucl-th/0304013.
- [36] K. Adcox et al., PHENIX Collaboration, Nucl. Phys. A757 (2005) 184-283.
- [37] B. Abelev et al., ALICE Collaboration, Phys. Rev. Lett. 109, 252301 (2012).
- [38] J. Adams et al., STAR Collaboration, Nucl. Phys. A 757, 102 (2005).
- [39] S. Chatterjee, R. M. Godbole and S. Gupta, Phys. Lett. B 727, 554 (2013).
- [40] B. B. Back et al., Nucl. Phys. A757 (2005) 28-101.
- [41] I. Arsene et al., BRAHMS Collaboration, Nucl. Phys. A757 (2005) 1-27.
- [42] J. Adams et al., STAR Collaboration, Phys. Rev. Lett. 91 (2003) 172302.
- [43] K. Aamodt, et al., ALICE Collaboration, Phys. Lett. B 696, 30, (2011).
- [44] B. Abelev, et al., ALICE Collaboration, Phys. Rev. Lett. 110, 082302 (2013).
- [45] F. Antinori, et al., NA57 Collaboration, J. Phys. G 32, 427 (2006); F. Antinori, et al., (NA57 Collaboration), J. Phys. G 37, 045105 (2010).
- [46] B. I. Abelev, et al., (STAR Collaboration), Phys. Rev. C 77 044908, (2008).

References

- [47] B. Abelev et al., ALICE Collaboration, Phys. Lett. B 728, 216 (2013);
B. Abelev et al., ALICE Collaboration, Phys. Rev. Lett. 111, 222301 (2013).
- [48] J.Y. Ollitrault, Phys. Rev. D 46, 229 (1992).
- [49] S. Voloshin and Y. Zhang, Z. Phys. C 70, 665 (1996).
- [50] Abelev, B. et al., ALICE Collaboration, (2012) arXiv:1205.5761[nucl-ex]
- [51] Horowitz, W. and Gyulassy, M. Nucl.Phys. A872, 265-285 (2011).
- [52] Adams, J. et al., STAR Collaboration, Phys.Rev. C72, 014904 (2005).
- [53] Aamodt, K. et. al., ALICE Collaboration, Phys. Rev. Lett. 105, 252302 Dec (2010)
- [54] Aamodt, K. et. al., ALICE Collaboration, Phys. Rev. Lett. 107, 032301 Jul (2011)
- [55] R.J. Fries, Berndt Muller, C. Nonaka, and S.A. Bass, Phys. Rev. Lett., 90: 202303, 2003.
- [56] P. Koch, Berndt Muller, and Johann Rafelski, Phys. Rept., 142:167-262, 1986.
- [57] I. Kuznetsova and J. Rafelski, Eur. Phys. J. C, 51:113-133, 2007.
- [58] M. He, R. J. Fries and R. Rapp, Phys. Rev. Lett., 110(11):112301, 2013.
- [59] D. Park, Introduction to the Quantum Theory(McGraw-Hill Inc.), second edition, 1974.
- [60] L. Gaudichet, STAR collaboration, J.Phys. G30 (2004) S549-S555, nucl-ex/0307013.
- [61] L. Alvarez, Nobel Lecture, December 11, 1968.

- [62] K.A. Olive et al. (Particle Data Group), *Chin. Phys. C*, 38, 090001 (2014) and 2015.
- [63] E. Shuryak and G. Brown, *Nucl. Phys. A* 717, 322 (2003).
- [64] M. Bleicher and J. Aichelin, hep-ph/0201123.
- [65] R. Rapp and J. Wambach, *Adv. Nucl. Phys.* 25, 1 (2000).
- [66] R. Rapp, *Phys. Rev. C* 63, 054907 (2001).
- [67] J. Schaffner-Bielich, *Phys. Rev. Lett.* 84, 3261 (2000).
- [68] J. Letessier et al., *J. Phys. G* 27, 427 (2001).
- [69] G. Torrieri and J. Rafelski, *Phys. Lett. B* 509, 239 (2001).
- [70] W. Broniowski and W. Florkowski, *Phys. Rev. Lett.* 87, 272302 (2001).
- [71] A. Baltz and C. Dover, *Phys. Rev. C* 53, 362 (1996).
- [72] European Muon Collaboration, J. Ashman et al. , *Phys. Lett. B* 202, 603 (1988); European Muon Collaboration, M. Arneodo et al. , *ibid.* 211, 493 (1988).
- [73] M. Arneodo. Nuclear Effects in Structure Functions. *Phys. Rept.*, 240:301-393, 1994
- [74] J.W. Cronin, Henry J. Frisch, M.J. Shochet, J.P. Boymond, R. Mermod, et al., *Phys. Rev. D*, 11:3105, 1975.
- [75] O. S. Broning et al., LHC Design Report, (2004).
- [76] L. Evans (ed.), P. Bryant (ed.), *JINST* 3, S08001 (2008).
- [77] <https://cds.cern.ch/record/941318/files/p361.pdf>.
- [78] <http://home.cern/about/accelerators/proton-synchrotron>
- [79] <http://home.cern/about/experiments/atlas>.

References

- [80] <http://home.cern/about/experiments/cms>.
- [81] <http://home.cern/about/experiments/alice>.
- [82] <http://home.cern/about/experiments/lhcb>.
- [83] <http://te-dep-epc-oms.web.cern.ch/te-dep-epc-oms/general-fr/pagesources/Cern-Accelerator-Complex.jpg>.
- [84] CERN, Report on the 18 september incident at the LHC, (2008).
- [85] M. Lamont, Comparison of integrated luminosities, Chamonix (2010).
- [86] J. M. Jowett et. al., First run of the LHC as a heavy ion collider, CERN, (2011).
- [87] ALICE Collaboration, <http://aliceinfo.cern.ch/>.
- [88] K. Aamodt et al. (ALICE Collaboration), JINST 3, S08002 (2008).
- [89] Aamodt, K. , ALICE Collaboration. Journal of Instrumentation, 3(08):S08002, 2008.
- [90] LHCb Technical Proposal, CERN/LHCC 98-4 (1998).
- [91] ALICE Inner Tracking System (ITS): Technical Design Report, CERN-LHCC- 99-012, <http://edms.cern.ch/file/398932/1>.
- [92] ALICE Time Projection Chamber: Technical Design Report, CERN-LHCC- 2000-001, <http://cdsweb.cern.ch/record/451098>.
- [93] ALICE Transition Radiation Detector: Technical Design Report, CERN-LHCC-2001-021 ; LYCEN-2001-97, <https://cds.cern.ch/record/519145>.
- [94] ALICE forward detectors: FMD, T0 and V0: Technical Design Report, CERN- LHCC-2004-025, <http://cdsweb.cern.ch/record/781854>.

- [95] ALICE Zero-Degree Calorimeter: Technical Design Report, CERN-LHCC-99-005, <https://cds.cern.ch/record/381433>.
- [96] ALICE dimuon forward spectrometer : Technical Design Report, CERN-LHCC-99-022, <https://cds.cern.ch/record/401974>.
- [97] ALICE Photon Multiplicity Detector (PMD): Technical Design Report, CERN- LHCC-99-032, <http://cdsweb.cern.ch/record/451099>.
- [98] ALICE Technical Design Report on Photon Multiplicity Detector, Addendum-1, CERN/LHCC 2003-038 (2003).
- [99] F. Bergsma et al., CERN ALICE DAQ Group, ALICE DAQ and ECS users guide, ALICE Internal Note ALICE-INT-2005-015, <http://cdsweb.cern.ch/record/960457>.
- [100] ALICE Collaboration, ALICE Technical Design Report of the Trigger, Data Acquisition, High-Level Trigger, Control System, CERN/LHCC 2003/062 (2004), <https://edms.cern.ch/document/456354/2>.
- [101] https://twiki.cern.ch/twiki/bin/viewauth/ALICE/PWG1EvSelDocumentation#Custom_trigger_classes.
- [102] R. E. Kalman, Trans ASME, J. Bas. Eng. 82 D, (1960).
- [103] B. Alessandro et al. (ALICE Collaboration), J. Phys. G 32, 1295 (2006).
- [104] https://alimonitor.cern.ch/job_details.jsp.
- [105] B. Abelev et al. (ALICE Collaboration), Phys. Rev. C 88, 044909 (2013).
- [106] R. Barlow, Systematic Errors: facts and fictions, arXiv:hep-ex/0207026.
- [107] C. Tsallis, J. Stat. Phys. 52, 479 (1988).
- [108] E. Schnedermann, J. Sollfrank and U.W. Heinz, Phys. Rev. C 48, 2462 (1993).

References

- [109] Massimo Venaruzzo for the ALICE Collaboration, Nuclear Physics B, 234 (2013) 317-320.
- [110] B. I. Abelev et al. (STAR Collaboration), Phys. Rev. Lett. 97, (2006) 132301.
- [111] Milano, Leonardo for the collaboration, J.Phys.Conf.Ser. 316 (2011) 012019.
- [112] Becattini et al., J. Phys. G: Nucl. Part. Phys. 38, 2011, 025002.
- [113] J. Adam, et. al., (ALICE Collaboration), Eur. Phys. J. C (2016) 76: 245.
- [114] B. Abelev et al., (ALICE Collaboration), Eur. Phys. J. C72 (2012) 2183.
- [115] B. Abelev et al., (ALICE Collaboration), Phys. Rev. C91 no. 2, (2015) 024609.
- [116] <https://aliceinfo.cern.ch/Notes/node/409>.
- [117] J. C. Collins and M. J. Perry, Phys. Rev. Lett. **34**, 1353 (1975);
L. D. McLerran and B. Svetitsky, Phys. Lett. **B 98**, 195 (1981).
- [118] K. Kajantie, C. Montonen and C. Pietarinen, Zeit. Phys. **C 9**, 253 (1981); R. Hagedorn and J. Rafelski, Phys. Lett. **B 97**, 180 (1980).
- [119] J. W. Harris and B. Müller, Ann. Rev. Nucl. Part. Sci. **41**, 96 (1996);
B. Müller, Rep. Prog. Phys. **58**, 611 (1998).
- [120] S. A. Bass, M. Gyulassy, H. Stöcker and W. Greiner, J. Phys. **G: Nucl. Part. Phys.** **25**, R1 (1999).
- [121] <http://www.star.bnl.gov/>
- [122] <http://home.cern/about/experiments/alice>
- [123] <http://www.fair-center.eu/for-users/experiments/cbm.html>

- [124] A. Drees, Nucl. Phys. **A 698**, 331 (2002); E. Shuryak, Nucl. Phys. **A 750**, 64 (2005); S. Jeon and G. D. Moore, Phys. Rev. **C 71**, 034901 (2005).
- [125] X-N. Wang, Nucl. Phys. **A 750**, 98 (2005); A. K. Chaudhuri, Phys. Lett. **B 659**, 531 (2008); David d'Enterria and B. Betz, Lect. Notes Phys. **785**, 285 (2010).
- [126] A. Adare et al. (PHENIX Collaboration), Phys. Rev. Lett. **98**, 172301 (2007); B. I. Abelev et al. Phys. Rev. Lett. **98**, 192301 (2007); B. Abelev et al (ALICE Collaboration), arXiv:1203.2160v1[nucl-ex]2012.
- [127] M G Wysocki (PHENIX collaboration) Nucl Phys A 905-905, 67c-74c (2013) M Sarsaur (PHENIX collaboration) Nucl Phys Proc 276-278, 125-128 (2016)
- [128] K. J. Eskola, V. J. Kolhinen and C. A. Salgado, Eur. Phys. J. **C 9**, 61 (1999); K. J. Eskola, V. J. Kolhinen, P. V. Ruuskanen and C. A. Salgado, Nucl. Phys. **C 661**, 645 (1999).
- [129] J. W. Cronin, H. J. Frisch, M. J. Shochet, J. P. Boymond, R. Mermoud, P. A. Piroue and R. L. Sumner, Phys. Rev. **D 11**, 3105 (1975).
- [130] A. Adare et al. (PHENIX Collaboration), Phys. Rev. Lett. **98**, 172301 (2007).
- [131] E. Eichten, I. Hinchliffe, K. D. Lane, and C. Quigg, Rev. Mod. Phys. **56**, 579 (1984); Z. W. Lin, and M. Gyulassy, Phys. Rev. **C 51**, 2177 (1995); M. Younus and D. K. Srivastava, J. Phys. G: Nucl. Part. Phys. **37**, 115006 (2010).
- A Adare et al, (PHENIX Collabodation) Phys Rev Lett 109, 242301 (2012)

References

- [132] Grazia Luparello (for the ALICE Collaboration), *Journal of Physics: Conference Series*, **509**, 012101 (2014); Chitrasen Jena, for the ALICE Collaboration, *Journal of Physics: Conference Series*, **535**, 012027 (2014).
- [133] H. Fujii and K. Watanabe, arXiv:1308.1258, (2013).
- [134] X N Wang, M Gyulassy, *Phys. Rev. D*, 44, 3501 (1991).
- [135] B. Andersson, G. Gustafson, and B. Nilsson-Almqvist, *Nucl. Phys. B* 281, 289 (1987); B. Nilsson-Almqvist and E. Stenlund, *Comp. Phys. Commun.* 43, 387 (1987).
- [136] A. Capella, U. Sukhatme, and J. Tran Thanh Van, *Z. Phys. C* 3, 329 (1980); J. Ranft, *Phys. Rev. D* 37, 1842 (1988); *Phys. Lett.B* 188, 379 (1987).
- [137] T. Sjostrand and M. van Zijl, *Phys. Rev. D* 36, 2019 (1987); T. Sjostrand, *Comput. Phys. Commun.* 39, 347 (1986); T. Sjostrand and M. Bengtsson, *ibid.* 43, 367 (1987)
- [138] C. W. DeJager, H. DeVries, and C. DeVries, *At. Data Nucl. Data Tables* 14, 479 (1974)
- [139] M. Gyulassy, in *Proceedings of Eighth Balaton Conference on nuclear Physics*, edited by Z. Fodor (KFKI, Budapest, 1987); CERN Report No. CERN-TH-4794/87, 1987.
- [140] E. Eichten, I. Hinchliffe, K. Lane, and C. Quigg, *Rev. Mod. Phys.* 56, 579 (1984).
- [141] D. W. Duke and J. F. Owens, *Phys. Rev. D* 30, 50 (1984).
- [142] A. H. Mueller and J. Qiu, *Nucl. Phys. B* 268, 427 (1986); J. Qiu, *ibid.* B291, 746 (1987).
- [143] L. L. Frankfurt and M. I. Strikman, *Phys. Rep.* 160, 235 (1988).

- [144] Zi-Wei Lin, Che Ming Ko, Bao-An Li and Bin Zhang, *Subrata Pal Phys. Rev. C* **72**, 064901 (2005)
- [145] B. Zhang, *Comput. Phys. Commun.* **109**, 193 (1998).
- [146] B. A. Li, A. T. Sustich, B. Zhang and C. M. Ko, *Int. J. Mod. Phys. E* **10**, 267 (2001)
- [147] B. A. Li and C. M. Ko, *Phys. Rev. C* **52**, 2037 (1995)
- [148] M. L. Mangano, P. Nason and G. Ridolfi, *Nucl. Phys. B* **373**, 295 (1992); S. Frixione, M. L. Mangano, P. Nason and G. Ridolfi, *Adv. Ser. Direct. High Energy Phys.* **15**, 609 (1998).
- [149] U. Jamil and D. K. Srivastava, *J. Phys. G* **37**, 085106 (2010).
- [150] K. J. Eskola, H. Honkanen, V. J. Kolhinen and C. A. Salgado, "Global DGLAP fit analyses of the npdf: Eks98 and hkm," hep-ph/0302170 (1999); J. QIU, *Nucl. Phys. B* **291**, 746 (1987).
- [151] R. Vogt, "Cold Nuclear Matter Effects on Open and Hidden Heavy Flavor Production at the LHC", arXiv:1508.01286 [hep-ph].
- [152] M. Younus, U. Jamil and D. K. Srivastava, *J. Phys. G* **39**, 025001 (2012).
- [153] P. M. Nadolsky, H.-L. Lai, Q.-H. Cao, J. Huston, J. Pumplin, D. Stump, W.-Ki. Tung, C.-P. Yuan, *Phys. Rev. D* **78**, 013004 (2008).
- [154] K. J. Eskola, H. Paukkunen and C. A. Salgado, *JHEP* **0904**, 065 (2009).
- [155] B. L. Combridge *Nucl. Phys. B* **151**, 429 (1979).
- [156] A. Accardi, "Cronin Effect In Proton-Nucleus Collisions:A Survey Of Theoretical Models", hep-ph/0212148 (2003); X.-N. Wang, *Phys. Rev. C* **61**, 064910 (2000).
- [157] A. Accardi, M. Gyulassy, *Phys. Lett. B* **586**, 244 (2004).

References

- [158] R. Sharma, I. Vitev, and B.-W. Zhang, Phys. Rev. **C 80**, 054902 (2009).
- [159] G. G. Barnafoldi, P. Levai, G. Fai, G. Papp and B. A. Cole, Int. J. Mod. Phys. E **16**, 1923 (2007)
- [160] I. Vitev, and M. Gyulassy, Phys. Rev. Lett. **89**, No. 25, 252301 (2002); I. Vitev, Phys. Lett. B **562**, 36 (2003).
- [161] C. Peterson, D. Schlatter, I. Schmitt, and P. Zerwas, Phys. Rev. **D 27**, 105 (1983).
- [162] M. Cacciari, M. Greco and P. Nason, JHEP **9805**, 007 (1998); M. Cacciari, PoS HEP **2005**, 137 (2006) [hep-ph/0512251].
- [163] M. Cacciari and P. Nason, JHEP **0309**, 006 (2003).
- [164] E. Braaten, K. Cheung, S. Fleming, and T. C. Yuan, Phys. Rev. **D 51**, 4819 (1995) [arXiv:hep-ph/9409316].
- [165] V. G. Kartvelishvili, A. K. Likhoded, and V. A. Petrov, Phys. Lett. **B 78**, 615 (1978).
- [166] B. Abelev et al. (ALICE Collaboration), JHEP01 **128** (2012)
- [167] B. Abelev et al. (ALICE Collaboration) Phys. Rev. Lett. **113**, 232301 (2014)
- [168] M. Mangano, H. Satz and U. Wiedermann, DOI 10.5170/CERN-2004-009, <http://cds.cern.ch/record/815037>
- [169] P. Demorest, T. Pennucci, S. Ransom, M. Roberts and J. Hessels, Nature **467** 1081 (2010).
- [170] J. Antoniadis, P. C. C. Freire, N. Wex, T. M. Tauris, R. S. Lynch, M. H. van Kerkwijk, M. Kramer, C. Bassa et al., Science **340** 6131 (2013).
- [171] P. C. C. Freire, C. Bassa, N. Wex et al., MNRAS **412** 2763 (2011).

- [172] F. Weber, *Pulsars as Astrophysical Laboratories for Nuclear and Particle Physics*, (IOP Publishing, Bristol, 1999).
- [173] N. K. Glendenning, *Compact Stars: Nuclear Physics, Particle Physics, and General Relativity*, (Springer-Verlag, New York, 2000).
- [174] D. M. Palmer et al., *Nature* 434 1107 (2005).
- [175] B. Franzon, V. Dexheimer, S. Schramm, arXiv:1508.04431v1 (2015); E. J. Ferrer, V. de La Incera, J. P. Keith, I. Portillo, and P. L. Springsteen, *Phys. Rev. C* 82 065802 (2010); D. Lai and S. L. Shapiro, *Astrophys. J.* 383 745 (1991); I. Fushiki, E. Gudmundsson, and C. Pethick, *The Astrophys. J.* 342 958 (1989).
- [176] M. Bocquet, S. Bonazzola, E. Gourgoulhon and J. Novak, *Astron. & Astrophys.* 301 757 (1995).
- [177] C. Y. Cardall, M. Prakash and J. Lattimer, *AstroPhys. J.* 554 322 (2001).
- [178] A. Broderick, M. Prakash and J. M. Lattimer, *AstroPhys. J* 537 351 (2000).
- [179] S. Chakrabarty, D. Bandyopadhyay and S. Pal, *Phys. Rev. Lett.* 78 2898 (1997).
- [180] W. Chen, P. Q. Zhang and L. G. Liu, *Mod. Phys. Lett. A*22 623 (2005).
- [181] F. X. Wei, G. J. Mao, C M. Ko, L. S. Kissinger, H. Stoecker and W. Greiner, *Jour. Phys. G* 32 47 (2006).
- [182] Y. F. Yuan and J. L. Zhang, *AstroPhys. J* 25 950 (1999).
- [183] T. Ghosh and S. Chakrabarty ,*Int. Jour. Mod. Phys. D*10 89 (2001).
- [184] T. Ghosh and S. Chakrabarty, *Phys. Rev. D*63 043006 (2001).
- [185] S. Chakrabarty and P. K. Sahu, *Phys. Rev. D* 53 8 (1996).

References

- [186] S. Chakrabarty, Phys. Rev. D 54 1306 (1996).
- [187] R. G. Felipe, A. P. Martinez, H. P. Rojas and M. Orsaria, Phys. Rev. C 77 015807 (2008).
- [188] A. G. W. Cameron, Nature 205 787 (1965).
- [189] S. Chandrasekhar, Astrophys. J., 140 417 (1964).
- [190] C. W. Misner, K. S. Thorne and J. A. Wheeler Gravitation (1970).
- [191] G. F. Burgio, M. Baldo, P. K. Sahu, A. B. Santra and H. J. Schulze, Phys. Lett. B 526 19 (2001).
- [192] K. K. Mohanta, N. R. Panda and P. K. Sahu, Int. Jour. Mod. Phys. E 24 1550096 (2015); K. K. Mohanta et al, Pramana 82 797 (2014); N. R. Panda, K. K. Mohanta and P. K. Sahu, Jour. of Phys.: Conf. Series 599 012036 (2015); N. R. Panda, K. K. Mohanta and P. K. Sahu, Proc. Indian Nat. Sci. Acad. 81 256 (2015).
- [193] J. Boguta and R. A. Bodmer, Nucl. Phys. A 292 413 (1977).
- [194] N. K. Glendenning and S. A. Moszkowski, Phys. Rev. Lett. 67 2414 (1991).
- [195] S. K. Ghosh, S. C. Phatak and P. K. Sahu, Z. Phys. A 352 457 (1995).
- [196] Y. Sugahara and H. Toki, Nucl. Phys. A 579 557 (1994).
- [197] J. Schaffner and I. N. Mishustin, Phys. Rev. C 53 1416 (1996).
- [198] H. Takahashi et al., Phys. Rev. Lett. 87 212502 (2001); J.K. Ahn et al., Phys. Rev. Lett. 87 132504 (2001); M. Danysz et al., Nucl. Phys. 49 121 (1963); S. Aoki et al., Prog. Theor. Phys. 85 1287 (1991).
- [199] L. D. Landau and E. M. Lifshitz, Quantum Mechanics (Pergamon Press, Oxford, 1965).

- [200] P. K. Sahu, G. F. Burgio and M. Baldo, *Astrophys. J.* 566 L89 (2002).
- [201] P. K. Sahu and S. K. Patra, *Int. Jour. Mod. Phys A*16 2435 (2001).
- [202] G. F. Burgio, M. Baldo, P. K. Sahu and H. J. Schulze, *Phys. Rev. C* 66 025802 (2002).
- [203] N. K. Glendenning, *Phys. Rev. D* 46 1274 (1992).
- [204] N. Yasutake, R. Lastowiecki, S. Beni, D. Blaschke, T. Maruyama and T. Tatsumi, *Phys. Rev. C* 89 065803 (2014); N. Yasutake, H. Chen T. Maruyama and T. Tatsumi, arXiv:1309.1954v1, (2013).

References